



Intelligent Planning for Refractive Surgeries: A Modelling and Visualisation-based Approach

Thesis submitted in accordance with the requirements of the University of Liverpool for
the degree of Doctor in Philosophy by

Wei Wang

June 2020

Abstract

Laser refractive surgeries have been commonly used in ophthalmic operations. Considerable research has been carried out and encouraging progress made in recent years. It covers properties of the cornea and behaviour of tissue in different parts of the eye, topography and material expression of individual patient's eyes, prediction using finite element (FE) analysis to estimate the corneal shape change and the change in refractive power. Further effort is still required to advance the research to aid the decision making for laser refractive surgeries. This study comprehensively reviews the latest techniques of refractive surgery and research on computational analysis and modelling techniques and their applications, especially the current prediction and planning techniques for laser refractive surgeries. The aim of this study is to develop an intelligent assistant tool for the laser refractive surgeries with prediction and visualisation functions. For this aim, two objectives will be achieved: prediction with the clinical dataset and human vision simulation.

Due to clinical statistics, the clinical dataset is often incomplete, imbalanced, and sparse. Three methods are proposed to predict surgery parameters and outcomes using the clinical dataset. A multiple imputation method, with multiple regression, is proposed for imputing the missing data. For the imbalance of data distribution in the clinical dataset, an over-sampling of the minority data method is proposed. The accuracy of predicted minority data is close to the accuracy of predicted majority data. Finally an ensemble learning method which is optimised by the genetic algorithm is proposed to improve the accuracy of the prediction results with a sparse dataset. According to the distribution of the sample in the clinical data, the percentage of unacceptable results is 23.02%. The methods in this study could provide an accuracy of 79.02% to find the possible unacceptable cases, that is, the method could reduce the percentage of unacceptable results from 23.02% to 4.82%.

In human vision simulation, the study focuses on how the human vision simulation could be determined and obtained accurately within a required timeframe. The ray tracing technique can provide more precise results than the rasterisation technique, especially for the simulation of light reflection and refraction in the human eyeball. However, the thin lens assumption affects the accuracy of the pathological vision simulation with the ray tracing technique. An improved schematic human eye model is proposed to obtain a numerical model predicting the size of the defocus blur for the pathological vision, which wraps the

shape of the ray intersection area. In order to generalise this model to other healthy and pathological vision, an intelligent blur range derivation method is proposed. On the other hand, ray tracing scene rendering requires repeated iterative computing which takes a significant amount of computation time. A GPU-based ray tracing computing method is proposed to accelerate and optimise the rendering of scenes. With this method, the scene rendering speed is about 75 times faster than using the CPU.

Acknowledgements

I would like to express the deepest gratitude to my wife Jing and my son Chenyu. They were always supporting me and encouraging me with their best wishes. I would like to express the deepest gratitude to my parents. They gave my life and love. I would like to thank my other family members. They helped me during the darkest time.

I would like to express the deepest gratitude to my primary supervisor Prof. Yong Yue. He has provided much help during my PhD and provided valuable help, support, care, patience and guidance. Working with him is enjoyable. The deepest gratitude is also due to my secondary supervisors, Prof. Ahmed Elsheikh and Dr Fang-jun Bao. Without their knowledge and assistance, this research would not have been successful.

I would like to thank people who help me at Xian Jiaotong-Liverpool University, University of Liverpool and Wenzhou Medical University. Special thanks to Dr Jie Zhang, Mr Hang Dong, Dr Xiaohui Zhu. I do not forget my colleagues in SD428 who always encouraged each other.

Contents

Abstract	i
Acknowledgements	iii
Contents	vii
List of Figures	ix
List of Tables	x
1 Introduction	1
1.1 Overview	1
1.2 Motivations	4
1.3 Research Questions and Aim	6
1.4 Research Methodology	8
1.5 Contributions	9
1.6 Published Work	11
1.7 Thesis Outline	12
2 Literature Review and Previous Work	13
2.1 Overview	13
2.2 Prediction in Refractive Surgery	15
2.3 Data Imputation	17
2.4 Data Resampling	19
2.5 Ensemble Learning	20
2.6 Human Eye Modelling and Human Vision Simulation	22
2.6.1 Schematic Eye Model	22
2.6.2 Human Vision Simulation	23
2.7 GPU-Accelerated Related Work	24
2.8 Summary	25

3	Clinical Dataset and Data Pre-process	27
3.1	Overview	27
3.2	Introduction of LASIK	28
3.3	Refractive Surgery Dataset	29
3.4	Multiple Imputation for Missing Data	35
3.5	Prediction of CMAD	37
3.6	Summary	39
4	Prediction of Surgery Outcomes	41
4.1	Overview	41
4.2	The Imbalanced Data Distribution	42
4.3	The Over-sampling Method	44
4.3.1	The Baseline for Evaluation	44
4.3.2	The Over-sampling Method	44
4.3.3	The Prediction Model of Surgery Outcome	47
4.3.4	Results and Analysis	48
4.4	The Ensemble Learning with Genetic Algorithm Optimization	49
4.4.1	The Optimisation Algorithm	50
4.4.2	The Ensemble Learning	51
4.4.3	Results and Analysis	53
4.5	Summary	54
5	Simulation of Human Vision using Ray Tracing	55
5.1	Overview	55
5.2	The Related Basis Principles	57
5.2.1	The Image-forming Principle of Human Eye	57
5.2.2	The Principle of Refractive Surgery	59
5.3	Methodology	60
5.3.1	Modelling the Human Eye	60
5.3.2	Human Vision Simulation	63
5.4	Results and Analysis	69
5.4.1	The Improved Human Eye Model	69
5.4.2	Simulation of the Human Vision	76
5.5	Summary	79
6	GPU-Accelerated Ray Tracing Method	81
6.1	Overview	81
6.2	Overview of CUDA Platform	82
6.3	The Method of GPU-Accelerated Ray Tracing	85
6.4	The Performance Analyses and Optimisations	87
6.4.1	Analysis of computing speedup	88

6.4.2	Threads Optimisation	91
6.4.3	Device Memory Optimisation	93
6.5	Summary	95
7	Conclusion	97
7.1	Overview	97
7.2	Summary	97
7.3	Main Findings	99
7.4	Research Contributions	101
7.5	Future Work	102
	References	103

List of Figures

3.1	The sample report of the LASIK	29
3.2	The process of the LASIK	30
3.3	Preoperative SP Histogram	33
3.4	CMAD Histogram	33
3.5	Preoperative SP Distribution	34
3.6	CCT Distribution	34
3.7	The missing data visualization	34
3.8	Multiple Imputation Methods	36
3.9	Linear Regression between Preoperative SP and CMAD	38
4.1	The distribution of 3-month Post-surgery SP	42
5.1	The Normal Monocular Vision	56
5.2	The Original Scene	56
5.3	The Abridged General View of Human Eye	58
5.4	The Process of Human Vision Model and Simulation	61
5.5	The Anatomical Structure of the Human Eyeball	62
5.6	The Framework of Human Vision Simulation	64
5.7	The CoC Calculation	65
5.8	The Anatomical Structure View of the Intersection of the Ray	68
5.9	The 2D Schematic View of the Intersection of the Ray	69
5.10	The Incident Ray Path of Emmetropia with the Improved Human Eye Model	70
5.11	The Intersection Points of Incident Rays on the Retina	70
5.12	The Incident Ray Path of Emmetropia for Near Object	71
5.13	The Intersection Points of Incident Rays for Near Object	71
5.14	The Incident Ray Path of Emmetropia for Large Incident Angle	72
5.15	The Intersection Points of Incident Rays for Large Incident Angle	72
5.16	The Myopia with 1mm Additional Axial Length	73
5.17	The Retinal Intersection Points of Myopia with 1mm Additional Axial Length	73
5.18	The Myopia with 2mm Additional Axial Length	73
5.19	The Retinal Intersection Points of Myopia with 2mm Additional Axial Length	73

5.20	The Incident Ray Path of Post-surgery	74
5.21	The Intersection Points of Post-surgery	74
5.22	The Incident Ray Path of Overtreatment	75
5.23	The Intersection Points of Overtreatment	75
5.24	The Scene without Defocus Blur	76
5.25	The Scene with DoF Effect for Thin Lens	76
5.26	The Defocus Blur with Improved Human Eye Model	76
5.27	The Myopia Simulation	77
5.28	The Post-surgery Simulation	77
5.29	The Original Optometry data for the Subjective Evaluation	78
5.30	The Myopia simulation for the Subjective Evaluation	79
6.1	The SM Structure of the GPU Used by the Quadro P5000	82
6.2	GPU Parallel Computing System	83
6.3	Schematization of Thread organization	84
6.4	The Basic Principle of the Ray Tracing	86
6.5	The CPU Usage of Serial Process	87
6.6	One Pixel Computing Time between CPU-based Serial Computing and GPU-based Parallel Computing	90
6.7	The Total Time Cost Comparison between CPU-based Serial Computing and GPU-based Parallel Computing	91
6.8	The Speedup of GPU-based Parallel Computing Compared with the CPU-based Serial Computing	92
6.9	The Efficient of GPU-based Parallel Computing Compared with the GPU-based Serial Computing	92
6.10	The Speedup with the Different Block Size	93
6.11	The Number of Registers of the Different Block Size	93
6.12	The Comparison among the Different Combination of Block Size and Number of Registers per Thread	94
7.1	The Intelligent Assistant Tool of the Laser Refractive Surgery	98

List of Tables

3.1	Mean Values and Standard Deviation of Biological Parameters	31
3.2	Mean Values and Standard Deviation of Surgery Parameters	32
3.3	Mean Values and Standard Deviation of Post Surgery Outcomes	32
3.4	AIC Values of the First-month Post-surgery SP Regression	35
3.5	t-state of the first-month Post-surgery SP Regression	36
3.6	Mean Values and Standard Deviation of All Measures	37
3.7	Correlation between Ablation Depth and Other Parameters	37
3.8	Correlation between Ablation Depth and Other Parameters	37
3.9	Comparison of Multiple Regression and Munnerlyn Approximate Formula	39
4.1	Biometrics, Refractive and Treated Parameters	43
4.2	The Confusion Matrix without Over-sampling	44
4.3	Biometrics, Refractive and Treated Parameters with Over-sampling	46
4.4	Mean Impact Value	47
4.5	MSE of different numbers of member in hidden layer	48
4.6	Confusion Matrix with Over-sampling	49
4.7	Genetic Algorithm Initial Parameters	53
4.8	Confusion Matrix with Final Model	53
5.1	The Optical Properties of a Fully Relaxed Eye	61
5.2	The Sample Data	67
5.3	The Optical Properties of the Test Eye	78
6.1	GPU Memory Hierarchy	85
6.2	Performance Test Platform Specifications	88
6.3	The Rendering Parameters for Test	89
6.4	The Comparison among the GPU Memories	94
6.5	The Speedup of Memory Optimisation	95

Chapter 1

Introduction

1.1 Overview

The global prevalence of refractive errors has been estimated to range from 800 million to 2.3 billion. China is one of the countries with the highest myopic rates among its total population of over 1.3 billion. A considerable number of studies have been conducted on laser refractive surgeries. Many publications introduced the successful cases of laser refractive surgeries. [1, 2, 3, 4, 5, 6]. Although laser refractive surgeries have been widely accepted, the study of postoperative complications of laser refractive surgeries continues to be a focus of research. [2, 6]. These postoperative complications may be associated with the creation of corneal flap before the excimer laser ablation [7], wound healing after the surgery and other biomechanical responses of the cornea to the change of structure introduced by the surgery process [8, 9]. Currently, laser refractive surgery has developed different surgery forms from Laser-Assisted In-situ Keratomi (LASIK) such as Femto-LASIK, FLEx and SMILE, which are claimed to have advantage over LASIK [10, 11, 12]. However, these surgery forms all lead to changes in the biomechanical properties of the corneal structure, thus causing postoperative complications which are the same as LASIK [13, 14, 15, 16, 17].

Laser myopic correction has been successful in practice, while improvements are still desired for more accurate and safer treatments for all the forms mentioned above. The computer-aided refractive surgery planning and prediction is one of the important aspect. It requires novel computer modelling of the biological parameters of each individ-

ual patient's eyes to simulate refractive surgery procedures and advanced computational techniques for determining optimum surgical procedure parameters. This project aims to develop such an intelligent planning tool. It will develop a comprehensive database for necessary information and knowledge representation and a dedicated graphical user interface. It is undeniable that laser refractive surgeries are very successful in practice. However, it is necessary to improve the problems of surgeries for obtaining more accurate and safe treatment results. One of the critical aspects in the planning of refractive surgeries requires a novel computer simulation model that simulates the surgical procedure based on corneal biometrics to determine the optimal surgical parameters and possible surgical outcomes for each patient. However, the models, algorithms and other technical details used in the surgical equipment for laser refractive surgeries are limited by the protection of intellectual property. They are not published; that is, this system is entirely unknown inside and is a black-box system. For a black-box system, it is hard to construct the mathematical model of simulation system using general approaches, such as an analytical approach, deductive approach, theoretical modelling approach and mechanism modelling approach [18, 19].

Moreover, laser refractive surgeries are multi-input and multi-output nonlinear systems. It is not easy to obtain a sufficiently accurate mathematical model of simulation system using approaches such as a testing approach, inductive approach, or system identification method. Machine learning provides an approach for obtaining a mathematical model of laser refractive surgeries. The number of input variables and outcomes for machine learning can be selected as needed, and some approaches in machine learning, such as regression, artificial neural networks (ANN), and support vector machines (SVM), can approximate arbitrary nonlinear functions. Furthermore, some methods in machine learning, such as ANN and SVM, can generate the identification model, but not the computational model. The tunable parameters of this model are reflected in the connections and weights inside the networks. This model does not require the creation of an identification format based on a mathematical model of the actual system (surgery process). The step of system structure identification can be omitted. In theory, the mathematical model of laser refractive surgeries can be established by a method of machine learning that selects, trains, and adjusts without having to delve into the specific mechanism or system structure of the laser refractive surgery. However, due to the statistical problems and other real-world problems, the dataset used for the modelling process always has some defects, e.g. missing data, imbalanced data distribution and sparse data distribution. These defects make the

mathematical model unacceptably inaccurate. Therefore, the dataset problem is one of the main problems that this study should solve.

Furthermore, the mathematical model of laser refractive surgeries simulation is used to achieve surgical planning and the prediction of the surgical outcomes. It is better to visualise the simulation results to evaluate the surgical planning and surgical outcome intuitively. One of the prerequisites is to simulate human vision in an acceptable time accurately. The principle of human vision is to project a three-dimensional (3D) scene of the real world onto a two-dimensional (2D) retina. Similar to human vision, the process of human vision simulation is to display a 3D scene on the 2D screen. There are two approaches to accomplish this task. One is rasterisation, and the other is ray tracing. Both approaches have a balance between how to handle real-time and high-fidelity in rendering.

With the supporting of modern graphics processing units (GPUs), real-time rendering and high-fidelity simulation can be achieved in rasterisation. Rasterisation has played a dominating role in simulation for a long time. Furthermore, it is widely used in simulation for the information visualisation. OpenGL and DirectX, both based on rasterisation are the most famous application programming interfaces (APIs) in simulation. Rasterisation uses the mesh of triangles or polygons to describe the 3D model in the scene. In the mesh, the vertices of each triangle intersect the vertices of other triangles with different sizes. Each vertex includes position, colour, texture, and normal information. All the vertices in the 3D scene are then mapped to pixels or points on the 2D screen. In the 2D screen, the initial colour of each pixel is determined by the vertices information of the 3D scene. With scene illumination analysis, multi-layer texture application and other further operation, the final colour of each pixel on the 2D screen is determined. However, the 3D scene rendering process of rasterisation is not suitable for human vision simulation for the following reasons:

1. Light intensity, reflection types and materials are considered during the scene illumination analysis of rasterisation. All rays can only be reflected once in a scene. The refraction is not considered. Nevertheless, for real human vision, rays may reflect and refract multiple times before reaching the retina. Rasterisation is unable to simulate this process.

2. In the 3D scene, the model details are approximated by mathematical approaches, such as digital differential algorithm (DDA), Bresenham algorithm and anti-aliasing algo-

rithm. For real human vision, the dioptré and the object distance are both the causes of the detail loss. Rasterisation is unable to simulate this process.

However, simulation can also display a 3D scene on a 2D screen using the ray tracing method. The ray tracing method uses a ray from the light source to reflect and refract among the various models in the 3D scene. The intersections of the ray and the model, the reflective and refractive direction and the ray intensity are computed. In this process, the ray passes through the lens of a virtual camera. The intensity and colour of the ray determine the image displayed on the 2D screen. Compared with rasterisation, the principle of ray tracing is more similar to human vision. However, compared with the rasterisation method, in order to obtain an accurate rendering result, the ray tracing method needs an accurate schematic human eye model which takes into account the normal and pathological human eye, and a large amount of computing time which is used to analyse the ray path. That is another problem that this study aims solve.

The work is directed at the development of such an intelligent planning tool to predict the surgical parameters and outcome for laser refractive surgeries. It is the focus of the study. This planning tool is based on the vital information and knowledge representation of the laser refractive surgeries, and with a dedicated graphical user interface.

The rest of this chapter is organised as follows. The additional discussion of the motivations is presented in Section 1.2. Section 1.3 presents the research question and related issues. The primary research methodologies adopted to address the research question and related issues are discussed in Section 1.4. Section 1.5 highlights the research contributions. Section 1.6 and Section 1.7 list the published works during the study and the outline of this thesis, respectively.

1.2 Motivations

The main aim of the study presented in this thesis is to find effective and accurate approaches to establish simulation and visualisation mathematical models using the concepts and methods of machine learning, which will enable reliable predictions of surgical parameters and outcomes for the laser refractive surgeries. Most of the studies on simulation and visualisation of the human eye and human vision have tended to focus on the healthy human eye and normal human vision. There is minimal published work on the modelling for the abnormal human eye and pathological human vision. Simulation and visualisation

of the abnormal human eye and pathological human vision should be the pre-condition of the refractive surgeries. In practice, at least with respect to the clinical diagnosis of laser refractive surgeries, this can be accomplished roughly by using a theoretical formula and the experience of surgeons; although the surgical instruments can provide some surgical parameters and possible surgical results in numerical form, due to the protection of intellectual property, the approach has not been published. Meanwhile, it has not been modified or optimised by the surgeons. On the other hand, this approach of using surgical instruments to predict surgical outcomes is not efficient, given that patients who need to complete the surgery are still waiting in the queue. Using a machine learning method for the human eye modelling and the human vision simulation, and then implementing the intelligent planning, prediction and evaluation of laser refractive surgeries, even if only coarsely achieved, would significantly improve the prediction accuracy and reduce the time to process the prediction. The areas, where intelligent planning would be of particular value, are in screening programmes where large quantities of pre-surgery biological parameters need to be processed in such a way that surgeons and patients can receive the surgical planning and post-surgery outcomes during the initial examinations. The results of this study can also be applied to screen for glaucoma and other eye diseases caused by diabetes using machine learning.

In summary, the motivations for choosing refractive surgeries as a focus for the study presented in this thesis are as follows:

1. Little work has been reported for the planning, prediction and evaluation of refractive surgeries in terms of machine learning applied to the clinical data. However, there have been many studies that have used regression methods to perform statistical analysis of refractive surgery results. The majority of the reviews are on the analysis of the patient biological features [20, 21], the study of surgery parameters [22, 23] and the study of surgery outcomes [24, 25].

2. With the widespread use of laser refractive surgery, many clinicians have found that it is difficult to find new information and knowledge from existing clinical data using traditional medical statistical methods such as regression. Besides, clinicians lack the tools to predict and evaluate surgical outcomes. Most existing refractive surgery tools only support the analysis of a patient's biological parameters and suitability for surgery. In practice, in refractive surgery, the subjective assessment of the clinician is the primary method of preoperative evaluation. Although the success rate of refractive surgery is

high, the process may still be affected by clinicians' human errors and skills. Therefore, intelligent planning based on a machine learning method proposed in this thesis is of practical significance for the prediction and evaluation of the refractive surgeries. It can provide more objective surgical plans, predictions, and evaluation recommendations. In addition, it enables clinicians and patients to understand the outcomes of the surgery in advance.

3. The Computer-Aided Diagnosis (CAD) is an essential element in the medical care field and is certainly not limited to refractive surgeries. The method mentioned in this thesis could be used in the ophthalmological studies and other medical studies for supporting the automatic CAD, and help the clinicians and scientists discover new information and knowledge from the clinical data.

4. The accurate human eye model and human vision simulation could be used for many other fields, such as glasses design, or the development of an optical system. In particular, the abnormal human eye model and the pathological human vision simulation, including myopia and hyperopia, could help to develop display systems suitable for the people with the ophthalmic diseases.

5. The acceleration method for the ray tracing proposed in this thesis could provide the support to develop a new real-time rendering engine for the simulation system, game and virtual-reality system.

1.3 Research Questions and Aim

Based on the research motivations outlined in Section 1.2 above, the work in this thesis aims to investigate methods that can help with the planning, prediction, and evaluation of refractive surgery. More specifically, the study in this thesis intends to use machine learning to complete the prediction of surgical parameters and surgical outcomes. Besides, With the establishment of a mathematical model of human eyes, machine learning can be used to simulate human vision, with the result that refractive surgery can be planned, predicted, and evaluated. Thus the overall research question of this thesis is

Is it possible to design machine learning-based methods suitable for multi-input, multi-output and non-linear system modelling so that effective data prediction and simulation can be achieved in the presence of missing data, imbalanced data, sparse data and complex datasets?

The reasons for adopting a machine learning method as follows:

1. The raw data in the medical field are diverse and heterogeneous. These data include the biological parameters of patients, clinical examination results, doctors' observations and consultations. These data are directly or indirectly related to the final diagnosis result and treatment. The methods of medical statistics cannot solve the problems of data diversity and heterogeneity, whereas the methods of machine learning can provide a reference for doctors by establishing relationships among different properties by forming various relational expressions.

2. It is difficult for medical data to express its structure and characteristics mathematically in the collection of medical data. It is not easy to integrate and structure the data into a formula or model that reflects the relationship among the data. Machine learning methods can obtain the association of species data through methods such as clustering, regression, or sequence analysis.

3. It is difficult to avoid noise interference completely. Machine learning methods can increase the fault tolerance of the model by ignoring specific bizarre samples, prevent the over-fitting of the model, and improve the generalization of the model.

4. The medical data is inevitably lost. The method of medical statistics is to discard these incomplete data, but the information in these data is lost along with it. Machine learning methods can interpolate this part of the incomplete data to maximize the information contained in the data.

5. The medical data often contains redundant, meaningless or additional attributes. Machine learning can remove these attributes through correlation analysis and collinearity analysis to improve the accuracy of the final model.

6. The medical data often face data shortage. Due to technical conditions and acquisition costs, certain types of properties or data volume are relatively small compared with the total. Machine learning can solve such data shortages and imbalances by under-sampling or over-sampling, or by using vision simulation to generate new data.

In summary, a core issue of using machine learning to model multiple-input, multiple-output and the non-linear system is the problem of processing data sets. The reason for this problem is that the medical data used in the mathematical modelling of medical diagnosis is often a by-product of medical behaviour and is not explicitly collected for modelling. These medical data may have problems such as missing data, imbalanced data and spare data due to statistics, ethics, disease characteristics, and noise. Another core issue is the

data shortage problem faced by using machine learning for system modelling. The reason for this problem is that the amount of data required for modelling is large, the cost is high, and it exceeds the current technology level.

The above research question thus encompasses five subsidiary research questions:

1. *The issue of missing data*

In a real system, due to the problems of statistics, the missing of input and output data is unavoidable. During the process of modelling using a machine learning approach, the deviation of the mathematical model is largely due to the missing data.

2. *The issue of imbalanced dataset*

In a real system, the amount of data outputted by one type of output is much less than (or more than) the amount of data outputted by other types. The imbalanced dataset can deviate the model built by machine learning.

3. *The issue of sparse data distribution*

Due to data statistics or real system characteristics, the data distribution is not concentrated, so that an effective model cannot be trained.

4. *The ray tracing method uses blur to describe the loss of details.*

The computing of the blur range and quantity are determined by the blur distribution function (BDF). Currently, the BDF is determined for normal human vision and is not suitable for pathological human vision.

5. *The computing of ray intersection, ray reflection and ray refraction take significant time.*

For the existing algorithm and hardware technology, it is impossible to guarantee high-speed and high-fidelity scene rendering. There is also a requirement for a novel accelerate approach for ray tracing computing.

1.4 Research Methodology

Adaptive research methods have widely considered and evaluated many machine learning methods, especially, data imputation, data over-sampling and ensemble learning, to solve these questions.

It is firstly necessary to collect training and test datasets for refractive surgery. The data source is the Eye Hospital of Wenzhou Medical University. This hospital is a specialised

hospital for ophthalmology. The staffs at this hospital are also able to comment, verify and evaluate the utility of the proposed methods.

For the prediction of surgical parameters and results, due to the absence of various properties in the medical dataset, the dataset needs to be pre-processed first, such as by data imputation. These data are then statistically analysed for evaluating the distribution of the data. For Improving the sensitivity (true positive fraction, TPF) and specificity (true negative fraction, TNF) of prediction results, while at the same time, reducing the false positive fraction (FPF) and the false negative fraction (FNF), the high proportions of data are under-sampled. On the other hand, to compensate for the minority data, over-sampling is used. During the prediction process, different machine learning methods are compared. Due to data sparseness, the accuracy of the predictor is only slightly higher than that of random guessing when using a single machine learning method. The ensemble learning method is used to integrate multiple predictors with low accuracy and optimise the weight of each predictor by genetic algorithm. To avoid over-fitting and to improve the generalisation of the predictor, the K-fold cross-validation is used.

On the other hand, in the modelling and visual simulation of human eyes, mathematical models of human eyes suitable for normal and abnormal human eyes are constructed according to the image-forming principles of the human eye and the tenets of refractive surgery. In the visual simulation, the blur distribution function (BDF) is introduced to increase the accuracy and the speed of simulation. BDF is a multi-input, multi-output non-linear function. The machine learning method is used to derive BDF. However, due to the limitation of current technology, imaging data inside the human eye cannot be obtained directly. The established human eye mathematical model and ray tracing method are used to simulate human eye vision to obtain training and test datasets. By constructing neural networks, the BDF is derived. Finally, this study utilises GPU acceleration methods and optimises threads and memory to speed up the generation of datasets and reduce the computation time of ray tracing in simulation.

1.5 Contributions

This thesis makes several significant contributions, and these are summarised in this section. This study achieves the planning, prediction and evaluation of refractive surgery with machine learning methods, and proves the feasibility of modelling multiple inputs, multiple

outputs, and nonlinear systems with machine learning. In pre-processing medical data of refractive surgery, the multiple imputation method and the data over-sampling method of medical data is proposed. The methods improve the accuracy of prediction indicators and reduce the predicted FPF and FNF. Based on the actual prediction results of the refractive surgery, an ensemble learning method optimised by the genetic algorithm is proposed for the medical data to improve the accuracy of the predictor. Furthermore, a novel schematic human eye model is proposed in this thesis. This model is based on the image-forming principle of the human eye and the principle of refractive surgery. This model could simulate normal and abnormal human eyes. With the ray tracing method, the standard and pathological human vision could be simulated by this model. This thesis proposes two ways to improve the accuracy and the speed of human vision simulation. First, the BDF is introduced to simulate the defocus blur in DoF effect. The BDF is derived from the machine learning method. The training and test datasets are obtained by the schematic human eye model proposed above and ray tracing. Second, with GPU acceleration technology, and by optimising the thread and memory, the ray tracing computing is parallelised and accelerated.

In summary, the main technical and practical contributions that this thesis makes can be summarised as follows:

1. A novel and effective method is proposed for planning, predicting and evaluating the refractive surgeries with the medical dataset.
2. A multiple imputation method is proposed for the missing medical data in the training and test datasets.
3. An improved over-sampling method is designed for reducing FPF and FNF with the imbalanced medical data.
4. An ensemble learning method with optimisation is proposed for increasing the accuracy of the predictor in a sparse medical dataset.
5. An improved schematic human eye model with variable axial length and variable corneal thickness is proposed for pathological human vision, e.g. myopia and hyperopia, and refractive surgery.
6. A novel data augmentation method is proposed for machine learning using the results of human vision simulation.
7. A BDF derivation method is proposed for using machine learning.
8. A GPU-accelerated ray tracing rendering engine is designed for human vision simu-

lation.

In addition to the contribution mentioned above, this work has also made some contributions to other fields.

1. A medical dataset with detailed explanations of each property was developed and could be published for further machine learning research.

2. A universal optimisation workflow is designed for other GPU-accelerated applications.

1.6 Published Work

There are some materials in this thesis that have been published previously. This section provides a summary of these publications:

1. *Wei Wang, Yong Yue, Ahmed Elsheikh and Fangjun Bao. Intelligent Planning for Laser Refractive Surgeries. Journal of Physics: Conference Series, 976(1), 2018. EI Compendex.* This paper discusses data mining techniques that can be utilized for the prediction of laser refractive correction surgery parameters. It can provide the surgeon with a reference for possible surgical parameters and outcomes of the patient before the laser refractive correction surgery. The work described in this paper is used as the foundation for work presented in Chapter 3 and Chapter 4.

2. *Wei Wang, Yong Yue, Ahmed Elsheikh and Fangjun Bao. Using imbalanced learning: A case study in refractive surgery outcome prediction. In 9th International Conference on Information Technology in Medicine and Education (ITME 2018), 2018. EI Compendex.* This paper proposes an imbalanced learning method for the prediction of the refractive surgery outcome. The content of this paper is used with respect to the work in Chapter 4.

3. *Wei Wang and Yong Yue. An Improved Schematic Human Eye Model for the Human Vision Simulation. In 2nd International Conference on Advances in Computer Technology, Information Science and Communications (CTISC 2020), 2020. (Accepted)* This paper proposes an improved schematic human eye model for the pathological human vision. The content of this paper is used with respect to the work in Chapter 5.

4. *Software copyright registration, LASIK Refractive Surgery Assistant System, No. 2018R11L466994.* The application document and software specification of this software copyright registration introduces the improved schematic human eye model for the normal and abnormal human eyeball, the BDF derived method using machine learning for human

vision simulation, and the ray tracing based on GPU acceleration. The methods of this software are used for Chapter 5 and Chapter 6.

1.7 Thesis Outline

The remainder of this thesis is organised in the following way. Chapter 2 presents a literature review and related works of this study. Chapter 3 begins by analysing the dataset for this study and the application domain. The chapter also introduces the multiple imputation for the missing data in the dataset. The process of surgery parameters and outcomes prediction is introduced in Chapter 4. This chapter proposes the imbalance learning method and the ensemble learning method with optimisation. In Chapter 5, the improved schematic eye model is introduced. In addition, the BDF derivation method using machine learning is proposed in detail. Chapter 6 introduces the GPU-accelerated ray tracing method and its specific optimisation process. Finally, Chapter 7 presents the conclusions and the main findings of the work presented in this thesis, and some possible directions for future work.

Chapter 2

Literature Review and Previous Work

2.1 Overview

This chapter provides an overview of previous work related to this thesis. In short, the work described belongs to the field of Computer-Aided Diagnosis (CAD), which combines machine learning with medical diagnostics. Thus, this chapter begins with a review of the application of machine learning in refractive surgery in Section 2.2. Machine learning in the medical field is a way to discover the information and knowledge needed for medical diagnosis from large amounts of medical data. The application of machine learning methods in medical diagnosis is mainly divided into two categories: one is the prediction method (regression, classification and time series analysis), and the other is the description method (clustering, association and sequence analysis). Because medical statistics are widely used in the medical field, the regression method is a common approach for the study of refractive surgery. The regression is used for the prediction, comparison, and evaluation of surgical processes and outcomes. According to the literature review, it is found that most of the studies only use the least-square method to fit regression functions or regression equations, but lacking rigorous regression analysis, such as t-test, f-test and p-value. Moreover, the datasets used in most studies are small, usually no more than 500 eyes. Most studies do not analyse the data distribution in the datasets, and the datasets are not published. In this case, the regression model is not confidence. Meanwhile, it is difficult to generalise for

other diagnoses.

In the process of the literature research on machine learning methods in refractive surgery, it is found that most machine learning research focuses on method innovation and more attention is given to improving accuracy.

On the other hand, the dataset is often ignored. Datasets are the foundations of machine learning to discover knowledge. In the dataset, the distribution of data affects the accuracy of the model. Thus, the data imputation research and data resampling research are reviewed in sections 2.3 and section 2.4, respectively. In the process of the literature research, it is found that the multiple imputation method uses a series of possible values to replace each missing value, which can reflect the uncertainty of the missing data being replaced, thus, it could avoid the biased estimates in any single imputation method. The multiple imputation method could produce more efficient model estimates. As mentioned in Chapter 1, it is challenging to collect medical data for machine learning research. The datasets are usually small.

Meanwhile, due to various reasons, e.g. privacy, the treatment, and the outcomes, one type of sample may be less than others. Therefore, using the under-sampling method loses the information hidden in the unselected data. The generalisation of the model is reduced. Due to the data sparseness in the medical dataset, the accuracy of the predictor is only slightly higher than random guessing. The concept of ensemble learning is proposed for better accuracy of prediction. Ensemble learning is summarised in Section 2.5. With the literature research, it is found that ensemble learning can improve the accuracy of the model in the medical field.

On the other hand, in order to accurately evaluate the outcomes of refractive surgery, it needs to model the human eye and simulate the human vision. The schematic human eye models are reviewed in Section 2.6.1. It was found that all the schematic eye models emphasised the changes of the refractive power. However, these models ignore the main features of the abnormal human eye, such as the change of axial length for myopia. In addition, all the schematic eye models do not consider laser refractive surgeries, that is, the changes in the corneal thickness. In Section 2.6.2, the studies on human vision simulation are summarised. It is found that ray tracing has been the focus of visual simulation research in recent years. In addition, defocus blur is one of the main studies in ray tracing, and it is also the key to describing the effect of DoF. In order to improve the accuracy of defocus blur computing, two main methods have been proposed: the multi-pass method and the

post-processing method. The multi-pass method has high accuracy, but the operation efficiency is very low. With post-processing method, however, the accuracy is lower, but the operation efficiency is high. In addition, there is no related study on the pathological vision and post-surgery vision simulation. GPU-accelerated algorithms are introduced for the computational efficiency of ray tracing, and a summary of GPU-accelerated methods is provided in Section 2.7. Section 2.8 is the final summary of this chapter.

The following summarises the research contents of this study.

2.2 Prediction in Refractive Surgery

Because medical statistics are widely used in the medical field, the regression method is common in medicine as a method of predicting, comparing, and evaluating medical procedures and outcomes. There are some studies on refractive surgeries.

Before laser refractive surgery, Salz et al. used fresh human cadaver eyes to analyse the relationship between incision depth, corneal curvature, corneal thickness, corneal diameter and incision length with stepwise regression in the radial keratotomy and introduced the prediction equation of the change in corneal curvature the correlation after radial keratotomy [26, 27]. While the lack of long-term following for the cadaver eyes, they presented a way to predict the outcomes of refractive surgery with linear regression. Block and Block use multiple regression to determine the surface of the cornea in radial keratotomy [28]. Although they introduced the algorithm and ellipsoid equation, they did not, however, provide the solution of this equation. In 2011, Bao et al. solved the ellipsoid equation with 112 eyes multiple regression, moreover, they determined that the axial length is the main morphological parameter related to myopia [29]. Villaseor et al. introduced a linear regression equation which can obtain intraoperative central corneal thickness (CCT) with preoperative CCT in the radial keratotomy [30]. While the size of the dataset is 395 eyes, the dataset spanned a large timescale, from 6 days to 18 months. This situation may increase the error in the regression equation.

Since laser refractive surgeries were invented; there have been studies on the data analysis of the risk of surgery, patient biological feature, surgical parameters and outcomes. Ehlers and Hjortdal used 40 eyes stepwise linear regression to compare the difference between two types of attempted correction [31]. Dutt et al. used one-year results of excimer laser photorefractive keratectomy (PRK) to analyse the correlation between the attempted

refractive correction and the achieved correction with linear regression [32]. The dataset of Srinivass study is 47 eyes of 39 patients. Kohlhaas used 297 eyes (divided into five linear regression groups) to analyse the correlation among intraocular pressure (IOP), CCT and corneal curvature after corneal refractive surgery [33]. There are slight correlations among IOP, CCT and corneal curvature. With 50 eyes linear regression, Yuan-Chieh Lee et al. presented the development of glare and halo symptoms was correlated with the attempted correction of spherical equivalent (SE) and astigmatism, but not correlated with the pupil size [34]. In contrast, with 92 eyes linear regression, Helgesen et al. claimed the large pupil size is associated with postoperative visual disturbances during scotopic condition [35]. Won-Mo Yi et al. introduced a linear regression method to evaluate the correlation between corneal flap thickness and preoperative corneal thickness with 69 eyes [36]. The correlation between corneal flap thickness and preoperative corneal thickness was found in this study. With 20 eyes linear regression, Srivannaboon et al. claimed that the corneal power changes measured by Orbscan-derived total optical power maps correlated highly with the manifest refractive change produced by LASIK [37]. With 56 eyes linear regression, Bhren et al. claimed the postoperative wavefront error had limited influence on the subjective quality of vision [38]. With 43 eyes linear regression, Lackerbauer et al. claimed there is limited correlation between the corneal ablation and refractive outcomes in LASIK [39]. Alio et al. evaluated PRK outcomes and introduced a predictive model for the refractive changes in the long term with 33 eyes linear regression [40]. Given the small size of these datasets, the results may be disturbed by the outliers in the dataset.

Juan et al. introduced a way to evaluate the effectiveness and safety of LASIK with 143 eyes linear regression [41]. In their studies, there was a significant correlation between achieved correction and difference between preoperative and postoperative mean keratometric readings. Huang et al. introduced a method to estimate the deviation in myopia and astigmatism mixed refractive surgery with 523 eyes multiple regression [42]. He found that the spherical ablation by LASIK has 19% greater refractive change than by PRK. With 706 eyes linear regression, Recep claimed that the decrease in IOP was related to the decrease in corneal stromal thickness after LASIK [43]. With 102 eyes linear regression, Durairaj et al. presented the regression equation of actual stromal ablation [44]. After 484 eyes linear regression, Van Gelder et al. presented the suboptimal outcomes of attempted correction in one eye, increasing the risk of a poor outcome in the other eye in the bilateral LASIK [45]. After 196 eyes linear regression, Eleftheriadis claimed thinner flap is

associated with the faster visual recovery and less myopic SE. Postoperative complications are unrelated to the flap thickness [46]. Chen and Hamilton introduced the correlation between corneal biomechanical properties, e.g., corneal hysteresis (CH) and a corneal resistance factor (CRF), and attempted refractive correction in LASIK [47, 48]. Ogasawara and Onodera analysed the correlation of residual stromal bed thickness and regression of myopia after LASIK with linear regression [49]. While the values of P-value and R-squared are used to evaluate the regression in these studies, more details of regression, e.g., standard error and correlation, are not mentioned. The accuracy of the results can not be evaluated.

Choudhri used 250 eyes multiple linear regression to predict the corneal flap thickness in LASIK [50]. The corneal thickness is most significantly correlated with corneal flap thickness. With 8113 eyes linear regression, Chang presented a method to predict the change of IOP after the LASIK with refractive change [51]. Razmjoo introduced a regression model for correcting intraocular lens power after refractive surgery independent of preoperative data with 148 eyes linear regression [52]. Wangsupadilok presented a regression equation of IOP and CCT with 437 eyes linear regression [53]. Liyanage, Allan et al. developed a systematic method for quantifying pre-treatment adjustments to the treatment sphere in patients having myopic wavefront laser in situ keratomileusis with multiple linear regression [54, 55]. The mean-squared-error (MSE) is a measure of the quality of an estimator [56]. The root-mean-square error (RMSE) is a measure of accuracy, to compare forecasting errors of different models for particular data and not between datasets [57]. For the prediction model with regression, MSE and RMSE could be used to evaluate the accuracy. However, they were not mentioned in these studies.

The related work provided an efficient way to plan and evaluate laser refractive surgery using data mining techniques. This study explores how to predict the corneal maximum ablation depth with data mining. In addition, more details of regression (e.g., standard error and correlation which have been neglected in previous studies) could be used to evaluate the accuracy of model and results.

2.3 Data Imputation

Missing data is very common in medical statistics and medical diagnostic research. Compared with no missing data, the missing data make the results of medical diagnosis deviate

and undermine the effectiveness of the conclusions.

There are three main types of missing data: missing completely at random (MCAR), missing at random (MAR), and missing not at random (MNAR)[58, 59]. In medical diagnosis, typical examples of MCAR include the inability to perform cardiology analysis because the patient's heart rate is not fully recorded, or the patient's renal function is not detected due to equipment failure. Therefore, with the MCAR assumption, missing data does not depend on observed data or unobserved data [60]. MAR is different from MCAR. With the MAR assumption, missing data depends on what has been observed [60]. For example, in medical surveys, women are less likely to fill in height, and weight items than men, the missing data in such medical surveys belong to MAR. Once gender is considered, the missing data does not depend on their height and weight values. In contrary to MAR, With the MNAR assumption, missing data depends on unobserved data, such as the value of the observation itself[60]. For example, people with myopia or hyperopia are more likely to take vision measurements than people with normal vision, even after gender and age are considered. If there is a lack of vision measurement data, it may be due to an individual's unobserved features (with normal vision). Donders and Little believe that in the field of medical diagnosis, in most cases, the missing data is not attributed to either MCAR or MNAR, but MAR. Based on the data that could be observed, it is possible to determine whether the missing data is MCAR. However, it is impossible to evaluate whether the missing data is MAR or MNAR. [60, 61]

For the missing data in the machine learning, there are many types of research which have proposed several methods, e.g. list-wise deletion[62], missing indicator method[63], and single imputation[62]. These methods all assume that the missing data type is MCAR. With MCAR assumptions, these methods could provide unbiased estimates, but these estimates are less accurate. List-wise deletion is the most popular method for the missing data. Any row with missing data is deleted from the dataset. Only the rows with the complete data are reserved for the analysis. However, the operations of list-wise deletion method reduce the sample size and make a significant bias for the estimate; meanwhile, the information hidden in the rows with missing data are discarded [62]. Missing indicator method considers the missing data as a new group, named missing, or as a fixed value, usually zero. This method could use all available data in the dataset, even if data are missing in some rows. This method makes the direction of the bias hard to estimate [63]. Similar to the missing indicator method, single imputation method uses a single value, e.g.

mean value, the possible value and most recently value, to replace the missing data [62]. Similar to the missing indicator, this method makes biased estimates.

Multiple imputation, as an effective method for missing data, solves the model uncertainty caused by missing data [64]. Multiple imputation provides the associated unbiased estimates based on valid data with the MAR assumption in most of the statistical tools [65]. Buuren proposes that multiple imputation could also work with MCAR or MNAR assumption [66]. Multiple imputation replaces each missing data with a series of possible values to reflect the uncertainty of the missing data being replaced. Then, the standard statistical analysis process is used to analyze these datasets generated after multiple imputation. Finally, the statistical results from each dataset are synthesized to obtain the estimated values of the overall parameters. Because multiple imputation does not replace missing data with a single value, it tries to generate a random sample of missing data. This method reflects the uncertainty caused by missing data and could produce more effective estimates. Combined with this method, it could easily infer the unknown properties of missing data without discarding any information.

Therefore, the multiple imputation method is chosen for the missing data in the dataset of the refractive surgery. The possible values for replacing the missing data should be discussed in the following chapter.

2.4 Data Resampling

In medical diagnosis, the datasets often suffer from sample data imbalanced across classes. The causes of the situation include the patients' privacy, the feature of the disease and the approach of the diagnosis. For the refractive surgeries, because of the cautious of the clinicians and the maturity of the surgery, the successful outcomes hold an absolute advantage position in the dataset. With this type of dataset, the model produced by the machine learning method tends to output the positive results with any input data. It is a substantial bias of estimate.

A series of data resampling methods are proposed for balanced data distribution among the different classes. These methods could be divided into two main categories: one is under-sampling, the other is over-sampling. The under-sampling is for the majority class. By under-sampling the majority class, the data sample size could be balanced between the majority class and minority class. The popular under-sampling methods include NearMiss

family [67], Condensed Nearest Neighbor (CNN) [68], Edited Nearest Neighbor (ENN) [69] and Tomek Link Removal [70, 71]. The main disadvantage of this method is that the information contained in the samples which are not resampled in the majority class is discarded. It causes bias in the estimate. In particular, the dataset size is always small in medical diagnosis. With the under-sampling method, the model produced by machine learning is inaccurate.

In contrary to the under-sampling method, the over-sampling method is suitable for the minority class. By oversampling the minority class, the data distribution between the two imbalanced class could be kept consistent. The over-sampling method includes random over-sampling of the minority class, synthetic minority over-sampling technique (SMOTE) [72], borderline SMOTE [73] and the combination with under-sampling [74, 75, 76, 77]. The combination with under-sampling methods is the new development direction of the data resampling. Due to the uncertainty of the data obtained by the over-sampling, the main disadvantage of the over-sampling method is that the direction of the bias is uncertain. However, if the data obtained by the over-sampling is a small part of the entire dataset, this bias could be corrected by other machine learning method.

Therefore, in medical diagnosis, when the dataset size is not big enough for the under-sampling method, the over-sampling method, especially the combination method of SMOTE, could be a better choice for the data resampling.

2.5 Ensemble Learning

In medical diagnosis, supervised learning is performed using machine learning to achieve the goals of prediction and classification. The desired result is a model that is stable and performs well in all respects. In other words, the generalization ability of the model should be good enough for other datasets. However, the actual model is often not so ideal. In most cases, the only model with preferences (weakly supervised models) can be obtained by machine learning methods. These models may perform well with some datasets and perform poorly in other datasets. The performance of these models may be inconsistent. That is, some models obtain wrong predictions, while others make correct predictions. It could correct wrong predictions by the correct ones. It is the core idea of integrated learning. Ensemble learning is the combination of multiple weakly supervised models to obtain a better and more generalized robust supervised model. Ensemble learning is a

meta-algorithm that combines several machine learning methods into a prediction model to achieve reducing bagging, boosting and improving stacking.

In order to adapt to different dataset sizes, the various data strategies are formulated for ensemble learning:

1. For the large dataset: Divide the dataset into multiple small datasets, use multiple machine learning methods for model training and testing, and combine these models to form the final model.

2. For the small data set: Use Bootstrap method for sampling to obtain multiple data sets, use multiple machine learning methods for model training and testing, and combine these models to form the final model.

The methods of ensemble learning combination models are mainly divided into two categories:

1. Sequential method

Weakly supervised models for training and testing are obtained in order, such as Adaboost methods. The principle of the sequential method is to use the dependencies between weakly supervised models. By assigning higher weights to the wrong samples during training and testing, the prediction and classification accuracy of the final model is improved.

2. Parallel method

Weakly supervised models for training and testing are obtained simultaneously, such as Random Forest method. The principle of the parallel method is to make use of the mutual relationship of independence among the weakly supervised models. The error rate of the final model could be reduced by averaging or simple majority voting.

For the ensemble learning, there are several classical ensemble learning methods, such as Breimans bagging [78], Schapires boosting [79], Adaptive Boosting [80], Wolperts stacked generalization [81] and Mixture of Experts [82].

In medical diagnosis, the datasets for model training and testing always suffer the data sparseness. That is, there are many redundant and noisy data in these datasets, and it is difficult to extract useful information from the datasets. If the accuracy of the model obtained by using a single predictor or classifier is only slightly better than random guessing, it could use ensemble learning to combine weak predictors or classifiers to improve the accuracy of the final model with optimizing the algorithm. Therefore, several studies focus on the combination of ensemble learning and other machine learning methods. Tekin et al. propose the adaptive ensemble learning with confidence bounds for

medical information. [83]. Maji et al. propose the deep convolutional neural networks ensemble learning method for detecting retinal vessels in fundus images [84]. Moreira et al. propose an ensemble learning method to predict neonatal condition in pregnancy care [85]. Hosni et al. propose an ensemble learning method to classify lung cancer [86].

2.6 Human Eye Modelling and Human Vision Simulation

With the development of ophthalmology and computer science, especially the exploration of the causes of pathological vision and the requirement for the pre-evaluation of the refractive surgeries, the studies begin to focus on how to model the human eye and simulate the human vision accurately. For human eye modelling, it is mainly formed an image on the retina by using a combination of the spherical lenses as the optical media of the eyeball. These studies are focus on the schematic human eye model. For human vision simulation, it is mainly expressed the defocus blur effect in the scene by using various types of blur. These studies are focus on the methods and technologies of human vision simulation.

2.6.1 Schematic Eye Model

Schematic eye model is a model based on the human eye's optical characteristics based on the anatomy of the human eye. There are some schematic eye models proposed for emmetropia modelling. Gullstrand firstly proposed a human eye model in 1909. This model includes some spherical lenses to simulate the optical structure of the human eye. The optical properties and the anatomical structure of the human eye are both considered in this model. This model provides the foundation of the later study of human eye modelling. In 1911, Gullstrand received the Nobel Prize for his work [87]. In 1980, Grand improved Gullstrand's eye model and proposed Gullstrand-Le Grand eye model. This model takes the aspheric surface of the cornea into account [88]. In 1985, Navarro et al. propose a novel human eye model which takes the accommodation process into account. Navarros model takes the focus ability of the human eye into account. It is suitable for objects with different distance [89]. In 1999, to be compatible with the large-angle incident light, Escudero-Sanz and Navarro propose an improved Navarro eye model [90]. In recent years, Navarro eye model is widely used in the studies of human vision, e.g. intraocular lens design [91, 92], near-eye display system [93, 94], head-mounted display system [95, 96] and

the eyeball physiological structure [97, 98] and visual quality evaluation [99, 100, 101].

In summary, most studies focus on modelling healthy human eyes, but few studies focus on modelling pathological human eyes. The main reason for this situation is that the causes of pathological vision are complicated. For example, the causes of myopia include genetic factors, drug factors, abnormal lens refractive power, abnormal axial length and other unknown reasons. It is a complex system still with multiple unknown factors. The models lack medical interpretation and rationality. For example, if the myopic eye model only considers changes in the refractive power of the eyeball and do not consider changes in the axial length of the eyeball. This model does not conform to the actual medical situation.

2.6.2 Human Vision Simulation

To accurately simulate the human vision, the schematic human eye model is considered as a group of spherical lenses. These lenses are integrated into a ray-tracing rendering engine. The rendering results provide the simulation of the human vision.

There are some studies using ray tracing to simulate the defocus blur in DoF effects. The methods used in these studies can be divided into two categories: one is the multi-pass method [102, 103, 104, 105] and the other is the post-processing method [106, 107, 108, 109]. The multi-pass method can achieve accurate DoF effect simulation by computing the positions where the image plane intersects with multiple rays. Due to the high computation cost and long rendering time, the method cannot be used for real-time rendering. On the other hand, the post-processing method is to reduce the amount of computing by pre-processing the blur level of the vertex for the pixels in the image plane, e.g. blur distribution function (BDF). This method can increase the rendering speed, but it will reduce the accuracy of the DoF effect. However, all of the above methods generate the DoF effect based on the thin lens principle and do not consider the change of the axial length and the thickness of the lens caused by the pathological eyeball and the refractive surgery, so it cannot accurately describe the change in DoF effect before and after refractive surgery.

Therefore, in Chapter 5, an improved schematic human eye model is proposed. The variables of the axial length and the corneal thickness are added into Navarro eye model. It is suitable for both normal and pathological eyeball and human vision, included em-

metropia, myopia, hyperopia and post-refractive surgeries. Moreover, an improved pre-processing algorithm is proposed to obtain BDF to compute the defocus blur of DoF effect.

2.7 GPU-Accelerated Related Work

The GPU-based parallel computing is similar to SMP, with shared system bus and memory, but it integrates thousands of computing cores in one chip. It is a highly cost-effective method for parallel computing.

The concept of GPU was defined in the mid-1990s. Initially, the function of GPU was a co-processor to complete the 3D graphics acceleration, including triangle drawing, materials, texture and lighting. The architecture of this GPU was not programmable. For the complicated 3D graphics functions in the Computer-Aided Design software and the video games, the concept of 3D graphics application programming interface (API) is presented for accessing the rendering pipeline, e.g. DirectX and OpenGL.

Around 2000, with the advent of programmable GPU, the concept of programmable shaders was proposed. Subsequently, three relatively advanced shader languages were proposed, e.g. High-Level Shading Language (HLSL), OpenGL Shading Language (GLSL) and C for Graphics (Cg). Since programmability vertex and rasterization units were added to the architecture of GPU as part of rendering pipeline, the developer turned the scientific computing problems into graphics processing problems and then used shader language to complete the coding and computing. At that time, GPU-based parallel computing has not entirely escaped the constraints of graphics processing, not general computing on the GPU.

In 2003, the Stanford University graphics group, Ian Buck and partners, proposed Brook which is based on Cg and is a variant of ANSI C. Brook was early and influential attempts to general-purpose computing on GPU [110]. In the Brook and later, the developers do not care about graphics processing problems caused by different shading languages generated. In 2007, NVIDIA created a GPU-based parallel computing platform named Computer Unified Device Architecture (CUDA) for general-purpose computing. The CUDA platform is designed for working with a high-level language, e.g. C/C++ and Fortran [111]. With the CUDA platform, developers do not need advanced skills in shader language programming at all. As a software layer between developers and GPUs,

the CUDA platform supports direct access to the instruction set and parallel computing units in the GPUs. The developers have lower-level control of parallel operations and can optimize parallel programs. In 2008, Khronos Group released the Open Computing Language (OpenCL) specification. OpenCL is a framework for parallel programs what execute on heterogeneous systems consisting of CPU, GPU, Digital Signal Processor (DPS), Field Programmable Gate Array (FPGA) and other processors. OpenCL provides a unified programming environment based on C/C++. OpenCL can support GPUs designed and manufactured by Intel, AMD and NVIDIA.

However, to adapt to the normal execution of different CPUs, GPUs and devices, OpenCL has made some sacrifices in performance. In 2010, NVIDIA published a ray tracing engine based CUDA technology, named OptiX [112]. There are some studies for human vision simulation based on OptiX [113, 114]. However, because the OptiX is controlled and maintained by NVIDIA, that is, OptiX only provides some APU. The accuracy of the ray tracing algorithm of the OptiX is hard to measure. On the other hand, the optimization of OptiX is determined by the hardware and NVIDIA. Therefore, it is necessary to design an accurate GPU-accelerated ray-tracing rendering engine to simulate human vision based on the improved schematic eye model and BDF.

2.8 Summary

In this chapter, the studies of the planning, prediction, and evaluation of the refractive surgery using machine learning-related methods are summarized. Based on the features of the dataset used in medical diagnostic modelling, the related studies of data interpolation, data resampling and ensemble learning is introduced. And then, the related studies of the human eye modelling and the human vision simulation are summarized. The reviews on the schematic eye model and defocus blur are focused. The previous work plays a guiding and enlightening role in the follow-up research of this thesis. In the next chapter, the dataset and the related pre-processing are introduced.

Chapter 3

Clinical Dataset and Data Pre-process

3.1 Overview

Refractive surgery has been proven to be the most effective treatment for myopia. Although patient satisfaction with LASIK surgery exceeds 90%, it may not be recommended for everyone. There are two main reasons: (1) for some patients, there may not be a significant visual improvement; (2) for some patients, it is not suitable for surgery or has side effects after surgery [115]. The thickness of the cornea to be ablated in the surgery determines whether the patient's cornea can be operated and the refractive power after the operation. These factors affect the patient's post-surgery vision. Currently, surgeons make predictions based on the patient's biological parameters, surgical parameters, theoretical formulas and some assumptions. This prediction is a theoretical result. Based on this result, surgeons can rely on their experience and make rough estimates of surgical outcomes based on the surgical equipment manual [116, 117, 118, 119]. The work presented in this thesis proposes a way based on medical data and machine learning methods to predict the surgery parameter and post-surgery outcome for a patient without theoretical formulas, assumptions, and surgeon experience. It could provide additional references for surgeons to adjust surgical parameters for better surgical results, and patients could receive the possible methods.

In this chapter, the process of Laser Assisted in-situ Keratomileusis (LASIK) is introduced for a better explanation of the following dataset researches in Section 3.2. And the

dataset used for this research is presented and analysed with statistical methods in Section 3.3. The multiple imputation method is proposed and tested for the missing data of the dataset in Section 3.4. Finally, in Section 3.5, the prediction regression model is proposed with this dataset to check whether machine learning could provide a better prediction than the theoretical formula and surgeon's experience.

3.2 Introduction of LASIK

LASIK is laser assisted in situ keratomileusis, which means using the excimer laser underneath a corneal flap (in situ) to reshape the cornea (keratomileusis). Before the LASIK surgery, the surgeon will examine the patients' eyes in detail. Age, gender, spherical equivalent, dioptre of spherical power and cylinder power, dioptre of spherical equivalent, the diameter of cornea, central corneal thickness and intraocular pressure (measured with non-contact tonometer) are recorded by the surgeon. As shown in Figure 3.1[120], it is a sample report of the LASIK [120].

The report is made by LASIK surgical equipment. There are two main parts in this report, the biological parameters and the surgery parameters. The biological parameters are input by the surgeon, who examined the patient's eye. The surgical equipment obtains the surgery parameters with an internal algorithm. With this report, surgeons could determine whether a patient is suitable for LASIK and the possible outcomes after surgery. The main surgery parameter is the maximum ablation depth. According to corneal features, to keep the stable structure of the cornea, the residual bed depth should greater than $250\ \mu\text{m}$. The residual bed depth is the difference of the central corneal thickness and the maximum ablation depth. The report is also used to guide the process of the surgery.

As shown in Figure 3.2[121], there are four main steps in the LASIK. During the LASIK procedure, a specially trained eye surgeon first creates a precise, thin hinged corneal flap using a microkeratome. The surgeon pulls back the flap to expose the underlying corneal tissue, and then the excimer laser ablates (reshapes) the cornea in a unique pre-specified pattern for each patient. The flap is then gently repositioned onto the underlying cornea without sutures.

As same as the majority of surgeries, there are some side effects after LASIK. Residual refractive error (RRE) is the commonest one. The post-surgery visual acuity is affected by the RRE. We had better predict the RRE before the surgery. The surgeon could adjust

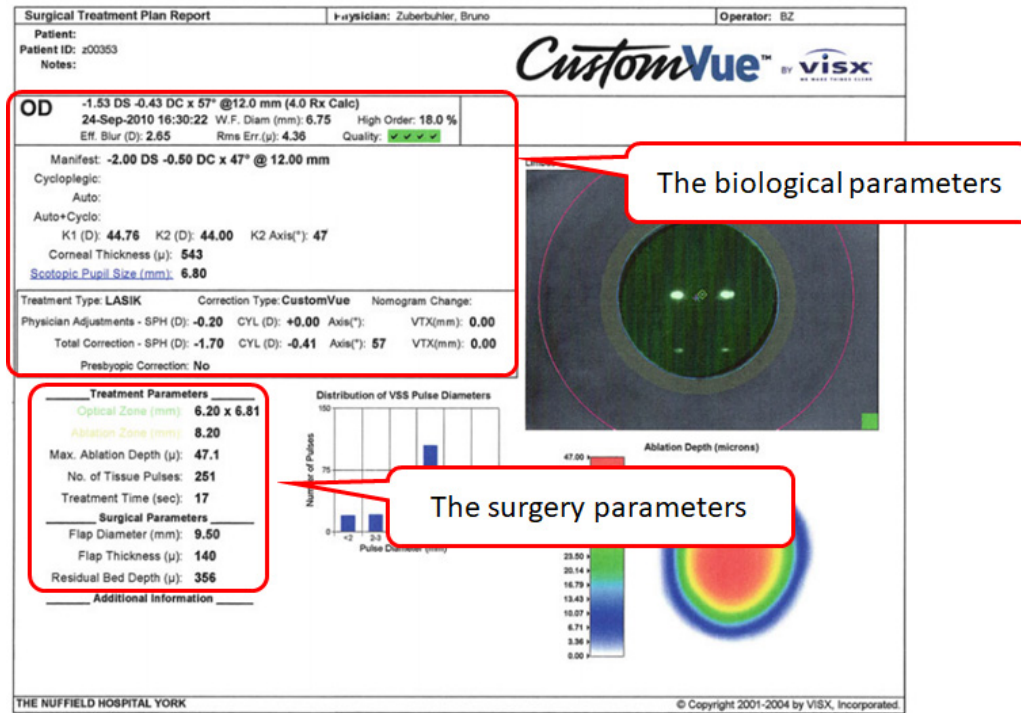


Figure 3.1: The sample report of the LASIK

the surgery parameters to reduce the RRE, and the patients could know the possible visual acuity after the LASIK surgery.

3.3 Refractive Surgery Dataset

In this study, the surgery data is collected from the Eye Hospital of Wenzhou Medical University (Zhejiang Eye Hospital) from 2013 to 2015. The original surgery data is recorded on paper which is similar to the reported shown in Figure 3.1. These data are entered into the computer and verified. The dataset has 30 items for 1559 eyes of 786 patients in total.

There are four items of patient demography, age, gender, preoperative examination date and surgery date. There are six items of preoperative examination, diopter of spherical power (SP) and cylindrical power (CP), astigmatism axial (AA), best-corrected visual acuity (BCVA), CCT and IOP with non-contact tonometer (NCT). The diopter of SP is about the spherical error. That means the image of human vision appears blurred in all

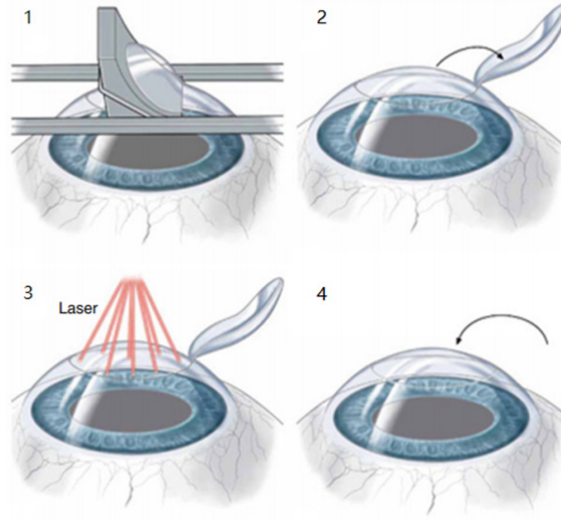


Figure 3.2: The process of the LASIK

meridians. The diopter of CP is the cylindrical error, which means the blurring only occurs in a single direction. The angle of this direction is described by astigmatism axial. The value of BCVA is a measurement of the best correction vision that can be achieved, such as with glasses. For example, if the patient's uncorrected eyesight is 20/200, which is tested by the Snellen eye chart, meanwhile, the patient can see 20/20 with glasses. That means that the BCVA of this patient is 20/20. For different locations on the cornea, the thickness of the cornea is different. The centre of the cornea is thicker than the rest of the cornea. CCT is a value used to describe the corneal thickness at the centre. The normal CCT value is around 510-520 μm . This value is measured by optical or ultrasound methods. Thicker cornea always means higher IOP. IOP is the fluid pressure inside the eye. The unit of IOP is millimetres of mercury (mmHg). In this dataset, the IOP is measured by NCT. The mean values and standard deviation of biological parameters are shown in Table 3.1.

There are five items of surgery parameters, optical zone diameter (OpD, in mm), cutting zone diameter (CuD, in mm), corneal flap thickness (CFT, in μm), residual corneal thickness (RCT, in μm) and corneal maximum ablation depth (CMAD, in μm). The optical zone is the laser ablation zone. The value of optical zone diameter is set by the

Table 3.1: Mean Values and Standard Deviation of Biological Parameters

Parameter	Mean Difference \pm Standard Deviation
Age (year)	23.91 \pm 5.95
Preoperative SP (diopter)	-5.16 \pm 2.12
Preoperative CP (diopter)	-0.82 \pm 0.69
Preoperative AA (degree)	86.85 \pm 73.55
Preoperative CCT (μ m)	540.62 \pm 30.47
Preoperative NCT (mmHg)	15.59 \pm 2.91
Preoperative BCVA	1.07 \pm 0.12

surgeons. The optical zone diameter should match the size of the pupil in the dark. Otherwise, after surgery, the patient may suffer permanent, debilitating visual aberrations, such as starbursts, halos, and multiples images at night. Therefore, generally, the optical zone diameter is always smaller than the largest size of the pupil. Most of optical zones diameter with modern laser refractive surgeries are from 6.0 mm to 6.5 mm. If the optical zone diameter is too large, the more corneal tissue will be removed during the surgery. If too much tissue is removed, the patient will likely develop a post-surgery complication, Keratoconus. There is an annular zone around the optical zone named the transition zone for a better surgery outcome. The transition zone is to avoid the night vision problem for the patients with large pupil size. The size of the transition zone is 0.5 mm to 1 mm larger than the pupil. The cutting zone diameter is a sum of optical zone diameter and the size of the transition zone. The corneal flap thickness is always a fixed value for one type of laser refractive surgery. It is determined by the surgery instruments and the surgeons. The residual corneal thickness is the ablated corneal central thickness without the corneal flap. The corneal maximum ablation depth is the maximum ablation depth in the centre of the optical zone. In theory, the central corneal thickness is a sum of corneal flap thickness, residual corneal thickness and corneal maximum ablation depth. To avoid the post-surgery complication, such as Keratoconus, the patient should have a minimum of 250 μ m of corneal thickness remaining after laser refractive surgery. Meanwhile, the scope of corneal ablation depth is determined by the correct refractive error, such as spherical power and cylindrical power. The maximum correctable refractive error is determined by the patient's central corneal thickness. The relationship among the pre-surgery biological parameters, surgery parameters and post-surgery outcomes could be described as a function in theory. The mean values and standard deviation of surgery parameters are shown

in Table 3.2.

Table 3.2: Mean Values and Standard Deviation of Surgery Parameters

Parameter	Mean Difference \pm Standard Deviation
OpD (mm)	6.58 \pm 0.42
CuD (mm)	7.72 \pm 0.37
CFT (μ m)	97.67 \pm 18.90
RCT (μ m)	348.46 \pm 31.46
CMAD (μ m)	93.40 \pm 24.26

The post-surgery outcomes are from three post-surgery examinations, diopter of spherical power and cylindrical, astigmatism axial, BCVA and IOP with NCT, the first week, the first month and the third month, respectively. The mean value and standard deviation are shown in Table 3.3.

Table 3.3: Mean Values and Standard Deviation of Post Surgery Outcomes

Parameter	Mean Difference \pm Standard Deviation
First-week Postoperative SP (diopter)	0.36 \pm 0.47
First-week Postoperative CP (diopter)	-0.36 \pm 0.34
First-week Postoperative AA (degree)	74.14 \pm 63.94
First-week Postoperative BCVA	1.05 \pm 0.19
First-week Postoperative IOP (mmHg)	11.19 \pm 2.88
First-month Postoperative SP (diopter)	0.32 \pm 0.47
First-month Postoperative CP (diopter)	-0.38 \pm 0.46
First-month Postoperative AA (degree)	76.69 \pm 64.42
First-month Postoperative BCVA	1.09 \pm 0.15
First-month Postoperative IOP (mmHg)	11.36 \pm 3.02
Third-month Postoperative SP (diopter)	0.30 \pm 0.46
Third-month Postoperative CP (diopter)	-0.37 \pm 0.33
Third-month Postoperative AA (degree)	74.73 \pm 62.84
Third-month Postoperative BCVA	1.13 \pm 0.29
Third-month Postoperative IOP (mmHg)	10.23 \pm 2.74

The data contains information for 786 patients in the age range of 16 to 51. 41 patients are under 18-year-old. LASIK surgery is not recommended in theory for patients under 18 years old. Five patients have single eye LASIK surgery. Four hundred nineteen patients

are females, and the rests are males. The histogram of preoperative SP is shown in Figure 3.3. One thousand five hundred fifty-four eyes are in the spherical power range of -1D to -12D, which are suitable for LASIK surgery in theory. All the patients' cylindrical power is suitable for LASIK surgery in theory. The central corneal thickness of 80 eyes are below $490\mu\text{m}$, and these are not suitable for LASIK surgery in theory. Fifty-seven of these have flapless LASIK surgery, and the rests have Femto-LASIK surgery. The post-surgery spherical power of 10 eyes is below -1D. Half of these eyes are super-high myopia (below -10D). There are 63 eyes which have an intra-ocular pressure out of the normal range (10mmHg-21mmHg). More than half of these (34 eyes) still have more than -0.5D spherical power after LASIK surgery. The histogram of CMAD is shown in Figure 3.4. Both of these two parameters are with a similar distribution. One of the hypotheses in regression analysis is normal data distribution. The normal q-q plot is used to check the variable data normal distribution. Figure 3.5 is the preoperative SP normal distribution. Figure 3.6 is the central corneal thickness (CCT) normal distribution. These two figures show that the normal data distribution is close to normal distribution. It can be used to model regression equations. There are four eyes which are presbyopia. All the data is collected manually, and some of the items are missing.

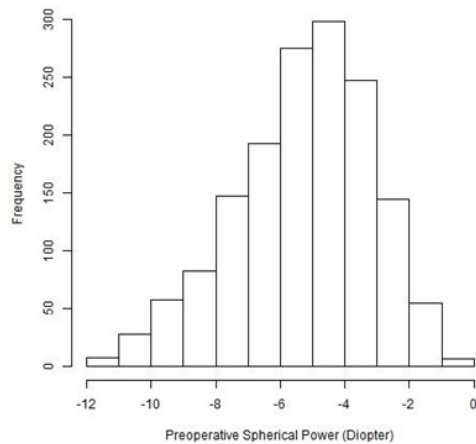


Figure 3.3: Preoperative SP Histogram

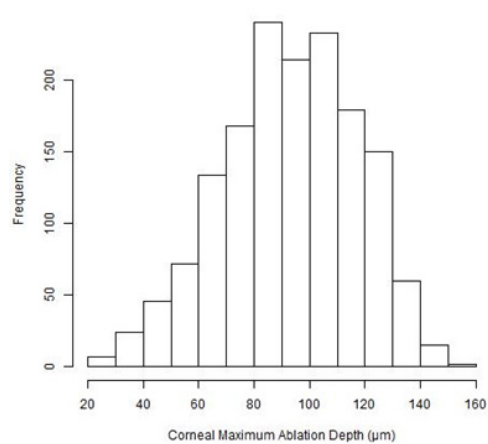


Figure 3.4: CMAD Histogram

Five patients only have single eye LASIK surgery, and the other five eyes which do not have any surgery parameters should be removed from the dataset. In Figure 3.7, there is

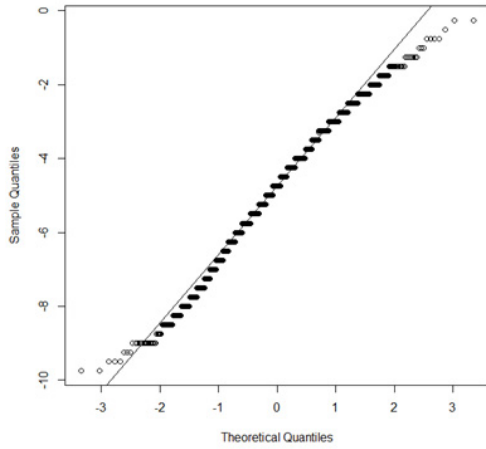


Figure 3.5: Preoperative SP Distribution

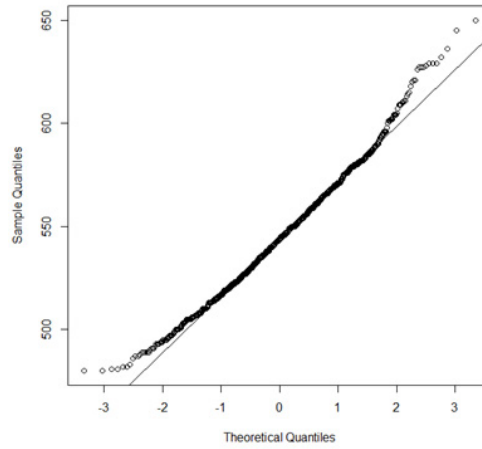


Figure 3.6: CCT Distribution

one eye missing pre-operative cylindrical power and axis. There are forty-four eyes missing cutting zone diameter data. Seventeen eyes are missing the first-week post-surgery data. Fifty-six eyes are missing the first-month post-surgery data. Thirteen eyes are missing the third-month post-surgery data.

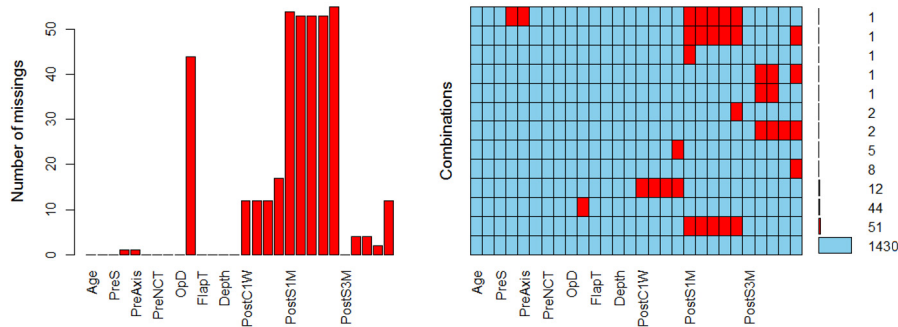


Figure 3.7: The missing data visualization

In the following sections, the multiple imputation for missing data is introduced. The first-month post-surgery SP is an example of this multiple imputation method. A regression model for predicting the CMAD is set as a test for this dataset.

3.4 Multiple Imputation for Missing Data

Since there are multiple methods for establishing a missing data fitted model, the combination of multiple interpolations is very flexible. The methods that can better respond the distribute of the missing data include Predictive Mean Matching (PMM), Bayesian linear regression, and ordinary linear regression. Due to a large number of previous works mentioned in Section 2.2, the relationship among the data of refractive surgery could be described by regression. In addition, the amount of missing data of the first-month post-surgery SP is the most in the dataset, and this research intends to take the imputation of this missing data as an example. By constructing a multiple regression equation of the missing data, the multiple imputation is implemented for the missing data. The results are compared with the PMM method and the Bayesian linear regression method to determine the appropriate multiple imputation method for the dataset.

The stepwise regression is used for regression model variable selection. In each step, a variable is considered for addition to or subtraction from the set of explanatory variables based on some prespecified criteria. In this research, Akaike information criteria (AIC) and t-stats are used as the standards of fit effect.

$$AIC = 2k + n_{obs} \ln\left(\frac{SSR}{n_{obs}}\right) \quad (3.1)$$

k is the number of items.

n_{obs} is observed number.

SSR is sum square of residue.

The lower the AIC means the better-fit effect. There are eight explanatory variables,, i.e., Age, Gender, Pre-operative spherical power (PreS), Pre-operative cylindrical power (PreC), Pre-operative cylindrical axis (PreAxis), Pre-operative BCVA (PreBCVA), Pre-operative non-contact tonometer result (PreNCT) and Pre-operative CCT (PreCCT). Table 3.4 shows the AIC values of each step in the First-month post-surgery SP regression.

Table 3.4: AIC Values of the First-month Post-surgery SP Regression

Initial	PreC	PreAxis	PreCCT
-8197.51	-8199.43	-8202.09	-8201.0

Table 3.5 shows the t-stats in regression, gender, and pre-operative BCVA are 0.1255

and 0.1195, which are above 0.1, and these are not significant. Therefore, gender, PreC, PreAxis, PreBCVA and PreCCT are rejected in the regression analysis.

Table 3.5: t-state of the first-month Post-surgery SP Regression

	Estimate	Std. Error	t Value	Pr(> t)
(Intercept)	0.656266	0.013856	47.362	$< 2e^{-16}$
Age	-0.134863	0.012056	-11.187	$< 2e^{-16}$
Gender	-0.006164	0.004022	-1.533	0.1255
PreS	-0.114833	0.018016	-6.374	$2.42e^{-10}$
PreBCVA	0.024392	0.015659	1.558	0.1195
PreNCT	-0.023430	0.014201	-1.650	0.0992

For the first-month Post-surgery SP regression, the regression equation is Formula 3.2.

$$Y = 0.656266 - 0.134863x_0 - 0.114833x_1 - 0.02343x_2 \quad (3.2)$$

Where Y is the first-month Post-surgery SP, x_0 is Age, x_1 is PreS, x_2 is PreNCT.

In Figure 3.8, result with this method are closer to the average value. Meanwhile, the root-mean-square error (RMSE) of the three methods is 0.32(PMM), 0.38(Bayesian linear regression) and 0.17(this method with multiple regression), respectively. Therefore, this method with multiple regression is suitable for the multiple imputation of the dataset.

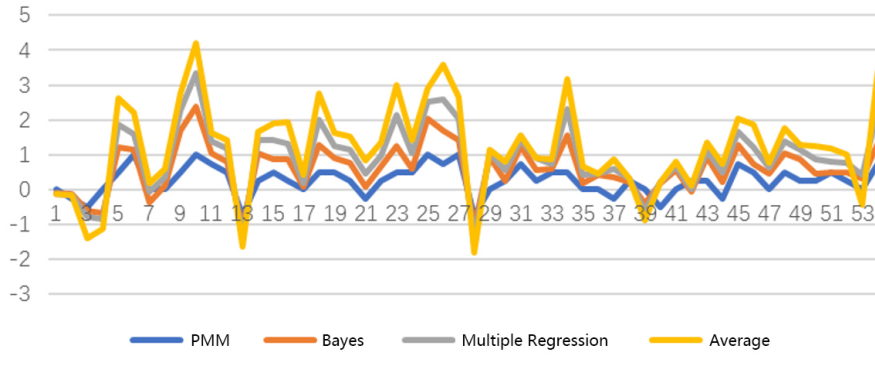


Figure 3.8: Multiple Imputation Methods

The rest of the missing data are imputed by this method. After the data imputation, the mean value and standard deviation are shown in Table 3.6. In the following section, the prediction of CMAD is a test for this dataset.

Table 3.6: Mean Values and Standard Deviation of All Measures

Parameter	Mean Difference±Standard Deviation
Age (year)	23.85±5.90
Preoperative SP (diopter)	-5.15±2.11
Preoperative CP (diopter)	-0.81±0.69
Preoperative AA (degree)	86.93±73.63
Preoperative CCT (μm)	540.81±30.24
Preoperative NCT (mmHg)	15.59±2.91
Preoperative BCVA	1.06±0.12
OpD (mm)	6.58±0.42
CMAD (μm)	93.38±24.15
the first-month Postoperative SP (diopter)	0.35±0.46
the first-month Postoperative CP (diopter)	-0.35±0.34

3.5 Prediction of CMAD

For the prediction of CMAD, the biological features and optical zone diameter are considered as the known conditions of the regression equations. The prediction model of CMAD is studied by correlation and regression analysis. The QR decomposition algorithm is used to complete the regression linear fit in R. A P-value of less than 0.05 is statistically significant.

The correlation is calculated between ablation depth and other parameters with a Pearson correlation coefficient for judging whether the ablation depth and other parameters have a high correlation, as shown in Tables 3.7 and 3.8.

Table 3.7: Correlation between Ablation Depth and Other Parameters

	Age	Gender	Preoperative SP	Preoperative CP	Preoperative Axis
Correlation	0.05	0.07	-0.85	-0.35	0.03

Table 3.8: Correlation between Ablation Depth and Other Parameters

	Preoperative CCT	Preoperative NCT	Preoperative BCVA	Preoperative OpD	Preoperative SP	Preoperative CP
Correlation	0.05	0.07	-0.17	-0.53	0.19	-0.19

According to the correlation among the parameters, preoperative spherical power, preoperative cylindrical power and optical zone diameter have a high correlation with corneal maximum ablation depth. The three parameters are used in the multiple regression. The correlation of the ablation depth and the preoperative spherical power is the highest than others; therefore, the preoperative spherical power will be used in single regression, separately.

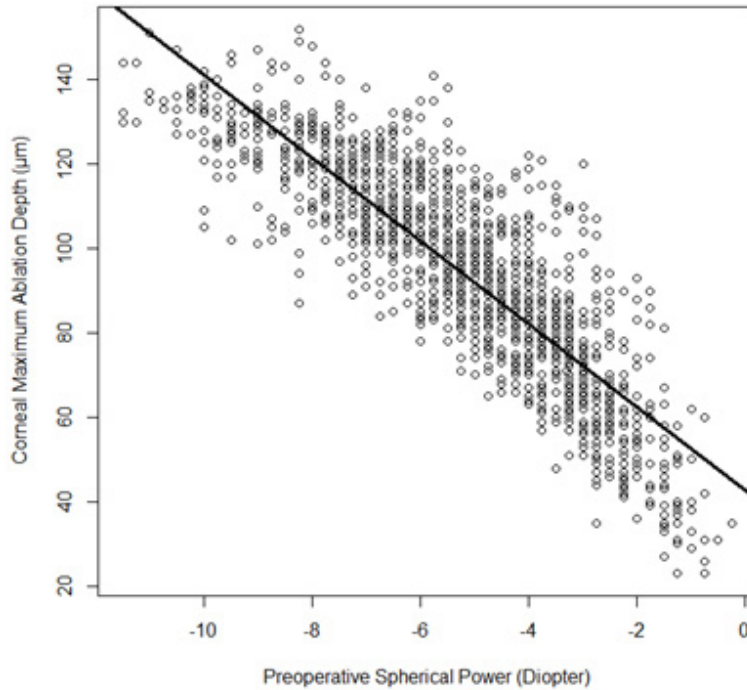


Figure 3.9: Linear Regression between Preoperative SP and CMAD

For the preoperative SP and CMAD regression, as shown in Figure 3.9, the regression equation is shown below. The residual standard error (σ) is $12.36\mu\text{m}$. The R-squared is 0.738. The P-value is less than $2.2e^{-16}$.

$$Y = 42.7577 - 9.8297x \quad (3.3)$$

where Y is expected ablation depth. x is preoperative SP.

For the multiple regression, the regression equation is shown below. The residual

standard error (σ) is $8.35\mu\text{m}$. The R-squared is 0.8806. The P-value is less than $2.2e^{-16}$. The multiple regression is with less residual standard error and greater R-squared values than single linear regression.

$$Y = -146.0074 - 13.1426x_0 - 11.9439x_1 + 24.5865x_2 \quad (3.4)$$

where Y is expected ablation depth. x_0 is preoperative SP. x_1 is preoperative CP. x_2 is OpD.

The predictions are compared between the regression equation and Munnerlyn approximate formula [116] for the evaluation of the regression equation.

$$\text{ApproximateAblationDepth} = \frac{|OZ|^2}{3}D \quad (3.5)$$

OZ is optical zone diameter. D is the correction in dioptres.

The mean-squared-error (MSE) is a measure of the quality of an estimator. The root-mean-square error (RMSE) is a measure of accuracy, to compare forecasting errors of different models for a particular dataset and not between datasets. For the prediction model with regression, MSE and RMSE can be used to evaluate the accuracy. The comparison includes the mean difference, MSE and RMSE, and the results are shown in Table 3.9. The multiple regression equation with less MSE and RMSE means the accuracy is better than the accuracy of Munnerlyn approximate formula.

Table 3.9: Comparison of Multiple Regression and Munnerlyn Approximate Formula

	Mean Difference	MSE	RMSE
Multiple Regression Equation	0.01016±6.104959	69.49518	8.336161
Munnerlyn Approximate Formula	21.5491±8.148693	584.3581	24.1735

3.6 Summary

The chapter presents an overview of the refractive surgery. In this chapter, the dataset used in this research is analysed in detail, including the distribution of data values and the distribution of missing data. The multiple imputation with the multiple regression method is proposed for the missing data. Compared with PMM and Bayesian linear regression methods, this RMSE of this method is less than the other two methods. It is suitable for

the dataset used in this research. In the final part of this chapter, the prediction of CMAD with regression methods is implemented as an initial test of the dataset. The results are proved more accurate than the Approximate Ablation Depth formula used by the surgeon. It is initial proved that the machine learning method could provide a more reasonable and accurate prediction in refractive surgery. In the following chapter, the furthermore work are done for improving the accuracy of the model obtained by machine learning methods.

Chapter 4

Prediction of Surgery Outcomes

4.1 Overview

In the refractive surgery, the surgeon and patient need to evaluate the surgery outcome. The surgeon performs the prediction with the patient's biology features, surgery parameters, theoretical formulas and hypotheses. This prediction could roughly estimate the surgery outcomes. With the popularity of refractive surgery, the clinical data are enough to implement a surgery outcomes prediction with machine learning methods, including regression, support vector machine and neural network. However, as the imbalanced data distribution, these data-driven methods still have drawbacks, including poor accuracy, high data size request and limited interpretability in the minority class. This chapter introduces an over-sampling method to improve these situations in the surgery outcome prediction. The approach over-samples the minority class to achieve better performance and accuracy. With the experiment, it is obtained a much more accurate result than that with an imbalanced dataset. Also, this method solves the result interpretability issue and the small data size issue in medical cases. Meanwhile, in order to solve the data sparseness problem and improve the accuracy of the model, an ensemble learning method with genetic algorithm optimisation is proposed in this chapter. The comparison between this method and other machine learning methods shows that this method is good at sensitivity and specificity and makes less error in false positives fraction (FPF) and false negative fraction (FNF).

In this chapter, the imbalanced data distribution of the dataset is analysed in Section 4.2. The over-sampling method is proposed and verified in Section 4.3. In Section 4.4, the

ensemble learning method with genetic algorithm optimisation is proposed and verified for improving the accuracy of the model. In Section 4.5, the method proposed in this chapter is compared with other machine learning methods.

4.2 The Imbalanced Data Distribution

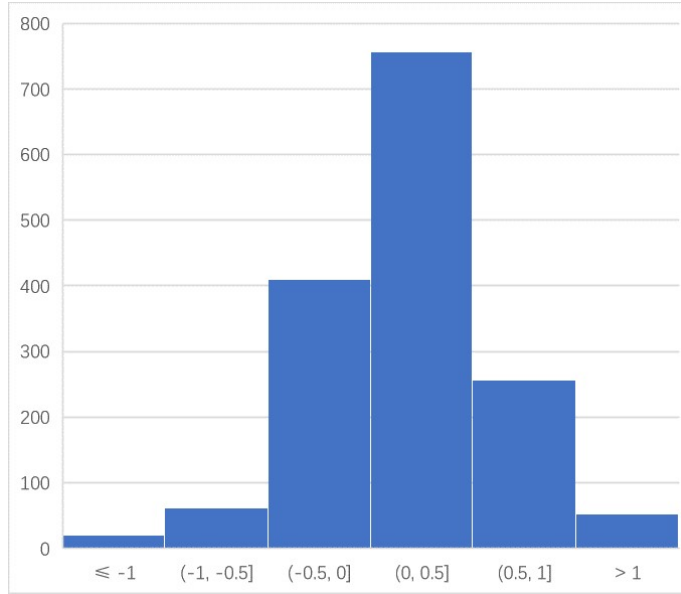


Figure 4.1: The distribution of 3-month Post-surgery SP

In this study, the clinical data were collected from the Eye Hospital of Wenzhou Medical University (Zhejiang Eye Hospital) from July 2013 to March 2015. The case records of 1559 eyes of 786 patients. Dataset obtained from the case records included patient age, gender preoperative spherical power (SP, in diopter) and cylindrical power (CP, in diopter), astigmatism axial value (Axis), best-corrected visual acuity (BCVA), central corneal thickness (CCT, in μm) and IOP with non-contact tonometer (NCT). Dataset also obtained five items of surgery parameters, optical zone diameter (OpD, in mm), cutting zone diameter (CuD, in mm), corneal flap thickness (Flap, in μm), corneal residual thickness (RT, in μm) and corneal maximum ablation depth (CMAD, in μm). The third-month post-surgery spherical power (SP) data what is more stable than the first week and first-month post-surgery data relatively are selected as the surgery outcomes. The dataset contains

information for 786 patients in the age range of 16 to 51. 419 patients are females, and the rests are males. The histogram of post-surgery SP is shown in Figure 4.1. The distribution is imbalanced. The majority of post-surgery SP is between -0.5 and 0.5 diopter. The sample of post-surgery outcome is imbalanced.

As the imbalance of the postoperative outcomes, in this study, the post-surgery SP can be classified into two groups. In Group 1, the absolute value of post-surgery SP is greater than 0.5 diopter, it is an unacceptable result. In Group 2, the absolute value of post-surgery SP is less than or equal to 0.5 diopter. It is an acceptable result. The comparison between the two groups is shown in Table 4.1.

Table 4.1: Biometrics, Refractive and Treated Parameters

	Group 1 (n = 359)	Group 2 (n = 1200)
	Mean±SD	Mean±SD
Age	23.59±6.07	24.00±5.91
Preoperative SP	-5.50±2.10	-5.05±2.11
Preoperative CP	-0.88±0.70	-0.80±0.69
Preoperative Axis	86.89±73.30	86.83±73.60
Preoperative BCVA	1.07±0.11	1.07±0.12
Preoperative NCT	15.47±2.89	15.63±2.92
Preoperative CCT	540.15±31.93	540.76±30.02
OpD	6.52±0.42	6.60±0.42
CuD	7.73±0.36	7.71±0.37
Flap	97.28±20.12	97.78±18.51
RT	343.39±28.62	349.98±32.10
CMAX	98.65±22.42	91.83±24.56

Therefore, the prediction of the postoperative outcome has transformed itself from numerical prediction into classification. In the following section, an over-sampling method is proposed to solve the imbalance of dataset. In addition, to improve the accuracy of the neural networks classifier, the members of input and hidden layer are also be selected by mean impact value (MIV) and mean square error (MSE).

4.3 The Over-sampling Method

In this section, the original imbalanced dataset is tested by backpropagation (BP) neural networks as the baseline. By the over-sampling method, the dataset can be reconstructed. After the selection of input and hidden layer member, the balanced dataset is tested again. The result will compare with the baseline.

4.3.1 The Baseline for Evaluation

At first, an initial test should be done for evaluating the performance of the data in the classified prediction. With backpropagation (BP) neural networks (with one hidden layer and the size of the hidden layer is 5), the dataset is divided into training and validation dataset. One thousand one hundred sixty-nine eyes (75%) are the training dataset, and 390 eyes (25%) are the validation dataset. The initial test results are shown by the confusion matrix in Table 4.2.

Table 4.2: The Confusion Matrix without Over-sampling

	Predicted Acceptable	Predicted Unacceptable
Actual Acceptable	296	3
Actual Unacceptable	90	1

4.3.2 The Over-sampling Method

It is a limited recall on the minority class (unacceptable results) while maintaining a high precision on the majority class. Although the SMOTE method mentioned in Section 2.4 could provide a better performance in the majority imbalanced dataset. However, the dataset used in this research is complex. The majority and minority class is mixed together and determined by multiple variables. Using SMOTE method resampling, the dataset may produce much more noise data. And it makes the model uncertain direction bias. Therefore, in this research, with the imbalanced dataset, an improved over-sampling method is proposed to resample the minority data. This method pays more attention to the mixed area between majority class and minority class and checks the synthetic examples,

which may be the noise in the dataset. The algorithm is shown below:

Algorithm 1 The Over-sampling Algorithm

Input: S : minority class; L : majority class; T : total dataset; F : mixed area dataset; m : size of S ; n : size of F ; p_i : data of minority class; q_j : data of mixed area set; $i \in [1, m]$; $j \in [1, n]$; r : size of synthetic data;

Output: over-sampled minority class S'

```

1: for each  $i \in [1, m]$  do
2:   Compute  $m$  nearest neighbours of  $p_i$  in  $T$ . This set is called  $M$ 
3:   Let  $q = |M \cap L|$ 
4:   If  $q = m$ ,  $p_i$  may be a noisy point. Reject  $p_i$  and continue to next point.
5:   If  $0 \leq q \leq \frac{m}{2}$ ,  $p_i$  may be minority class point. Reject  $p_i$  and continue to next point.
6:   If  $\frac{m}{2} < q \leq m$ ,  $p_i$  may be a mixed area point. add  $p_i$  to mixed area set  $F$ .
7: end for
8: initial  $S'$ 's length with  $n(r + 1)$ ;
9: for each  $j \in [1, n]$  do
10:  Compute  $k$  nearest neighbours of  $q_j$  in  $F$ ;
11:  Randomly choose  $r \leq k$  of the neighbours;
12:  Choose a random data  $q'_r$  along the line joining  $q_j$  and each of the  $r$  selected neighbours;
13:  Add  $q'_r$  to  $S'$ ;
14: end for
15: Add  $S$  to  $S'$ 
16: Output  $S'$ 

```

In this algorithm, k is assigned 3, and r is assigned 3. The comparison among Group 1, Group 1 with synthetic data and Group 2 is shown in Table 4.3.

Table 4.3: Biometrics, Refractive and Treated Parameters with Over-sampling

	Group 1	Group 1 with Over-sampling	Group 2
	(n = 359)	(n = 1077)	(n = 1200)
	Mean±SD	Mean±SD	Mean±SD
Age	23.59±6.07	23.01±4.96	24.00±5.91
Preoperative SP	-5.50±2.10	-5.51±1.96	-5.05±2.11
Preoperative CP	-0.88±0.707	-0.87±0.61	-0.80±0.69
Preoperative Axis	86.89±73.30	86.83±73.39	86.83±73.60
Preoperative BCVA	1.07±0.11	1.08±0.09	1.07±0.12
Preoperative NCT	15.47±2.89	15.43±2.47	15.63±2.92
Preoperative CCT	540.15±31.93	539.96±30.82	540.76±30.02
OpD	6.52±0.42	6.53±0.36	6.60±0.42
CuD	7.73±0.36	7.75±0.31	7.71±0.37
Flap	97.28±20.12	97.60±19.77	97.78±18.51
RT	343.39±28.62	342.87±26.75	349.98±32.10
CMAX	98.65±22.42	98.94±20.98	91.83±24.56

4.3.3 The Prediction Model of Surgery Outcome

In this study, the BP neural networks is selected as the classifier. To optimum, the BP neural networks , the mean impact value (MIV) is introduced to select the member of the input layer. There are 13 input layer candidates, include age, gender, Preoperative SP, Preoperative CP, Preoperative Axis, Preoperative BCVA, Preoperative NCT, Preoperative CCT, OpD, CuD, Flap, RT and CMAX. Because the RT is the difference between preoperative CCT and Depth, it is multicollinearity. RT will remove from the input layer. The MIV of these input layer candidates is shown in Table 4.4.

Table 4.4: Mean Impact Value

	Mean Impact Value
Age	0.266
Gender	-0.1089
Preoperative SP	0.1003
Preoperative CP	0.0021
Preoperative Axis	-0.1710
Preoperative BCVA	0.0266
Preoperative NCT	-0.0054
Preoperative CCT	-0.1238
OpD	1.7141
CuD	0.1423
Flap	-0.0755
CMAX	-1.2674

According to the absolute value of MIV, age, gender, preoperative SP, preoperative Axis, preoperative CCT, OpD, CuD, Flap and Depth are selected as the input layer mem-

bers. The mean square error (MSE) is used to decide the size of the hidden layer member. The MSE values with different size of the hidden layer are shown in Table 4.5. The lowest MSE is seven members in the hidden layer. Therefore, the construction of the member classifier is nine members in the input layer, seven members in the hidden layer and one member in the output layer. The dataset is divided into two parts, 1977 eyes (75%) is the training dataset, and 659 eyes (25%) are the validation dataset.

Table 4.5: MSE of different numbers of member in hidden layer

Number of members	Mean Square Error
1	0.91
2	0.64
3	0.61
4	0.62
5	0.63
6	0.67
7	0.59
8	0.63
9	0.60
10	0.64
11	0.60
12	0.63
13	0.64

4.3.4 Results and Analysis

With the over-sampling method, although the predictive accuracy is about 67.98%, lower than the baseline, 76.15%. The accuracy of predicted unacceptable results is 34.90%, much higher than the baseline, 0.25%. The specificity of the model is 65.90%, much greater than

the baseline, 1.09%. Therefore, the prediction model with the over-sample method provides better performance than the baseline model. The confusion matrix is shown in Table 4.6.

Table 4.6: Confusion Matrix with Over-sampling

	Predicted Acceptable	Predicted Unacceptable
Actual Acceptable	218	92
Actual Unacceptable	119	230

In the following section, the ensemble learning method and optimization algorithm are used to combine a novel ensemble learning method to improve the accuracy of the model.

4.4 The Ensemble Learning with Genetic Algorithm Optimization

As mentioned in the previous section, by resampling the imbalanced dataset, the accuracy of the model could be improved. However, using a single machine learning method may receive limited accuracy, which is only better than a random guess. The prediction error is composed of two components: bias, the accuracy of the predictor; and variance, the precision of the predictor when trained on different training sets. Meantime, these two components have a trade-off relationship: predictors with low bias tend to have high variance and vice versa. On the other hands, some mathematical methods have smoothing (variance-reducing) effect, i.e. averaging. Hence, in this section, the accuracy of prediction can be significantly improved through an ensemble of neural networks , i.e. training several neural networks with relatively fixed or similar bias and then combining the outputs reduce the variance. The motivation for combining neural networks in redundant ensembles is that of improving their generalisation ability. Combining a set of imperfect basis predictors can be thought of as a way of managing the recognised limitations of the individual predictors; each component neural networks is known to make errors, but they are combined in such a way as to minimise the effect of these errors. In order to obtain more accurate results, the initial weights and thresholds of the basis predictors are optimised by the genetic algorithm

(GA).

4.4.1 The Optimisation Algorithm

GA is employed to optimize the initial weight and threshold of basis predictor. The purpose of the optimization is to improve the output accuracy of the basis predictor. The optimization includes five steps:

1. Population Initialization

The individual coding method is a real number based coding method. The individual code is a real number string which includes the weights between the input layer and hidden layer, the weights between the hidden layer and output layer, the hidden layer thresholds and the output layer threshold. Therefore, the string includes all weights and thresholds used by the neural network.

2. Fitness Function

The training set is used to train the BP neural network. By this BP neural network, the result of the predicted output is compared to the value of the desired output. The sum of the absolute values of the errors in individual fitness, F . The function of F is as follows:

$$F = k \left(\sum_{i=1}^n \text{abs}(y_i - o_i) \right) \quad (4.1)$$

In this function, n is the number of output node in BP neural network. y_i is the value of the desired output of output node i in BP neural network. o_i is the value of the predicted output of output node i in BP neural network. k is coefficient

3. Selection Operation

The selection operation employs the roulette method, which is fitness-proportionate selection. The probability p of each individual i is as follows:

$$f_i = \frac{k}{F} \quad (4.2)$$

$$p_i = \frac{f_i}{\sum_{j=1}^N f_j} \quad (4.3)$$

f_i is the fitness-proportionate of individual i . k is coefficient. N is population size.

4. Crossover Operation

The individual is coded by a real number string. Therefore, the real number crossover method is employed in this step. The k -th chromosome a_k and the l -th chromosome a_l perform the crossover operation at position j with the function which is as follow:

$$\begin{cases} a_{kj} = a_{kj}(1 - b) + a_{lj}b \\ a_{lj} = a_{lj}(1 - b) + a_{kj}b \end{cases} \quad (4.4)$$

b is between 0 and 1.

5. Mutation Operation

To complete the mutation operation at the j -th chromosome a_j of i -th individual, the mutation operation function is as follow:

$$f(g) = r_2 \left(1 - \frac{g}{G_{max}}\right) \quad (4.5)$$

$$a_{ij} = \begin{cases} a_{ij} + (a_{ij} - a_{max}) * f(g)r \geq 0.5 \\ a_{ij} + (a_{min} - a_{ij}) * f(g)r < 0.5 \end{cases} \quad (4.6)$$

a_{max} is the upper bound of the chromosome a_{ij} . a_{min} is lower bound of the chromosome a_{ij} . r_2 is a random number, g is the current iterative time. G_{max} is the maximum evolution time. r is between 0 and 1

4.4.2 The Ensemble Learning

In order to ensemble several predictors together, the first step is the initialisation of the training and testing datasets and the basis predictors. Because of the limited size of the dataset using in this research, it uses Bootstrap method for sampling to obtain multiple the training and test datasets for training the different predictor. As mentioned in the previous section, the structure of the basis predictor is defined by MIV method and optimised by GA. With the training and testing datasets and the basis predictors, the basis predictors are trained. The sum of the prediction error of each predictor is e_t . If the e_t is greater than 0.5, that is, the accuracy of this predictor is worse than a random guess. This predictor should be rejected. If the e_t is lower than 0.5, the prediction weight of this predictor is computed. According to the prediction weights of the basis predictors, the weights of the training datasets are modified. After several loops, the final predictor could be obtained

by the combination of the final rest of basis predictors.

The pseudocode of this ensemble algorithm is as follow:

Algorithm 2 The Ensemble Algorithm

Input: $Trainingdata = \{x_i, y_i\}, i = 1, \dots, m, y \in \{\omega_1, \dots, \omega_i\}$ K ensemble size of the basis predictor

Set $D(i) = \frac{1}{m}$

2: **for** each $t \in [1, K]$ **do**

Use *Bootstrap* method sampling the dataset to obtain the subset S_t from the distribution D_t .

4: Train Basis Predictor on S_t , receive hypothesis $h_t : X \rightarrow Y$

Calculate the error of h_t :

6: $e_t = \sum_{i=1}^m D(i)(h_t(x_i) \neq y_i)$
 $e_t > \frac{1}{2}$ abort.

8: Set the prediction weight of the basis predictor as a_t :

$$a_t = \frac{1}{2} \ln\left(\frac{1-e_t}{e_t}\right)$$

10: Update sampling distribution

$$D_{t+1} = D_t(i) * \frac{\exp[-a_t y_i h_t(x_i)]}{B_t} \quad i = 1, \dots, m$$

12: Where $B_t = \sum_{i=1}^m D(i)$ is a normalization constant to ensure that D_{t+1} is a proper distribution function.

end for

14: Given unlabeled instance z , obtain total vote received by each class

$$V_c = \text{sign}\left[\sum_{t=1}^K k a_t \cdot f(h_t, a_t)\right]$$

Output: Class with the highest V_c .

The core of this algorithm is the distribution update rule: the distribution weights of the instances correctly classified by the current hypothesis h_t are reduced by a fact of e_t , whereas the weights of the misclassified instances are left unchanged. When the updated weights are renormalized by B_t to ensure that D_{t+1} is a proper distribution, the weights of the misclassified instances are effectively increased. Therefore, with each new classifier added to the ensemble, the algorithm focuses on increasingly tricky instances. At each iteration t , this step raises the weights of misclassified instances such that they add up $\frac{1}{2}$, and lowers those of correctly classified ones, such that they too add up to $\frac{1}{2}$. Since the basis predictors optimized GA is required to have an error less than $\frac{1}{2}$, it can guarantee to

classify one previously misclassified training example correctly at least. When it is unable to do so, the algorithm aborts; otherwise, it continues until K classifiers are generated, which are then combined using the weighted majority voting.

4.4.3 Results and Analysis

With BP neural networks and over-sampling algorithm, the predicted accuracy is 67.95%. The confusion matrix is shown in Table 4.6. With the ensemble algorithm, the predicted accuracy is about 71.32%. The genetic algorithm initial parameters are shown in Table 4.7:

Table 4.7: Genetic Algorithm Initial Parameters

Initial Parameters	
Iterations	100
Population Size	200
Probably of Crossover	0.6
Probably of Mutation	0.4

With GA optimisation, the ensemble learning method combines 25 basis prediction. The predicted accuracy is about 76.09%. The accuracy of predicted unacceptable results is 37.56%, greater than the over-sample method model, 34.90%. The specificity of the model is 79.02%, greater than the over-sampling method model, 65.90%. Therefore, the prediction model with the GA optimised ensemble learning method provides better performance than the baseline. The confusion matrix is shown in Table 4.8.

Table 4.8: Confusion Matrix with Final Model

	Predicted Acceptable	Predicted Unacceptable
Actual Acceptable	282	102
Actual Unacceptable	73	275

4.5 Summary

The study has achieved a data-driven model automated method to obtain a possible surgery outcome, the postoperative spherical power, with genetic algorithm optimized ensemble learning. According to the results, for the medical diagnosis, the genetic algorithm optimized ensemble learning is proved that it could improve the prediction accuracy of the model. In the following chapter, the methods of human eye modelling and human vision simulation are proposed.

Chapter 5

Simulation of Human Vision using Ray Tracing

5.1 Overview

The human eye is a complex and precise optical imaging system. The external light signals are projected onto the retina, converted into electrical signals, and then transmitted to the brain to reconstruct the image through neurons. However, the human eye may suffer from a variety of diseases caused a refractive error, such as common myopia and hyperopia. Earlier methods to correct the refractive error were mainly by wearing glasses or contact lenses. In recent years, excimer laser technology has widely used in clinical medicine, especially in refractive error treatment of ophthalmology. The refractive surgeries based on excimer laser technology, e.g. Photorefractive Keratectomy (PRK), Laser-assisted in situ Keratomileusis (LASIK) and Small-incision Lenticule Extraction (SMILE), aim to correct the refractive error of the human eye. As the requirements of visual quality become higher, refractive surgeries are also developing personally. To accurately predict and evaluate the refractive surgery, the modelling of the human eye should be achieved first.

The normal monocular vision could be described as Figure 5.1. Compared with the original scene (Figure 5.2), in human vision, only the very central part of the scene can be focused correctly. The rest of the scene is defocused. Because the brain forms a clear vision through rapid eyeball movements, it is difficult to perceive such images. Modelling the human eye is useful in many studies, e.g. the prediction and the evaluation of refractive

surgeries, the design intraocular lens and progressive lenses, and other ophthalmic studies. It is also meaningful as information visualisation for the studies that are related to the human vision, e.g. the design of near-eye display systems and virtual reality systems. However, it still lacks an accurate human eye modelling method to simulate the refractive error of the human eye.



Figure 5.1: The Normal Monocular Vision



Figure 5.2: The Original Scene

To accurately model the human eye, the ray-tracing method is widely used. However, the simplified thin-lens camera which produces the depth-of-field (DoF) defocus blur effect

in the ray-tracing method cause the scene distortion. The computation cost of the ray tracing and the defocus blur make this method impossible to render in real-time. Wu et al. [122] use ray tracing method based on Navarro eye model. This method treats each eyeball optical media as a spherical lens. An incident ray is refracted by these lenses and forms an image on the retina. The refractive power of each optical media has been considered in this model. However, the axial length, which is the primary factor of myopia, is not considered in this model.

In this study, a novel approach is proposed to achieve the personalised modelling of the human eye, and the visual quality visualised evaluation of refractive surgeries. This approach adds an extra-axial length variable for myopia based on the Navarro eye model and improves the computation of defocus blur with a blur distribution function (BDF). Moreover, the BDF is calculated by the neural networks. In Section 5.2, the image-forming principle of the human eye and the principle of refractive surgeries are introduced. The improved eye model is proposed in Section 5.3. The process of establishing BDF and the method of calculation with a machine learning method is discussed in Section 5.4. Section 5.5 analyses the results and evaluates this model. The summary of this chapter is in Section 5.6.

5.2 The Related Basis Principles

For a better understanding of the modelling the human eye, the image-forming principle of the human eye and the principle of the refractive surgery are introduced firstly.

5.2.1 The Image-forming Principle of Human Eye

Figure 5.3 is an abridged general view of the human eye. As shown in Figure 5.3, the main structure of the human eye in the direction of incident light includes the cornea, aqueous humour, pupil, lens, vitreous and retina. The cornea and lens are two primary refractive media of the human eye. Due to the density difference between media, such as air and cornea, cornea and aqueous humour, aqueous humour and lens, lens and vitreous, the light will be refracted on the four surfaces before and after the cornea and lens. The curvature of the four surfaces has a significant impact on visual quality. The refractive power of the human eye without any adjustment is called static refractive power, and the

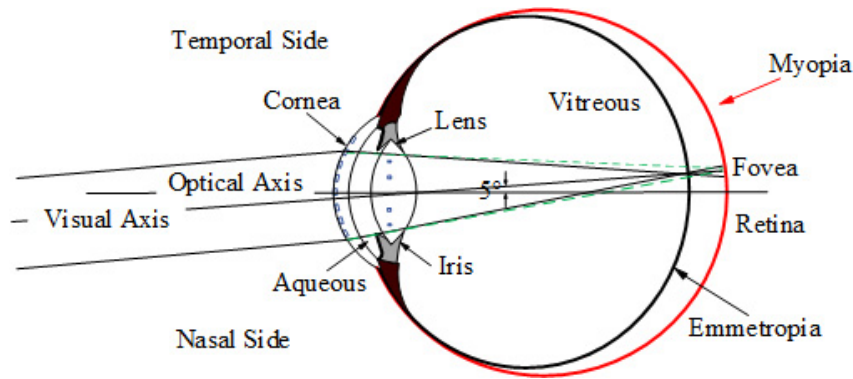


Figure 5.3: The Abridged General View of Human Eye

static refractive power of the standard human eye (emmetropia) is $+58.64D$. Generally, the corneal refractive power can be adjusted from $+42.0D$ to $+44.0D$. The cornea provides most of the refractive power of the human eye. Refractive surgery is mostly achieved by changing the corneal curvature the aperture of pupil changes with the brightness of the ambient light. The retina, like a photodetector, is a light-sensitive tissue that converts light signals into neural electrical signals. Between the optical axis and visual axis, there is a Kappa angle of 5 degrees off nose side. For the emmetropia, the total refractive power of the eyeball matches the axial length of the eyeball.

Meanwhile, the incident light can focus on the retina after passing through the various optical media of the eyeball, thereby obtaining good vision. For myopia, there is a mismatch between the axial length of the eyeball and its refractive power. As shown in Figure 5.3, a red arc indicates an increase in the size of the vitreous increases and the axial length, causing the position of the retina to move backwards. The defocus blur occurs when the size of the defocused light spot is larger than the retinal resolution. Approximately $1mm$ backwards produces $+3.0D$ spherical power. The principle of corneal refractive surgeries to correct the refractive error is to cut the corresponding amount of corneal stroma to flatten the front surface of the cornea. As shown in Figure 5.3, the green dotted line shows that the total refractive power matches the longer length of the eyeball.

5.2.2 The Principle of Refractive Surgery

LASIK is based on the image-forming principle of the human eye. LASIK performs a spherical cutting with the guidance of the Munnerlyn formula. As shown in Figure 5.3, the principle of the spherical cutting is to cut the corresponding amount of corneal stroma to flatten the front surface of the cornea. After the surgery, the curvature radius of the front corneal surface R_c^* is increasing. Meanwhile, the corneal refractive error is reduced. The post-surgery corneal front surface could be represented as below:

$$Z_c^{[s]}(\rho) = \frac{\frac{\rho^2}{R_c^*}}{1 + \sqrt{1 - \frac{\rho^2}{R_c^*}}} \quad (5.1)$$

$$R_c^* = \frac{(n_c - 1)R_c}{S_E R_c + (n_c - 1)} \quad (5.2)$$

In Formula 5.2, n_c is the corneal refractive index. S_E is the spherical equivalence which is used to represent the defocus value of myopia. ρ -factor is the aspheric parameter. In surgery, a $100\mu m$ corneal flat is created, and the excimer laser ablates the corneal stroma. The relationship between ablation depth and horizontal radius is represented as below:

$$\Delta Z_c^{[s]}(\rho) = \frac{\sqrt{R_c^2 - (1 + Q)\rho^2}}{1 + Q} - \frac{\sqrt{R_c^2 - (1 + Q)(\frac{O}{2})^2}}{1 + Q} - \sqrt{R_c^{*2} - \rho^2} + \sqrt{R_c^{*2} - (\frac{O}{2})^2} \quad (5.3)$$

O is the diameter of the pupil. Q is the coefficient of aspheric surface. After surgery, the Q becomes 0. During the practical ablation, the ablation depth is always calculated by the parabolic approximation of the Munnerlyn formula. It is a simplified Munnerlyn formula which is represented by the corrected dioptre of spherical equivalence, the ablation zone diameter and the radial distance from the optical axis. This simplified Munnerlyn formula assumes that the corneal refractive index n_c is 1.375.

$$s(y) = \frac{4Dy^2}{3} - \frac{Dd^2}{3} \quad (5.4)$$

As shown in Formula 5.4, $s(y)$ is the ablation depth in micrometre (μm), D is the refractive error (in dioptre) which will be corrected, d and y are the diameter of the ablation zone and the radial distance from the optical axis in millimetre (mm) separately. This simplified

Munnerlyn formula is widely applied to the evaluation and the performance of refractive surgeries. With the ablation depth, the post-surgery corneal thickness could be calculated.

According to the principle of human eye imaging and the principle of refractive surgery, in order to accurately describe the situation of emmetropia, myopia, hyperopia and refractive surgery, the changes in axial length and corneal thickness should be considered in the human eye model.

5.3 Methodology

The target of this study is to model the human eye and simulate the human vision for visual quality evaluation of refractive surgeries. As mentioned in Section 2.6 and Section 5.2, the pathological vision is complicated. The change of the refractive power of the eyeball is only a manifestation of the pathological vision. The cause of the pathological vision is the change of the axial length. In addition, Refractive surgery adjusts the refractive power by changing the corneal thickness. Therefore, to accurately model the human eye and simulate the human vision, the changes of the axial length and the corneal thickness are added into the schematic human eye model. Since the Navarro eye model has been widely used in various types of human vision simulation studies, by modifying this model, it can inspire more human vision studies. In this study, Navarro eye model is chosen.

On the other hand, in order to accurately describe the defocus blur of DoF effect in human vision simulation, while reducing the computation cost of ray tracing, this study introduces a BDF in human vision simulation. BDF is different from the computation of the Circle of Confusion (CoC) in the multi-pass method. Since BDF is a complex unknown expression with multiple inputs and multiple outputs, it could be considered as a black box system with multi-input and multi-output. In order to derive the expression of BDF, this study uses the neural networks to find the relationships between the input variables and output results. As shown in Figure 5.4, the process of human vision model and simulation contains two stages, the human eye model stage and the human vision simulation stage.

5.3.1 Modelling the Human Eye

As shown in Figure 5.5, in the human eye model stage, there are four main parts in the human eye model, cornea, pupil, lens and retina. The surface and media of the cornea

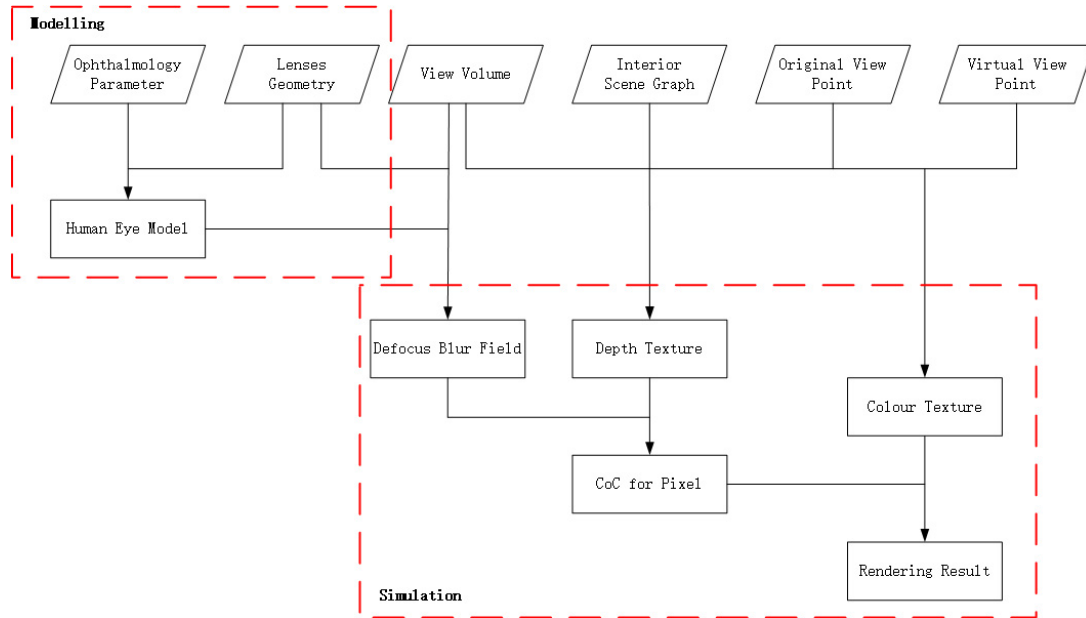


Figure 5.4: The Process of Human Vision Model and Simulation

and lens provide the refractive power which could be considered as the lens of a camera. The pupil could be considered as the aperture of a camera which controls the amount of incident ray. The retina could be considered as the film of a camera. The optical properties of a fully relaxed eye (the unaccommodated state) are shown in Table 5.1.

Table 5.1: The Optical Properties of a Fully Relaxed Eye

	Surface	Pos	Rad	Asph	Thick	Ref	Aper
Cornea	1	0.0	7.72	-0.26	0.55	1.367	12
	2	0.55	6.5	0	3.05	1.3374	12
Lens	3	3.6	10.2	-3.1316	4	1.42	10
	4	7.6	-6	-1	16.3203	1.336	10
Retina	5	24.4	-12	0	0	0	24

As mentioned in Section 5.2, because of the difference of the refractive index between the optical media, there are four optical refracture surfaces in the eyeball, including air to the cornea, cornea to aqueous, aqueous to the lens, lens to vitreous. The optical properties

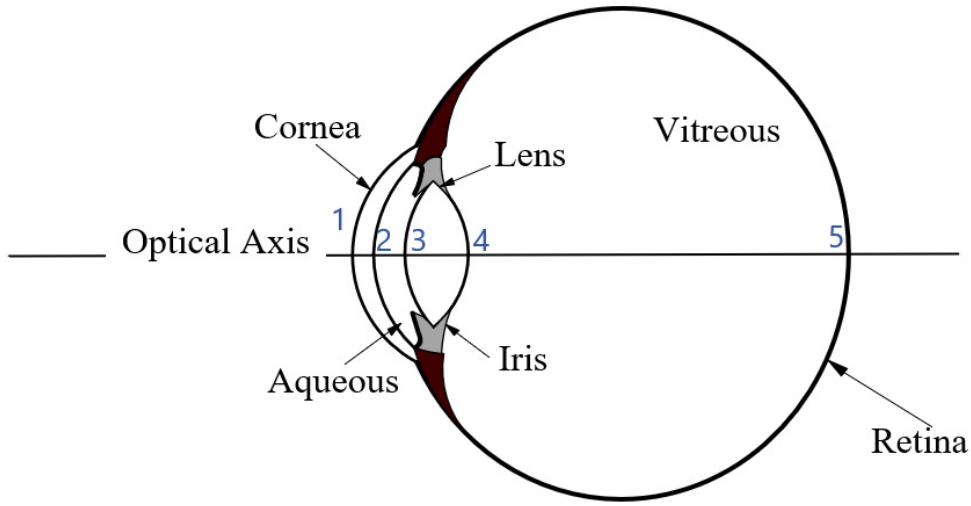


Figure 5.5: The Anatomical Structure of the Human Eyeball

of the anterior and posterior surfaces of the cornea and lens are considered in the eye model. In addition, because of the relationship the increasing of the axial length for myopia, as shown in Formula 5.4, the variable of the retina position is considered in the eye model.

$$\Delta L = \frac{1000}{S + \Delta s} - \frac{1000}{S} \quad (5.5)$$

In Formula 5.5, ΔL is the change of the axial length (in mm), Δs is the spherical equivalent of the refractive error (in dioptre). S is the total refractive power of the emmetropia (in dioptre). In this formula, the value of S is $+58.64D$. The human eye can accommodate the lens to focus the incident ray accurately on the retina within a reasonable range. According to the study of Navarro [89], the relationship among the spherical equivalent of the refractive error and the properties of the optical media are shown below.

$$R_{S3} = 10.2 - 1.75 \ln(\Delta s + 1.0) \quad (5.6)$$

$$R_{S4} = -6.0 + 0.2294 \ln(\Delta s + 1.0) \quad (5.7)$$

$$T_{aqueous} = 3.05 - 0.05 \ln(\Delta s + 1.0) \quad (5.8)$$

$$T_{lens} = 4.0 + 0.1\ln(\Delta s + 1.0) \quad (5.9)$$

$$Q_{S3} = -3.1316 - 0.34\ln(\Delta s + 1.0) \quad (5.10)$$

$$Q_{S4} = -1.0 - 0.125\ln(\Delta s + 1.0) \quad (5.11)$$

$$n_{index} = 1.42 + 9.0 \times 10^{-5} \ln(\Delta s + 1.0) \quad (5.12)$$

In these formulas, Δs is the spherical equivalent (in diopter) of refractive error. R_{S3} represents the accommodated front radius of the lens (in mm) when the refractive error is Δs . R_{S4} represents the accommodated posterior radius of the lens (in mm) when the refractive error is Δs . $T_{aqueous}$ is the accommodated thickness of the aqueous (in mm) while the refractive error is Δs , and T_{lens} is the accommodated thickness of the lens (in mm) while the refractive error is Δs . The accommodated front aspheric degree after lens adjustment is Q_{S3} , and the accommodated posterior aspheric degree after the lens is Q_{S4} . The accommodated total refractive index is represented as n_{index} .

For the refractive surgeries, since the corneal thickness is changed. The front radius of the cornea is changed. According to the simplified Munnerlyn formula (Formula 5.4) mentioned in Section 2, the front radius of the cornea R_{S1} is represented below.

$$R_{S1} = \sqrt{\frac{3\Delta t}{4\Delta s} + \frac{d^2}{4}} \quad (5.13)$$

In Formula 5.13, Δt is the corneal ablation depth (in mm), d is the diameter of the ablation zone (in mm), Δs is the corrected refractive error (in dioptre).

According to the image-forming principle of the human eye and the principle of the refractive surgeries, this study improved the Navarro eye model. The change of the axial length and the change of corneal front radius are considered in this schematic eye model. In the following section, this improved model is analysed by visualising the anatomical structure of the human eye and the path of the incident light.

5.3.2 Human Vision Simulation

As shown in Figure 5.6, in the human vision simulation stage, there are online rendering section and offline computing section.

In the offline computing section, the ray-tracing method is used to compute the refraction and occlusion with the schematic eye model and the ophthalmologic parameters.

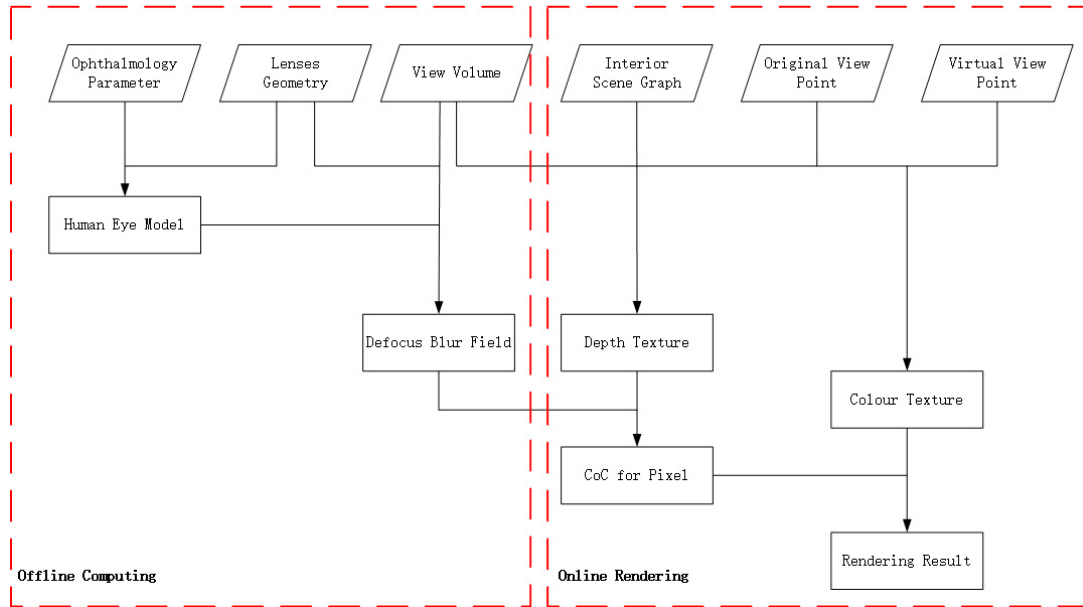


Figure 5.6: The Framework of Human Vision Simulation

By sampling the ophthalmologic parameters (focus distance and pupil size), object position (distance and angle from the observer), and the image information on the retina, a training dataset is established. With the neural networks, the blur distribution function (BDF) is obtained to describe the CoC size of each pixel of the image on the retina. If the schematic eye model and the ophthalmologic parameters are fixed, the BDF is constant; that is, the offline computing section only needs to execute once. In the online rendering section, the texture rendering of the rendering pipeline is divided into two parts. One is the colour texture used to compute the material and the light effect. The other is depth texture, which is used to compute the three-dimensional (3D) space position corresponding to each pixel by the reconstructing the scene. After that, the 3D space position is converted into the spherical coordinate; the origin of this spherical coordinate is the observer position. The spatial position and the observer's visual ophthalmologic parameters are used together as the inputs of the BDF derived by the offline computing section. Then, the BDF is solved, and the CoC size of the pixel of the image corresponding to the 3D spatial position is obtained. Finally, according to the CoC size and colour texture, a blurred/clear rendered image is obtained. For a better explanation of the process, the CoC calculation is introduced firstly.

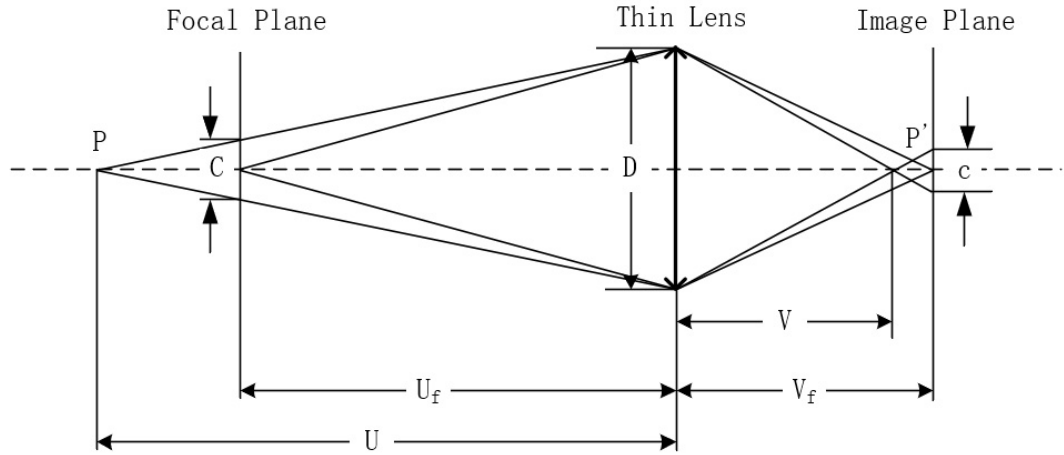


Figure 5.7: The CoC Calculation

As shown in Figure 5.7, in a thin lens optical system, the distance between the image plane and the surface of the lens V_f could be calculated by Formula 5.14.

$$V_f = \frac{U_f * f}{U_f - f} \quad (5.14)$$

U_f is the distance between the focal plane and the surface of the lens. And f is the focal length of the thin lens, D is the diameter of the lens. The relationship between V_f and U_f is represented as the magnification m .

$$m = \frac{V_f}{U_f} \quad (5.15)$$

With the similar triangle theory, in the focal plane, the diameter of the blur disk, C , produced by point P can be expressed as

$$C = D * \frac{|U - U_f|}{U} \quad (5.16)$$

U is the object distance and represents the distance between P and the surface of the lens. Therefore, the CoC size, c , could be obtained by the product of m and C .

$$c = mC = D * \frac{|U - U_f| * V_f}{U_f * U} = D * \frac{|U - U_f| * f}{U(U_f * U)} \quad (5.17)$$

The CoC size is determined by the lens diameter, focal length, object distance and focal distance. For a thin lens system, the thickness of the lens is 0, the CoC is always assumed to be circular, and the distribution of blurring is uniformly distributed. However, for a real lenses system, e.g. the human eye, including multiple lenses, the CoC size and distribution is complicated and non-linear. It is difficult to calculate for the complex optical system.

In this study, the neural networks provide a possible way to obtain the CoC size and distribution using the correlative factors, such as the focal length, the lens diameter and the object distance. The CoC size and distribution function is described as below

$$BDF(F, P, R_m, \Theta_m, \phi_m) \quad (5.18)$$

BDF is a multivariate function consisting of five parameters. In this function, F represents the focal length of the human eye. According to the principle of the thin lens, the different focal length is the direct cause of the different CoC sizes. Meanwhile, the pupil size, P , which is similar to the diameter of the thin lens, is also the cause of the different CoC size. The object distance and angle should also be considered in the function; therefore, m is the point of the scene formed at the pixel p position in the image. R_m, Θ_m and ϕ_m are spherical coordinates corresponding to m point position and the origin of the spherical coordinate system where m is located in the centre of the front corneal surface in the eye model.

For deriving function BDF , the improved Navarro eye model is used to generate a sample dataset for the training neural networks. By tracing the rays from different point position in the 3D scene, the areas where the ray intersects on the retina are recorded as the sample dataset. The sampling algorithm is shown in Algorithm 3.

Algorithm 3 The Sample Intersection Point Algorithm

- Set model focus as F
 Set pupil diameter as P
 3: P_s is the point set evenly distributed points on the first lens
for each $p \in P_s$ **do**
 $ray \leftarrow rayoriginsat(R_m, \Theta_m, \phi_m)pointingtop$
 6: $oray \leftarrow SchematicEyeModel(ray)$

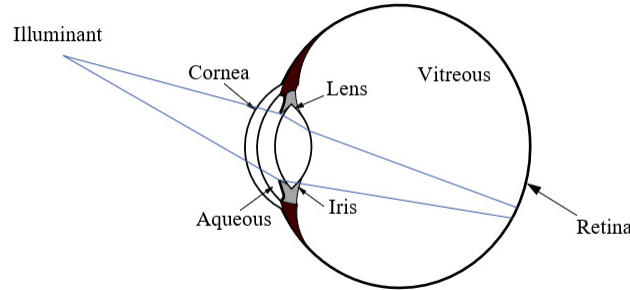


Figure 5.8: The Anatomical Structure View of the Intersection of the Ray

With Algorithm 3, the ray-tracing computing results corresponding to each set of values can be obtained. Then, the position of the 3D intersection point of the ray cone and the retina is converted into 2D pixel coordinates of the retinal image. Figure 5.8 is an anatomical structure view of the intersection of the ray cone and the retina, and Figure 5.9 is the 2D schematic ray intersection view after conversion. Since the shape of the intersection areas is irregular, this study uses a 2D rectangular envelope method to represent the size of the intersection area. By obtaining the height, h , and width, w , of the rectangle, Gaussian blur is applied to the rectangle area for the corresponding pixel.

There are seven dimensionalities in the sample dataset, including five input items and two output items. It could be considered BDF as a multiple regression function, $D(F, P, R_m, \Theta_m, \phi_m)$, that is, for the i -th input items $(F^i, P^i, R_m^i, \Theta_m^i, \phi_m^i)$, there are the output items, w^i and h^i . $i \in [1, n]$, and n is the amount of the intersection point of the ray on the retina. This multiple regression function could be optimised by minimizing the least-squares error:

$$E = \sum_{i=1}^n \|(w^i, h^i) - D(F^i, P^i, R_m^i, \Theta_m^i, \phi_m^i)\|^2 \quad (5.19)$$

On the other hand, the neural networks could be used to model the regression function and find the closed-form solution for this multiple regression function. The back-propagation neural network is selected for fitting the non-linear regression function. In this process, for better performance and generalisation of the neural networks, with several testing, the mean squared error (MSE) of closed-form fitting is set as $1 * 10^{-2}$. The structure of the

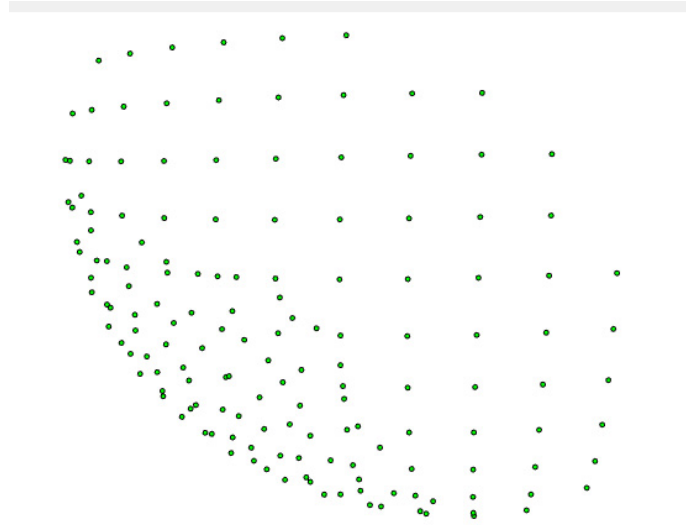


Figure 5.9: The 2D Schematic View of the Intersection of the Ray

neural networks is two hidden layers with 12 nodes separately. With the training, the final MSE of the neural networks is $1.9587 * 10^{-4}$. While $\sigma = \frac{1}{1+e^{-x}}$ the CoC size could be represented as below.

$$[w^i, h^i] = \sum_{k>0} w_{jk}^2 \sigma \left(\sum_{i>0} w_{ki}^1 x_i + b_k^1 \right) + b_j^2 \quad (5.20)$$

In this section, an improved schematic human eye model is proposed. This model takes into account the changes in the axial length and the corneal thickness for the pathological vision and the refractive surgeries, respectively. In addition, a novel method is proposed to obtain a BDF function for the CoC size and the defocus blur in DoF effects. In the following section, the improved schematic model and BDF function are verified and analysed.

5.4 Results and Analysis

5.4.1 The Improved Human Eye Model

In order to evaluate the improved human eye model, with the ray-tracing method, the incident ray path is illustrated on the anatomical structure of the human eye. As shown in

Figure 5.10, The emmetropia is simulated by the improved human eye model accurately. The incident rays are correctly focused on the retina. In Figure 5.11, the ray intersection points of the retina could reflect the real situation which the rays could be focused in the centre of the retina. In Figure 5.11, there are some disperse points around the central focus, which are the aberration of the human eye. For example, at night, a distant point light source is often recognized as the star shape by the human eye.

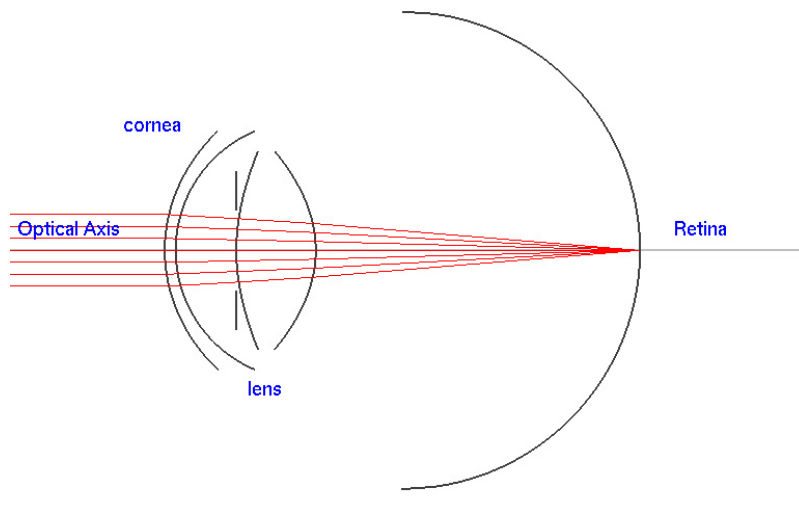


Figure 5.10: The Incident Ray Path of Emmetropia with the Improved Human Eye Model

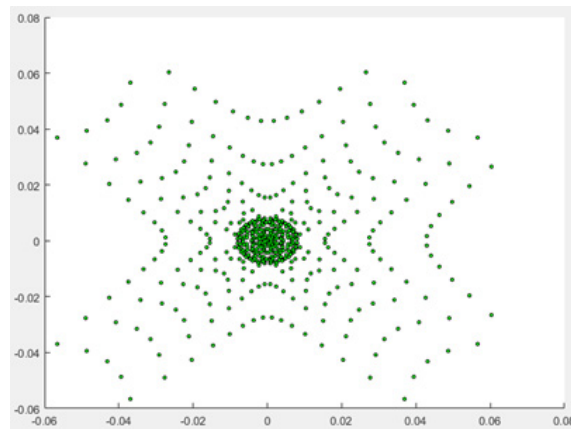


Figure 5.11: The Intersection Points of Incident Rays on the Retina

Figure 5.12 illustrates the near object, which is 50mm from the central point of the front corneal surface. The incident rays are not correctly focused on the retina. This situation is also reflected in Figure 5.13. The intersection points of incident rays on the retina are spread like circle shape. The distance between any two points is greater than $30\mu m$. The size of the typical retinal neural cells is only $2-4\mu m$. It causes severe defocus blur in human vision. It is consistent with real-world experience.

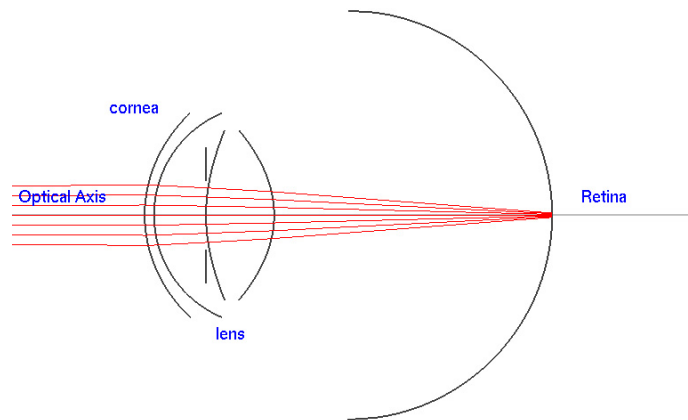


Figure 5.12: The Incident Ray Path of Emmetropia for Near Object

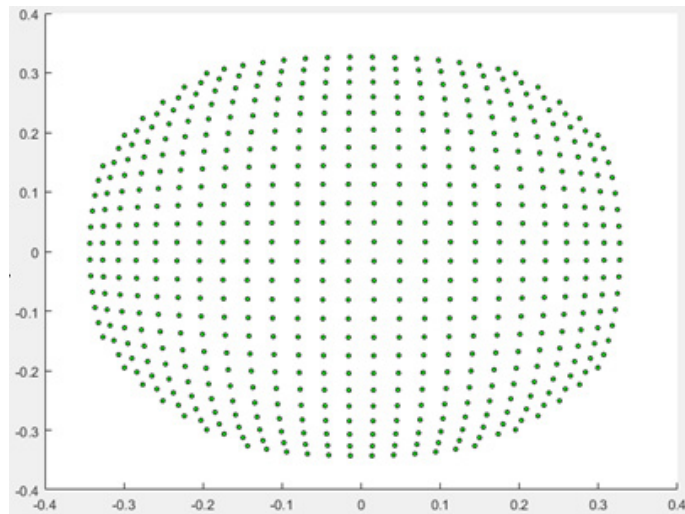


Figure 5.13: The Intersection Points of Incident Rays for Near Object

The case of the large incident angle rays is illustrated in Figure 5.14. Due to the large incident angle, the incident rays can not be properly focused on the retina, resulting in a triangular aberration. As shown in Figure 5.15, the triangular aberration makes the blur vision. As in the real world, objects at the edges of the perspective are always blurred.

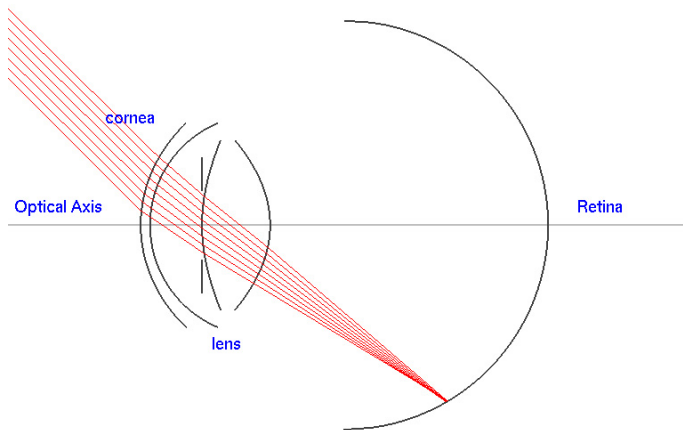


Figure 5.14: The Incident Ray Path of Emmetropia for Large Incident Angle

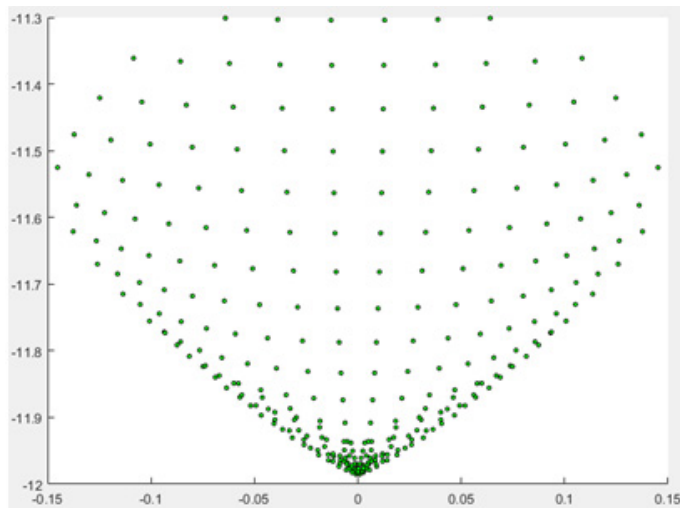


Figure 5.15: The Intersection Points of Incident Rays for Large Incident Angle

The cases of Myopia with a different refractive error are described in Figure 5.16 and

Figure 5.18. The incident rays have formed a circle of confusion on the retina with the increase of the axial length. With the different axial length, the shapes and the sizes of the circle of confusion are different, as shown in Figure 5.17 and Figure 5.19.

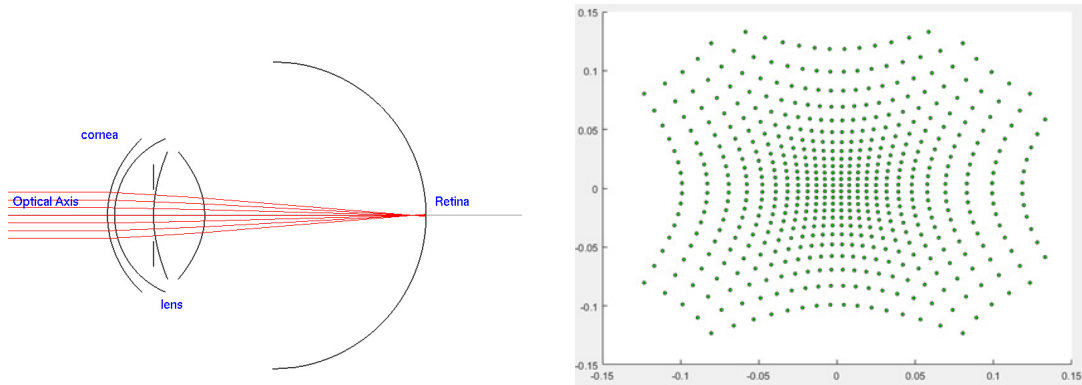


Figure 5.16: The Myopia with 1mm Additional Axial Length

Figure 5.17: The Retinal Intersection Points of Myopia with 1mm Additional Axial Length

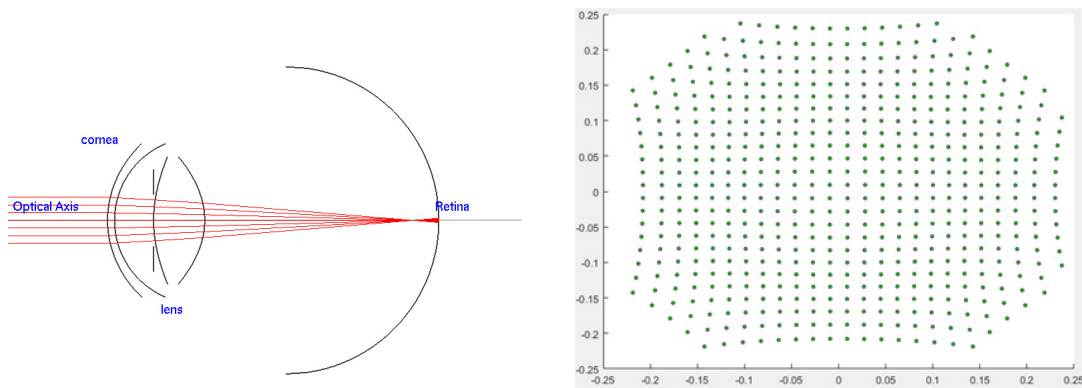


Figure 5.18: The Myopia with 2mm Additional Axial Length

Figure 5.19: The Retinal Intersection Points of Myopia with 2mm Additional Axial Length

According to the principle of refractive surgery, the corneal thickness is reduced by ablating the cornea. The refractive error is corrected by this process. The outcome of refractive surgery is illustrated in Figure 5.20. The $178\mu m$ corneal stroma is ablated, and

the -3.0D spherical equivalent refractive error is corrected by the surgery. In Figure 5.20, the incident rays are properly focused in the centre of the retina. The size of the spread is significantly larger than the emmetropic eye (Figure 5.21). That is aberrations caused by corneal ablation, which is also a side effect of LASIK. It may cause halo vision at night.

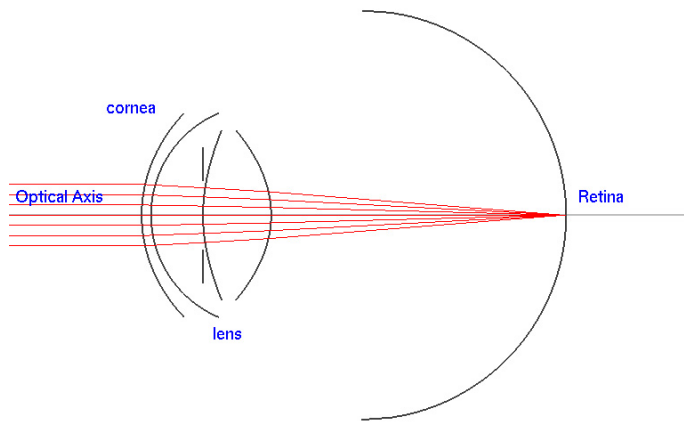


Figure 5.20: The Incident Ray Path of Post-surgery

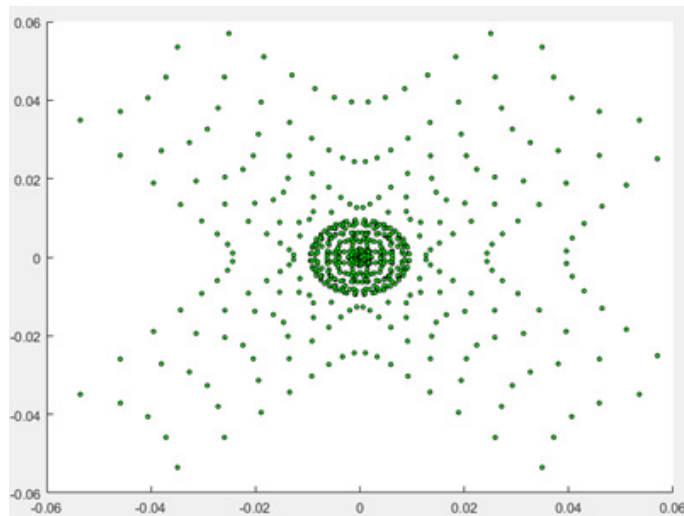


Figure 5.21: The Intersection Points of Post-surgery

If corneal stroma ablation exceeds what is required for refractive error, myopia will

not change to hyperopia simply. In Figure 5.22, after ablating $294\mu\text{m}$ corneal stroma, the -4.0D spherical equivalent refractive error is corrected to $+2.0\text{D}$. The incident rays should be focused behind the retina. A circle of confusion is formed on the retina. As shown in Figure 5.23, the defocus blur effect and size is different from myopia. Meanwhile, the aberration is also different.

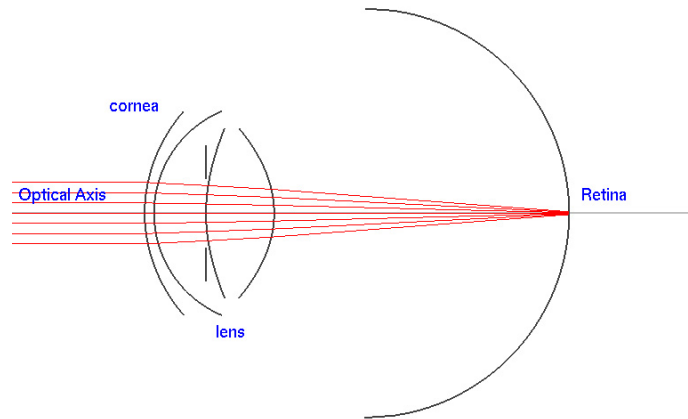


Figure 5.22: The Incident Ray Path of Overtreatment

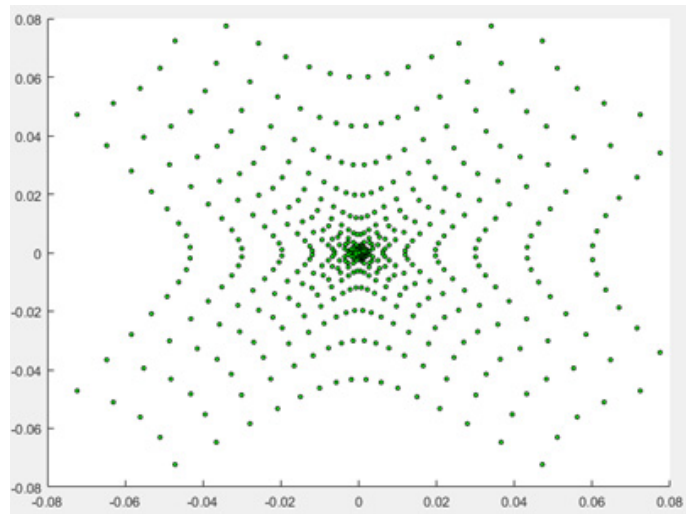


Figure 5.23: The Intersection Points of Overtreatment

5.4.2 Simulation of the Human Vision

With improved human eye models and ray tracing methods, training and test datasets can be obtained, including where the incident rays intersect on the retina. By neural networks and the datasets, the BDF is derived. The simulation of the human vision is rendered as the image. Figure 5.24 shows the scene without the defocus blur. Figure 5.25 shows the DoF effect for the thin lens; that is, it is a camera vision simulation.

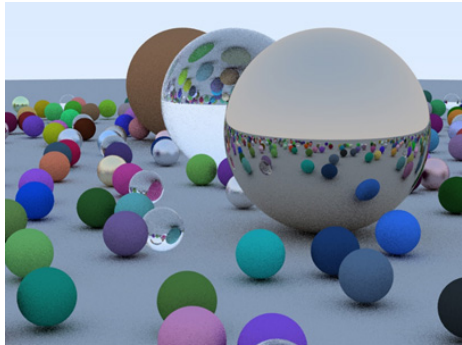


Figure 5.24: The Scene without Defocus Blur

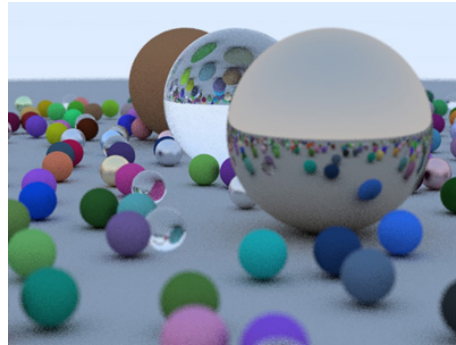


Figure 5.25: The Scene with DoF Effect for Thin Lens

As shown in Figure 5.26, it is the simulation of human vision using the improved human eye model. The front blur is lighter than the DoF effect of the camera vision. That is more accurate than that in Figure 25, and it is consistent with real human vision.

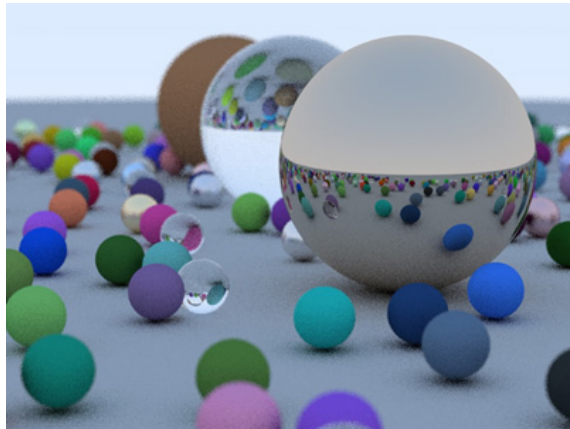


Figure 5.26: The Defocus Blur with Improved Human Eye Model

The myopia vision is simulated in Figure 5.27. The near objects are clear, and the distant objects are blurry. It accurately simulates the myopia vision. The post-surgery vision is simulated in Figure 5.28. There is an idea about LASIK because the surgery establishes the natural difference of the corneal stroma; the distant objects may be clearer than emmetropia. The simulation result in Figure 5.28 supports this idea.

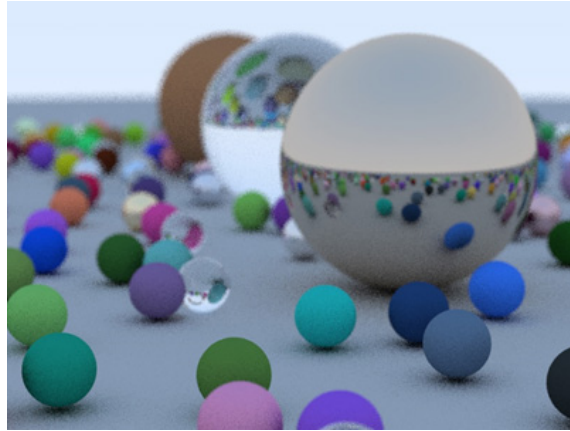


Figure 5.27: The Myopia Simulation

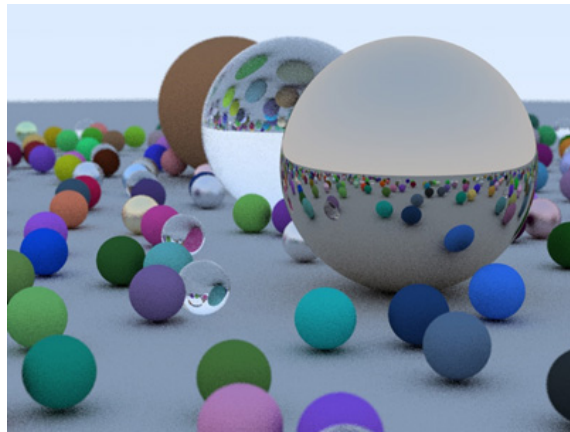


Figure 5.28: The Post-surgery Simulation

In order to compare the simulation results with real human vision, a special test based on subjective evaluation has been conducted as a reference for this study. As shown in Figure 5.29, the right eye is chosen for this test. The spherical power is -4.25D without

the cylindrical error. The optical properties of the test eye are shown in Table 5.3. The optical properties are measured by the ultrasonic tomography.

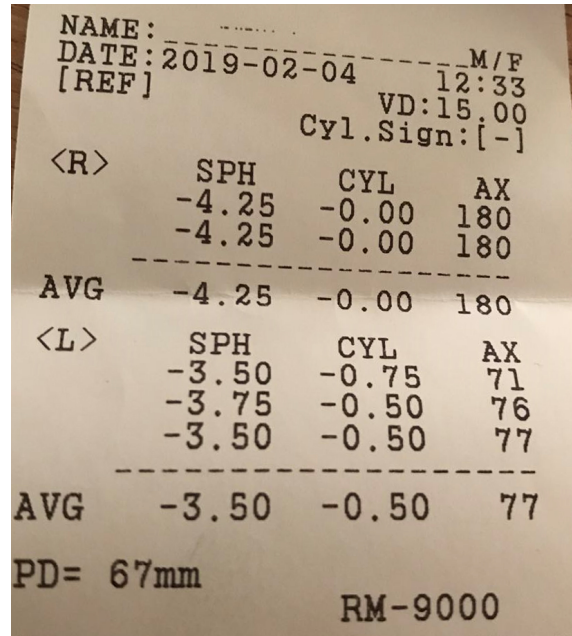


Figure 5.29: The Original Optometry data for the Subjective Evaluation

Table 5.3: The Optical Properties of the Test Eye

	Surface	Pos	Rad	Asph	Thick	Ref	Aper
Cornea	1	0.0	7.75	-0.24	0.54	1.367	12
	2	0.54	6.67	0	3.55	1.3374	12
Lens	3	4.09	10.42	-2.97	3.76	1.42	10
	4	7.58	-6	-1	17.25	1.336	10
Retina	5	25.1	-12	0	0	0	24

The vision simulation is shown in Figure 5.30. According to the discriminated by the tester, the subjective and the blur level of the vision simulation are similar to the real vision.

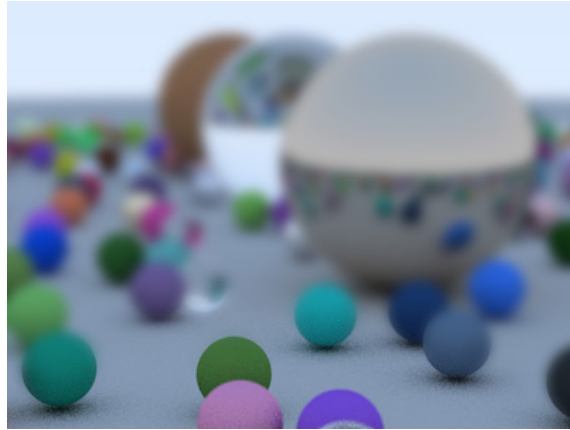


Figure 5.30: The Myopia simulation for the Subjective Evaluation

5.5 Summary

This chapter introduces the image-forming principle of the human eye and the principle of refractive surgery. Based on the principles, the improved human eye model is proposed. The model supports changes in the axial length and the corneal thickness for the pathological human eye and the refractive surgeries. In addition, in the human vision simulation, a novel BDF derivation method is proposed. This method is based on the machine learning. The training dataset is generated by the improved human eye model and ray tracing. The BDF is derived from the neural networks and the training dataset. The final rendering results have proven the efficiency of the model and the BDF derivation method. The GPU-accelerated ray tracing method is proposed in the following chapter. This method can reduce the computation cost of the ray tracing in the human vision simulation. It can speed up the rendering in the human vision simulation.

Chapter 6

GPU-Accelerated Ray Tracing Method

6.1 Overview

In the previous chapter, the improved human eye model and the BDF derivation method are proposed for the human vision simulation. Both of these works are based on ray tracing. Ray tracing can accurately compute the reflection and refraction of the rays. This method is suitable for human vision simulation. However, as mentioned in Chapter 1, compared with rasterisation, ray tracing needs more computation cost. For example, in order to render a Full-HD size (1920x1080) image for the human vision simulation, it needs about 15 minutes with a modern computer.

On the other hand, with rasterisation method, it needs less than 167ms. The reason is the rasterisation is optimised by GPU for years. The majority of the computing processes using in rasterisation have been accelerated by GPU. While NVIDIA presented the novel GPUs and APIs for the acceleration of ray tracing, there are only limited GPUs supported the new speciality. Meanwhile, the APIs, such as OptiX, have limited in the multiple lenses computing. As mentioned in Section 2.7, with the development of modern GPU architecture, a GPU-based parallel computing platform can provide an evident advantage in floating-point operations and memory bandwidth compared with CPU-based serial computation platform.

Meanwhile, the GPU can also provide the same general purpose computing ability as

the CPU platform. Therefore, in this chapter, the GPU-accelerated ray tracing method based on CUDA is proposed. This method can reduce the computation cost of the ray tracing in the human vision simulation. It can speed up the rendering in the human vision simulation.

For a better description and explanation of the work in this thesis, a summary of the principal and architectural structure of the CUDA platform will be given in Section 6.2. The framework of the GPU-accelerated ray tracing is proposed in Section 6.3. In Section 6.4, the performance analyses and optimisations are introduced.

6.2 Overview of CUDA Platform

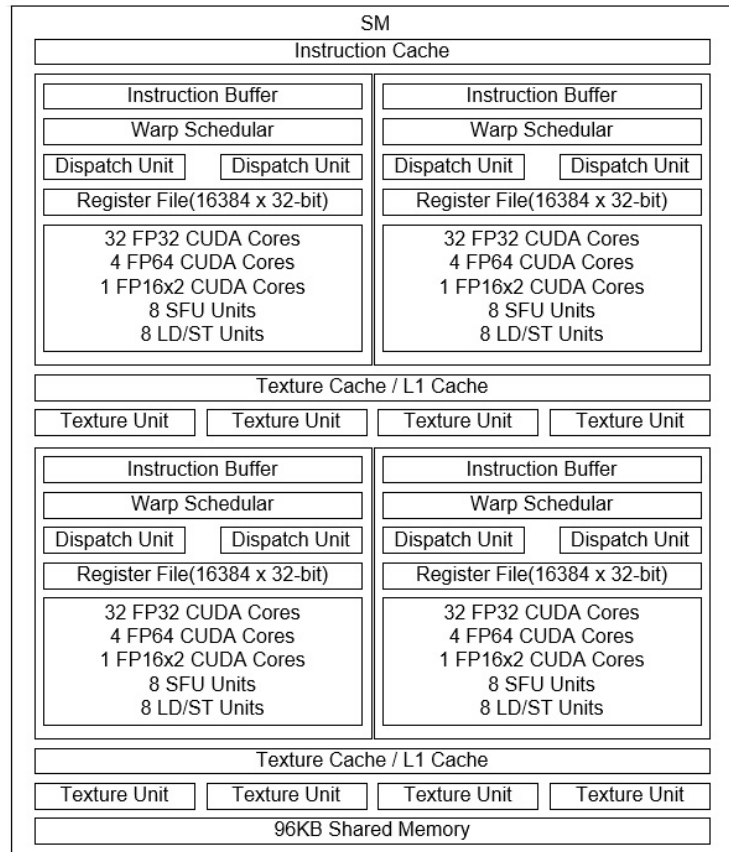


Figure 6.1: The SM Structure of the GPU Used by the Quadro P5000

As a GPU-based general-purpose computing platform, the basic computing unit of the CUDA platform is Streaming Multiprocessor (SM). There are hundreds of CUDA cores in each SM. Each CUDA core can perform integer and floating-point operations independently. To enhance the arithmetic performance, SM also includes the special function units (SFU) which provide the complete transcendental function instructions, e.g. trigonometric functions, reciprocal and square root. For the complex general-purpose computing, L1/L2 data cache, instruction buffer and scheduling units are added to the SM. The SM structure of the Quadro P5000 is illustrated in Figure 6.1. The SM includes instruction cache, four processors, texture/L1 cache, eight texture units and 96KB shared memory. Each processor includes 32 FP32 CUDA cores for single-precision floating-point operation, 4 FP64 CUDA cores for double-precision floating-point operation, 1 FP16 x 2 CUDA core for half-precision floating-point operation, 8 SFU units, register (16384 x 32-bit), two dispatch units, warp scheduler and instruction buffer. The compute capability is a concept that describes the GPU architecture. The compute capability of this GPU is 6.1.

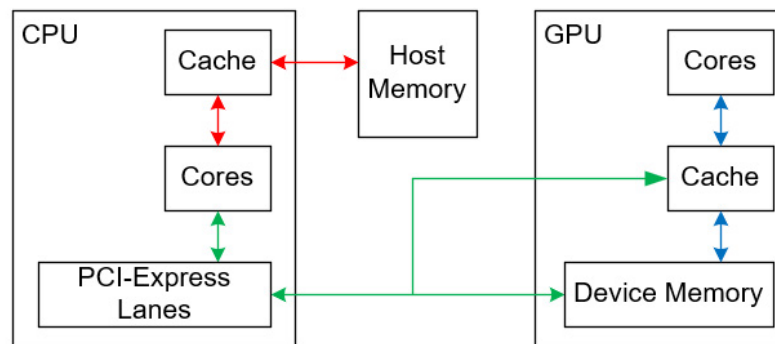


Figure 6.2: GPU Parallel Computing System

As shown in Figure 6.2, it is a schematic GPU parallel computing system based CUDA platform. The program consists of two main parts: The host program run on the CPU. Sub-program that run natively on the GPU is called Kernel Function. The red arrow lines present the host program processing on the CPU. The blue arrow lines present Kernel Function running on the GPU. CPU only operates Host memory.

Similarly, GPU only operates Device memory. The only transmission channel for the

data transfer between CPU and GPU is PCI-Express Lanes in CPU. The green arrow lines present the data transfer between CPU and GPU. Since the limited throughput of PCI-Express Lanes (15.75GBps with 16 Lanes PCI-Express Gen3), the data transfer rate through the PCI-Express Lanes is lower than the data transfer rate in the throughput between CPU (up to 130GBps with E5-2650 v4) and Host memory or between GPU and Device memory (up to 288GBps with NVIDIA Quadro P5000).

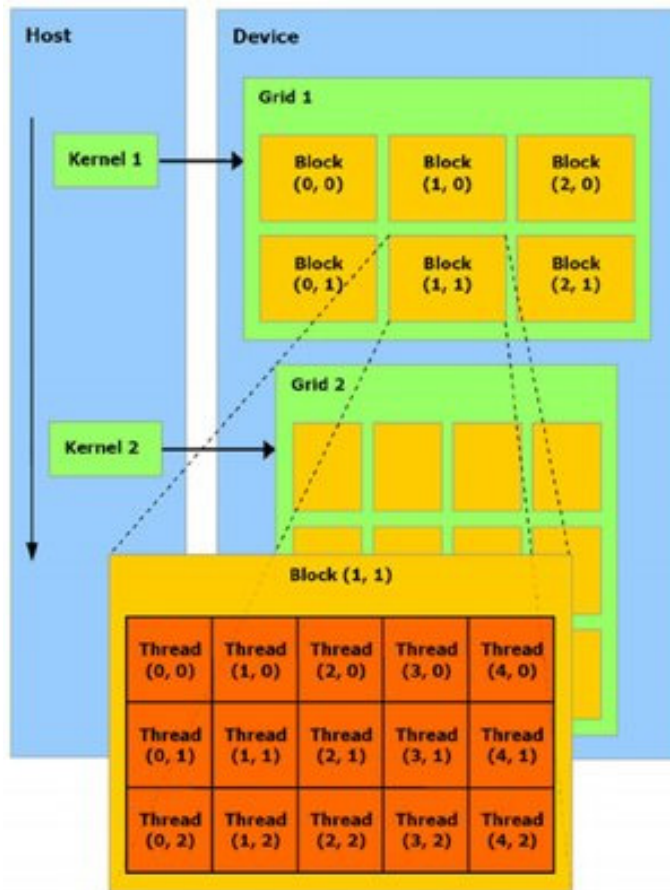


Figure 6.3: Schematization of Thread organization

In order to get the best efficiency of hardware, the logical structure of the Kernel Function is highly correlated with the hardware structure of GPU. As shown in Figure 6.3 [123], the design of Kernel Function should follow the Threads organization, including Grid, Block and Thread. The Grid is composed of Blocks. The Block is composed of

Threads. The dimension sizes of Thread, Block and Grid are defined by the GPU compute capability, e.g. NVIDIA Quadro P5000 with compute capability 6.1, the maximum number of threads per block is 1024, the maximum number of threads per SM is 2048, the maximum dimension size of a thread block is (1024, 1024, 64), the maximum dimension size of a grid is (2147483647, 65535, 65535).

Table 6.1: GPU Memory Hierarchy

Storage Type	Location	Cached	Access	Scope
Register	On-chip	N/A	R/W	Thread
Local	Off-chip	No	R/W	Thread
Shared	On-chip	N/A	R/W	Block
Constant	Off-chip	Yes	R	Grid
Global	Off-chip	Yes	R/W	Grid
Texture	Off-chip	Yes	R	Grid

When the Kernel Function is launched by the GPU, the Blocks in the Kernel Function are mapped to SM, and the Threads are mapped to the CUDA core. It could be found that the maximum number of Blocks and Threads is much larger than the number of SMs and CUDA cores, respectively. The cost of threads switching should be considered, although GPU thread switching is shorter than the Kernel Function launch and data transmission. The CUDA platform is considered as a single-instruction multiple data (SIMD) execution model. Threads execute the same instructions to process different data in Warp units. Warp occupancy is a measure of the utilization of cores in SM and is one of the issues to be considered for parallel program optimization.

On the other hand, as shown in Table 6.1, there are six types of memory defined in the CUDA platform. The register and shared memory are on-chip memory. The constant memory and texture memory are read-only and cached by the on-chip cache. In order to achieve the best Warp execution efficiency, the data should be aligned in the memory and stored in the fastest memory. Therefore, in the CUDA platform, memory optimization is another issue that should be considered.

6.3 The Method of GPU-Accelerated Ray Tracing

The basic principle of the ray-tracing could be explained in Figure 6.4. Assume that a human eye E is out of the screen, and a ray l_1 is emitted from a pixel on the connection

screen of E , if l_1 intersects with object M at point P , connects the line from point P to the light source. The line to light source L_2 is not blocked by any object. The colour value of point P projected by L_2 light source on object M is recorded. The line to a light source L_1 is blocked by other objects. L_1 does not affect on the colour of the P point or forms a shadow. The ray-traced reflection and refraction functions follow the law of refraction and reflection. These are not described in detail here.

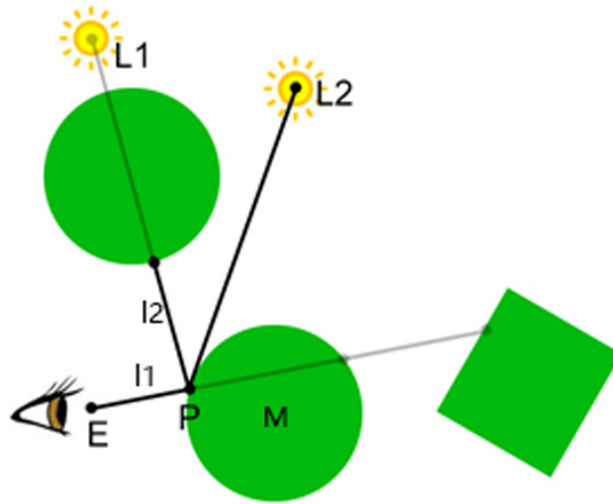


Figure 6.4: The Basic Principle of the Ray Tracing

In the simulation of human vision using the ray-tracing method, the ray is traced from the pixel position (retina) through the lenses group representing the lens, pupil, and cornea to the scene. According to the laws of reflection and refraction, the ray traversal operations among the objects are completed sequentially. The pixel colour is computed by the radiance along the ray path. The computation complexity increases as the resolution increases. And the computation complexity increases as the number of intersections of the ray path. If the ray-tracing computation is performed by the CPU, one computation cycles could process one pixel. If it is a Full-HD (1920 * 1080) resolution image, it needs 2073600 computation cycles. Figure 6.5 illustrates the CPU usage of the serial process. 86.45 % of the CPU time is used to complete the intersection computation and the intersection judgement, and about one half of the time is for the intersection judgement.

The GPU-based parallel computing is similar to multi-core CPU, with shared system bus and memory, but it integrates thousands of computing cores in one chip. If the

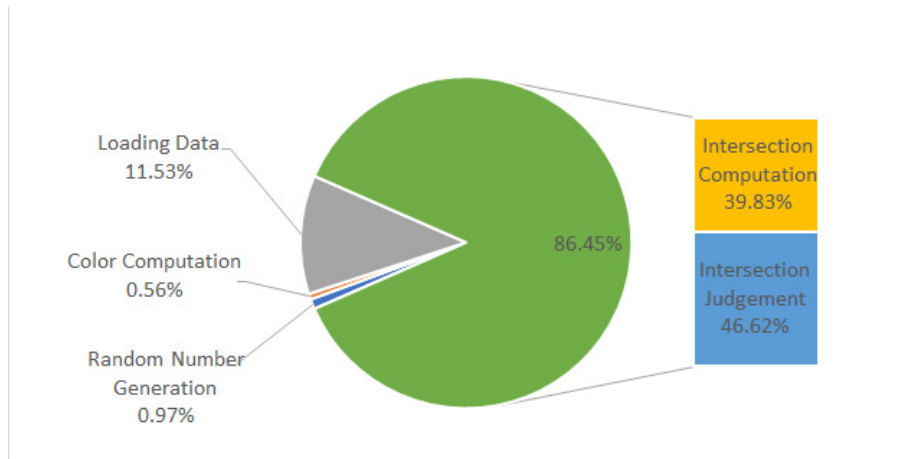


Figure 6.5: The CPU Usage of Serial Process

computation can be parallelised, that is, the computation of each ray path is assigned to one thread on the GPU. If there are not any differences among the threads, GPU-accelerated ray tracing method can achieve thousands of times speedup than on CPU. The GPU-accelerated ray tracing method without optimisation can only achieve about 40 times speedup than on CPU. The main reason for this is that the number of objects that the ray path corresponding from different pixels intersect in the scene is different, that is, the computation complexity of the threads is different, which causes low in GPU thread block utilisation and memory utilisation. Each pixel computation and its ray path computation are assigned to one thread on the GPU. The usages of the thread and the memory are optimised for better performance.

6.4 The Performance Analyses and Optimisations

The hardware specification for the performance analyses of the GPU-based parallel model is shown in Table 6.2. The CPU of the test platform is double E5-2650 v4 with 2.2GHz, 12 cores and 24 threads. The Host memory is 128 GB cached by 30MB L2 cache in CPU. In the test platform, double Quadro P5000 of NVIDIA with 2560 cores GP104 GPU is selected as the Devices for the algorithm performance testing. The 2560 cores are divided into 20 SMs which are included in 5 GPCs. Each SM has 256KB register, 48KB L1 cache (shared with texture cache) and 96KB shared memory. The GP104 memory is 16GB 256-bit GDDR5,

which is cached by 2048KB L2 cache. The memory bandwidth of GP104 is 192 GB/s. The compute capability of GP104 is 6.1. The peak floating-point performance with single precision of GP104 is 8.873 TFLOPS. The peak floating-point performance with double precision of GP104 is 277.3 GFLOPS. The pixel rate of GP104 is 110.9 GPixel/s.

Table 6.2: Performance Test Platform Specifications

Module	Module Specification
CPU	Intel Xeon E2650 v4 12 cores@2.2Ghz (1 core in use) with 30MB L3 cache
Operating system	Windows 10 for Workstation
GPU	Quadro P5000 with GP104
CUDA cores	2560 cores
GPU memory	16GB 256-bit GDDR5
GPU bandwidth	192 GB/s
GPU peak single precision floating-point performance	8.873 TFLOPS in theory
CPU compiler	Microsoft C/C++ optimizing compiler 19.00
GPU compiler	NVCC 9.0

6.4.1 Analysis of computing speedup

In order to accurately and fully test the speedup of this parallel computing model, there are 20 different amount of objects in the scene chosen to take part in the test. The objects are randomly placed into the scene. There are three materials for the objects, metal, glass and diffuse. The materials are randomly assigned to the objects. And the amount of objects is a multiple of 2 from 1 to 524228. For the accurate evaluation of the speedup, the codes compiled for the serial and parallel algorithm are optimized with Maximize Speed (/O2). On both CPU and CUDA platform, each scene with a fixed virtual viewpoint at (13, 2, 3). The original point is (0, 0, 0). Each scene is run ten times, and an average of these tests is chosen to be the test result of each dataset. The amount of Threads of each Block, the size of Block, is 512. The size of the Grid is the ratio of the number of objects to Threads, and the minimum value is 1. There is only 1 Grid in the computing process. The dimensions of Block and Grid are 3. The other rendering parameters are shown in Table 6.3.

The objective of parallel computing is to provide faster computation. Thus, certain defined parameters are needed to measure the performance of the parallel computing algo-

Table 6.3: The Rendering Parameters for Test

Module	Module Specification
Resolution	1000 pixels by 1000 pixels
Color Depth	Red 8 bits, Green 8 bits and Blue 8 bits
Number of Scene	20 Scenes
Number of Objects in Scene	Multiple of 2 from 1 to 524228
Objects' Material	Metal, Glass and Diffuse

rithm versus the serial computing algorithm. Amdahl [124] proposes two common measures of effectiveness that account for both the hardware and the algorithm design are speedup and efficiency. Speedup, S_p is defined as the ratio between the time of executing a serial algorithm for a set of computations, T_s , and the time to perform these same computations with a parallel algorithm, T_p .

$$S_p = \frac{T_s}{T_p} \quad (6.1)$$

The other measure, efficiency, E_p , is defined as the ratio of speedup to the number of processors. Efficiency accounts for the relative cost in terms of the number of the processors required in achieving a certain speedup.

$$E_p = \frac{S_p}{p} \quad (6.2)$$

The two formulas are used to measure the parallel algorithm performance in the following analyses.

For a better representation, in Figure 6.6, the value of Y-axis is the logarithm of the computing time of CPU-based and GPU-based, respectively. When the number of objects is below 256, the GPU-based parallel computing time is slower than the CPU-based serial computing time. In contract, while the number of objects is more than 256, the speed of the GPU-based parallel computing is significantly faster than that of the CPU. The advantage of GPU-based parallel computing increases as the number of objects increases.

The phenomenon can be explained with the principles of the CUDA platform. If the number of objects below 256, the computing of CPU is not affected, however, the time cost of Kernel Function launch, Wrap switch and GPU memory access on the CUDA

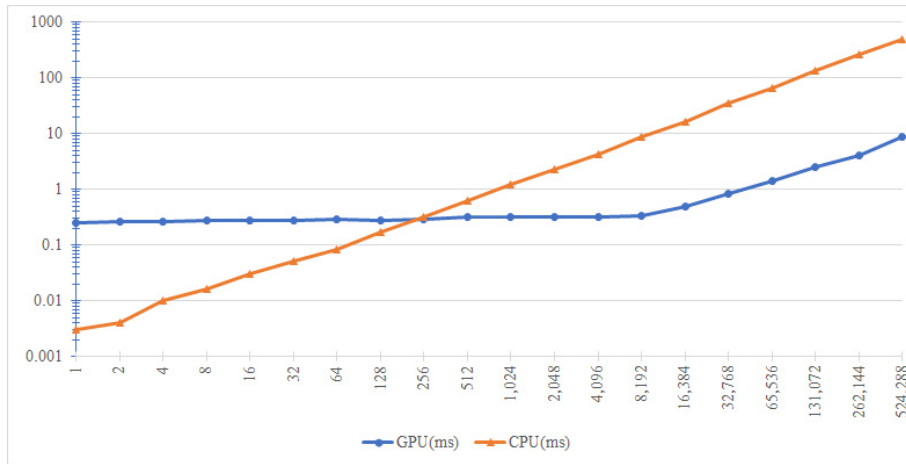


Figure 6.6: One Pixel Computing Time between CPU-based Serial Computing and GPU-based Parallel Computing

platform offsets the benefits of CUDA parallel computing. With the increasing of objects, the advantages of computational parallelism become obviously.

In Figure 6.7, the total rendering time cost comparison between CPU-based serial computing and GPU-based parallel computing is illustrated for evaluating the performance of human vision simulation. When the number of objects reaches 2048, the performance of CPU-based serial computing is lower than GPU-based parallel computing. The time cost is 39.37s. Meanwhile, until 524288 objects in the scene, the performance of GPU-based parallel computing is still acceptable, the total rendering time is only 112.36s. On the other hand, the performance of CPU-based serial computing reaches 5000s.

The trend of speedup of the CUDA platform is shown in Figure 6.8. With more than 16384 objects, the CUDA platform provides a significant speedup compared that on the CPU. The maximum speedup of the CUDA platform is 44.50. This trend can also be observed in the efficiency of GPU-based parallel computing shown in Figure 6.9. The maximum efficiency of the CUDA platform is 0.02.

According to the above results and analysis, GPU-based parallel computing has greatly surpassed CPU-based computing. As mentioned in the previous section, the potential of the GPU-based parallel should be inspired by the optimisation. In order to enhance the computing performance on the CUDA platform, several methods mentioned in the previous section are taken, including a reasonable allocation of the size of Threads, Blocks and Grids

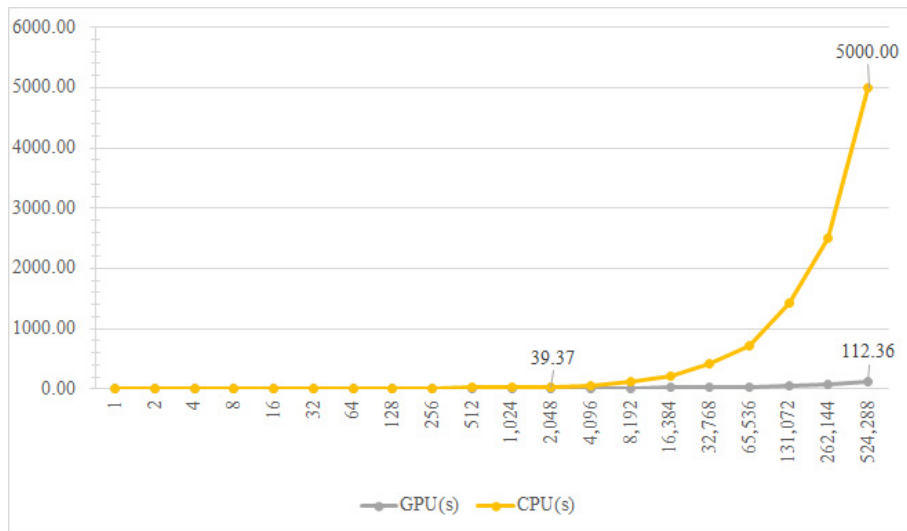


Figure 6.7: The Total Time Cost Comparison between CPU-based Serial Computing and GPU-based Parallel Computing

for a specific scene and the adoption of the register, shared memory and constant memory. These optimisations above are discussed in the following parts.

6.4.2 Threads Optimisation

For an accurate evaluation of optimisation, the impact of the Block size on the computing performance of the objects simulation is evaluated by varying the block size while keeping the registers per thread at 64. Meanwhile, the number of objects is 524288. Figure 6.10 shows the speedup of the different block size with 524288 objects. In order to obtain this plot, 32 executions of the parallel programs are executed in a row for each given block size. From this study, it is found that the block size of 544 produces the best performance, 58.51 times speedup, with 524288 objects.

As shown in Figure 6.11, with 554 Threads in each Block, the amount of register used by Threads is 34,816. However, the maximum number of registers per each Block is 65,536 for the Quadro P5000. In order to find the best performing combination of the Block size and register count per Thread, the parallel program is tested with the different combination of Block size and the number of registers per Thread. One hundred ninety-two combinations of the Block size and number of registers per Thread are executed. The register at 70 per

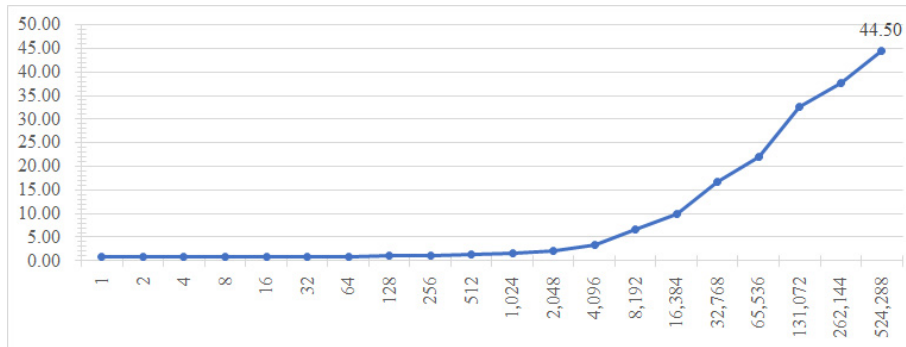


Figure 6.8: The Speedup of GPU-based Parallel Computing Compared with the CPU-based Serial Computing

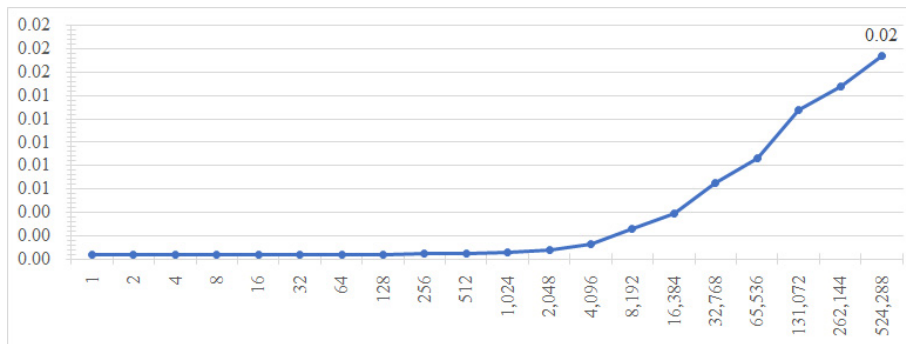


Figure 6.9: The Efficient of GPU-based Parallel Computing Compared with the GPU-based Serial Computing

Thread is chosen by the CUDA compiler with unlimited max registers compiler option, `-maxrregcount=0`. Since the total number of registers in combination with the register at 70 and Block size greater than 896 exceeds the maximum register limit allowed for each Block, the Kernel Function cannot be launched, so these tests have no results.

The results are displayed in Figure 6.12 for the different combination of Block size and the number of registers per Thread. It shows that the optimal computing performance occurs at 70 registers with 480 thread for 524288 objects, 65.94 times speedup, and the speedups seem to keep dropping beyond this number of registers and Threads.

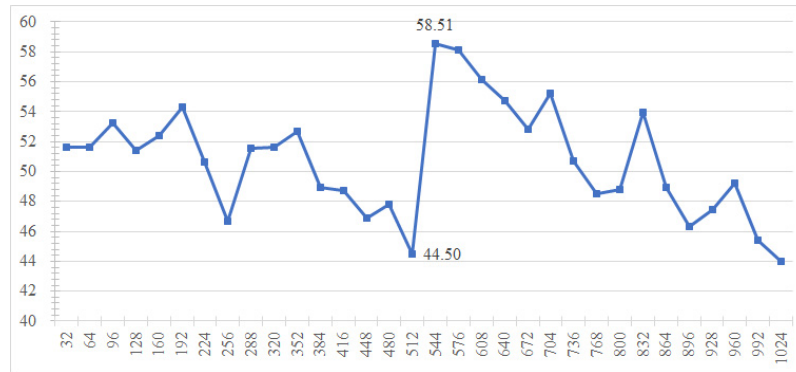


Figure 6.10: The Speedup with the Different Block Size

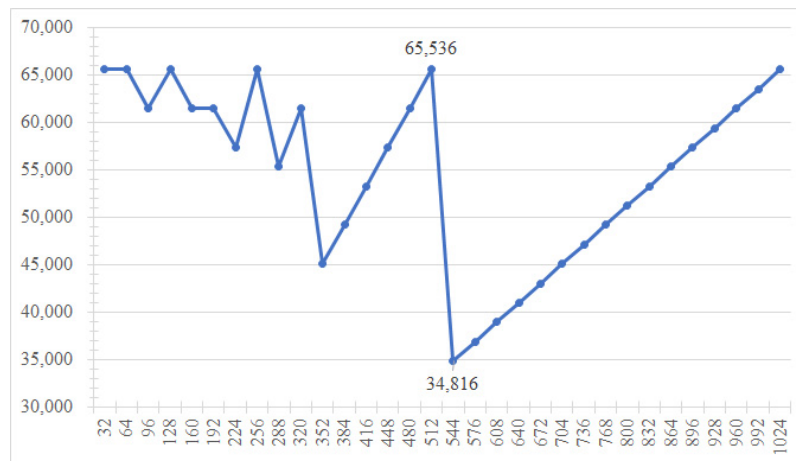


Figure 6.11: The Number of Registers of the Different Block Size

6.4.3 Device Memory Optimisation

The fastest memory is the registers. However, the register is non-programming; that is, the using of the register cannot be controlled by the developer directly, which has mentioned in the previous section. As shown in Table 6.4, the speed of memory access is different among the different Device memories. According to the bandwidth and latency comparison, the shared memory is faster than global memory; however, on-chip design of shared memory makes the size is much smaller than the global memory. Therefore, shared memory is often used for limited variables that need to load and store among Threads in the same Block quickly.

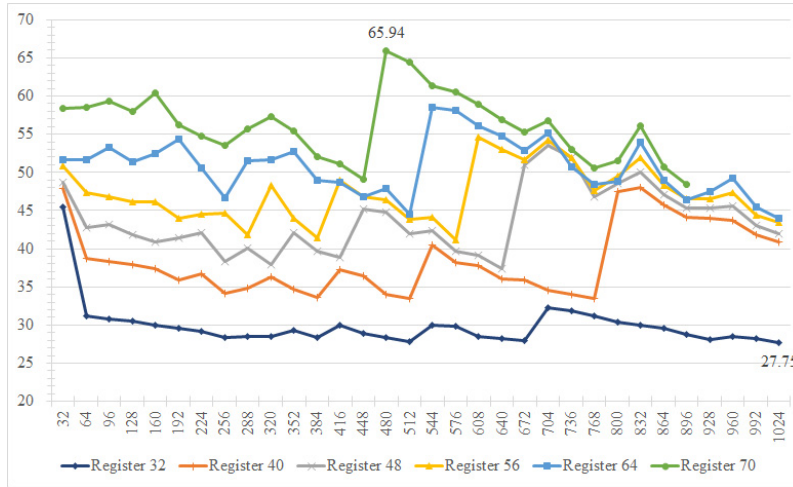


Figure 6.12: The Comparison among the Different Combination of Block Size and Number of Registers per Thread

Table 6.4: The Comparison among the GPU Memories

Storage Type	Bandwidth	Latency
Shared Memory	3,919GB/s	1 to 32 clocks
Constant Memory	288GB/s	400 to 800 clocks
Global Memory	288GB/s	400 to 800 clocks
Texture Memory	288GB/s	400 to 800 clocks

As mentioned in the previous section, the majority of computation time is for the intersection computation and intersection judgement. In this process, 22 single-precision floating-point variables need to load and store frequently. For reducing the latency of the memory access, in this study, the 22 variables are move to the shared memory from the global memory. The usage of the shared memory is calculated as below:

$$F_s = C_t \cdot S_v \cdot C_v \quad (6.3)$$

The usage of the shared memory, F_s is defined as the product of the number of Threads, C_t , the memory usage of variable, S_v , and the number of variables, C_v . According to Formula 6.3, 22 single-precision floating-point variables of 480 Threads per Block optimized

by previous work require 42240 bytes of the shared memory, which is less than the maximum shared memory limit of 49152 bytes per Block. By transferring these variables from global memory to shared memory, it reduces the memory access time of variables, thereby improves the performance of the program. As shown in Table 6.5, the speedup with shared memory is up to 75.18 times than serial programs on CPU.

Table 6.5: The Speedup of Memory Optimisation

	Runtime(ms)	Speedup
With shared memory optimization	2.40138	75.18 times
Without shared memory optimization	2.73779	65.94 times

6.5 Summary

In this chapter, an efficient GPU-accelerated ray-tracing method for human vision simulation is proposed. From the performance analyses with the Quadro P5000, the Block size and Device memory allocation are the main limiting factors for computing performance of simulation on the CUDA platform. This limitation holds for the other parallel computing model with domain decomposition strategy as well. In order to solve the problems, some optimizations are made to improve computing performance. With Threads optimization, the speedup of GPU-based parallel computing increases from 44.50 times to 58.51 times.

Moreover, with register allocation optimization, the speedup increases to 65.94 times. And then, after the memory access optimization, the frequently loaded and stored variables are move to the shared memory, which is with lower latency and greater bandwidth than the original global memory. This optimization makes the speedup increased to 75.18 times. In the following chapter, it is the final summary of the thesis.

Chapter 7

Conclusion

7.1 Overview

The chapter summarises the proposed methods and model for the intelligent assistant tool of the laser refractive surgeries with predictive and visualised functions in this thesis, especially the application to surgery prediction and human vision simulation. In this chapter, the main findings of the study and the contributions are presented with respect to the research question and subsidiary questions mentioned at the very beginning of this thesis. Some possible directions of the further work are provided at the end of this chapter.

There are four sections in this chapter. Section 7.2 summarised the proposed methods and model in this thesis. The main findings and contributions are presented in Section 7.3 and Section 7.4, respectively. In Section 7.5, future work is proposed.

7.2 Summary

This study comprehensively has reviewed the technical development level of refractive surgery and explored the computational analysis and modelling techniques about refractive surgery. In particular, it summarises the current research status of prediction and planning of laser refractive surgery. This study aims to develop intelligent assistant tools for laser refractive surgery with prediction and visualisation functions. In order to achieve this aim, this study has two objectives: using clinical datasets to predict surgical parameters and outcomes, and simulating the human vision. In order to complete the above

two objectives, this study proposes several methods and model, including multiple data imputation methods, imbalanced dataset resampling method, genetic algorithm-optimised ensemble learning method, the improved human eye model, machine learning-based BDF derivation methods, and GPU accelerated ray-tracing method and optimisation. Based on these, this research has completed an intelligent assistant tool for laser refractive surgery with prediction and visualisation functions, as shown in Figure 7.1. This software has obtained the certification of software copyright.

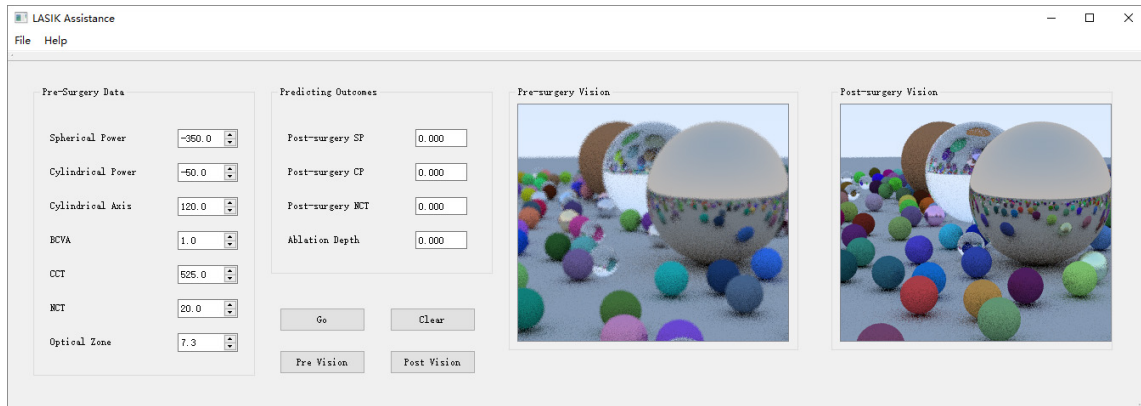


Figure 7.1: The Intelligent Assistant Tool of the Laser Refractive Surgery

Among these methods and model, multiple data interpolation method is used to complete data pre-processing. Based on the correlation analysis of each property in the dataset, a multiple regression model is established for the properties with missing data, and the missing data can be obtained by this multiple regression model. The method can predict possible missing data, and the biased direction of the model could be calculated.

After completing the data imputation, according to the distribution of medical dataset, this study proposes a resampling method for imbalanced datasets. This method focuses on over-sampling the mixed area between the majority data and minority data. The relatively conservative thresholds are used to control the generation of over-sampling data. This method is used to avoid model deviation.

After completing the data resampling, for the data sparseness problem in the medical field, this study proposes an ensemble learning method optimized by genetic algorithms. This method uses genetic algorithms to optimize the basis predictor of ensemble learning, to improve the prediction accuracy of the basic predictor, and then to improve the prediction

accuracy of the final model of ensemble learning.

For human eyeball modelling, this study focuses on the modelling of abnormal eyeball and surgical eyeball. Based on the analysis of the causes of myopia and hyperopia and the principle of refractive surgery. This study adds the changes of the axial length and the corneal thickness into the existing Navarro eye model and proposes an improved human eye model. This model is suitable for the normal eyeball, abnormal eyeball and refractive surgery eyeball.

In the human visual simulation, this study focuses on the derivation of the defocus blur range function for pathological and post-operative vision simulation. Based on the previous improved eye model, this study uses ray tracing method to generate training datasets. And then, the blur distribution function (BDF) is derived by the neural networks and the training datasets. With BDF, it could accurately simulate the human vision. In addition, in order to improve the generation speed of the training datasets and the rendering speed of the simulation results, this study proposes a GPU-accelerated ray tracing method and its optimization method, which can achieve 75 times acceleration.

The different methods and model presented in this thesis are tested and verified. The positive results are obtained, and these are discussed further in the next section.

7.3 Main Findings

This section presents the main findings from the conducted research presented in this thesis. Referring back to Chapter 1, the initial research question is:

Is it possible to design machine learning-based methods suitable for multi-input, multi-output and non-linear system modelling so that effective data prediction and simulation can be achieved in the presence of missing data, imbalanced data, sparse data and complex datasets?

The solution to this research question requires that several subsidiary issues be addressed. And Each of them is discussed below.

1. *The issue of missing data*

In a real system, due to the problems of statistics, the missing of input and output data is unavoidable. During the process of modelling using a machine learning approach, the deviation of the mathematical model is largely due to the missing data. In chapter 3, the multiple imputation method based on the multiple regression is proposed. With the

test in Section 3.5, this method is accurate and effective.

2. The issue of imbalanced dataset

In a real system, the amount of data outputted by one type of output is much less than (or more than) the amount of data outputted by other types. The dataset imbalance may make the model deviate while using the machine learning approach to establish the mathematical model of the simulation system. To solve this issue, in Chapter 4, an imbalanced dataset resampling method is proposed. By the testing in Section 4.3.4, the method proved to be accurate and effective.

3. The issue of sparse data distribution

Due to data statistics or real system characteristics, the data distribution is not concentrated, so that an effective model cannot be trained. For this issue, the genetic algorithm optimised ensemble learning method is proposed in Chapter 4. A comparison between the single machine learning method, and this method shows that this method is more effective and accurate.

4. The ray tracing method uses blur to describe the loss of details.

The computing of the blur range and quantity are determined by the blur distribution function (BDF). Currently, the BDF is determined for normal human vision and is not suitable for pathological human vision. The pre-condition of this solution is an improved human eye model which supports normal eye, abnormal eye and refractive surgery eye. This model is proposed in Section 5.3. The BDF derivation method is also proposed in Section 5.3. Both model and method are tested and verified in Section 5.4.

5. The computing of ray intersection, ray reflection and ray refraction take significant time.

For the existing algorithm and hardware technology, it is impossible to guarantee high-speed and high-fidelity scene rendering. There is also a requirement for a novel accelerate approach for ray tracing computing. For this issue, chapter 6 provides a detail description of the GPU-accelerated ray tracing method and optimisation. This method provides 75 times speedup.

Returning to the research question posed at the very beginning of this thesis, the above methods and model proposed in this thesis could combine an intellectual toolkit for the solve this research question. In addition, these methods and model also extend the application scope of the machine learning from data field to the simulation field. It also the main finding in this study.

7.4 Research Contributions

The findings from this study make several contributions to the body of knowledge. These contributions can be summarised as follows:

1. A novel and effective method to plan, predict and evaluate the refractive surgeries with a medical dataset.

According to the distribution of the sample in clinical data, the percentage of the unacceptable results is 23.02%. The method in this study could provide 79.02% accuracy to find the possible unacceptable cases, that is, the method could reduce the percentage of unacceptable results from 23.02% to 4.82%.

2. A multiple imputation method is proposed for the missing medical data in the training and test datasets.

3. An improved over-sampling method is designed for reducing FPF and FNF with the imbalanced medical data.

4. An ensemble learning method with optimisation is proposed for increasing the accuracy of the predictor in a sparse medical dataset.

5. An improved schematic human eye model with variable axial length and corneal thickness is proposed for pathological human vision, e.g. myopia and hyperopia, and refractive surgery.

6. A novel data augmentation method is proposed for machine learning using the results of human vision simulation.

7. A BDF derivation method is proposed for using machine learning.

8. A GPU-accelerated ray tracing rendering engine is designed for the human vision simulation.

In addition to the contribution mentioned above, this work has also made some contributions to other fields.

1. A medical dataset with detailed explanations of each property was developed and can be published for the further machine learning research.

2. A universal optimisation workflow is designed for other GPU-accelerated applications.

With this proved workflow, the speedup of GPU acceleration from 44.50 times to 75.18 times, increase about 68.94

7.5 Future Work

Several possible directions for the future work as introduced as below:

1. The clinical data will be collected for further research continually.
2. Both the over-sampling method and the under-sampling method will be combined for a novel data resample method.
3. The aberration of the human eye will be considered in the visual simulation.
4. As one of the future works, machine learning will be applied in other virtual environments.

This paper only planted seeds for the above research direction. Perhaps one of these directions can change the world in the near future.

Bibliography

- [1] Dimitri T Azar. *Refractive Surgery E-Book*. Elsevier Health Sciences, 2019.
- [2] FangJun Bao, Si Cao, JunJie Wang, Yuan Wang, Wei Huang, Rong Zhu, XiaoBo Zheng, JinHai Huang, ShiHao Chen, and YiYu Li. Regional changes in corneal shape over a 6-month follow-up after femtosecond-assisted lasik. *Journal of Cataract & Refractive Surgery*, 45(6):766–777, 2019.
- [3] FangJun Bao, JunJie Wang, Si Cao, Na Liao, Bao Shu, YiPing Zhao, YiYu Li, XiaoBo Zheng, JinHai Huang, and ShiHao Chen. Development and clinical verification of numerical simulation for laser in situ keratomileusis. *Journal of the mechanical behavior of biomedical materials*, 83:126–134, 2018.
- [4] Xu Chen, Fei Yuan, and Lianqun Wu. Meta analysis of intraocular lens power calculation after laser refractive surgery in myopic eyes. *Journal of Cataract & Refractive Surgery*, 42(1):163–170, 2016.
- [5] Joaquin Fernandez, Manuel Rodriguez-Vallejo, Javier Martinez, Ana Tauste, and David P Piero. Corneal biomechanics after laser refractive surgery: Unmasking differences between techniques. *Journal of Cataract & Refractive Surgery*, 44(3):390–398, 2018.
- [6] Himel Kandel, Jyoti Khadka, Mats Lundstrm, Michael Goggin, and Konrad Pseudovs. Questionnaires for measuring refractive surgery outcomes. *Journal of Refractive Surgery*, 33(6):416–424, 2017.
- [7] George D Kymionis, Vardhaman P Kankariya, Argyro D Plaka, and Dan Z Reinstein. Femtosecond laser technology in corneal refractive surgery: a review. *Journal of Refractive Surgery*, 28(12):912–920, 2012.

-
- [8] Ane Murueta-Goyena and Pilar Canadas. Visual outcomes and management after corneal refractive surgery: A review. *Journal of optometry*, 11(2):121–129, 2018.
- [9] Daizong Wen, Colm McAlinden, Ian Flitcroft, Ruixue Tu, Qinmei Wang, Jorge Ali, John Marshall, Yingying Huang, Benhao Song, and Liang Hu. Postoperative efficacy, predictability, safety, and visual quality of laser corneal refractive surgery: a network meta-analysis. *American journal of ophthalmology*, 178:65–78, 2017.
- [10] Gustavo K Marino, Marcony R Santhiago, and Steven E Wilson. Femtosecond lasers and corneal surgical procedures. *The Asia-Pacific Journal of Ophthalmology*, 6(5):456–464, 2017.
- [11] Anne Huhtala, Juhani Pietilä, Petri Mäkinen, and Hannu Uusitalo. Femtosecond lasers for laser in situ keratomileusis: a systematic review and meta-analysis. *Clinical Ophthalmology (Auckland, NZ)*, 10:393, 2016.
- [12] Liang Hu, Yiqing Huang, and Meng Lin. Excimer laser and femtosecond laser in ophthalmology. *High Energy and Short Pulse Lasers*, 2016.
- [13] Anders Ivarsen, Sven Asp, and Jesper Hjortdal. Safety and complications of more than 1500 small-incision lenticule extraction procedures. *Ophthalmology*, 121(4):822–828, 2014.
- [14] Kazutaka Kamiya, Kimiya Shimizu, Akihito Igarashi, and Hidenaga Kobashi. Visual and refractive outcomes of femtosecond lenticule extraction and small-incision lenticule extraction for myopia. *American journal of ophthalmology*, 157(1):128–134, 2014.
- [15] Bing Qin, Meiyang Li, Xun Chen, Walter Sekundo, and Xingtao Zhou. Early visual outcomes and optical quality after femtosecond laser small-incision lenticule extraction for myopia and myopic astigmatism correction of over- 10 dioptres. *Acta ophthalmologica*, 96(3):e341–e346, 2018.
- [16] Ting Liu, Guanting Lu, Kaijian Chen, Qiuxia Kan, and Ji Bai. Visual and optical quality outcomes of smile and fs-lasik for myopia in the very early phase after surgery. *BMC ophthalmology*, 19(1):88, 2019.
- [17] Rupal Shah. History and results; indications and contraindications of smile compared with lasik. *Asia-Pacific journal of ophthalmology (Philadelphia, Pa.)*, 8(5):371, 2019.

-
- [18] Joris Kenanian, Ayca Balkan, Raphael M Jungers, and Paulo Tabuada. Data driven stability analysis of black-box switched linear systems. *Automatica*, 109:108533, 2019.
- [19] Riccardo Guidotti, Anna Monreale, Salvatore Ruggieri, Franco Turini, Fosca Giannotti, and Dino Pedreschi. A survey of methods for explaining black box models. *ACM computing surveys (CSUR)*, 51(5):93, 2019.
- [20] D Rex Hamilton, R Duncan Johnson, Nancy Lee, and Nirit Bourla. Differences in the corneal biomechanical effects of surface ablation compared with laser in situ keratomileusis using a microkeratome or femtosecond laser. *Journal of Cataract & Refractive Surgery*, 34(12):2049–2056, 2008.
- [21] Boonchai Wangsupadilok and Orasa Horatanaruang. The impact of central corneal thickness on intraocular pressure measured by non-contact tonometry. *Journal of the Medical Association of Thailand*, 94(5):574, 2011.
- [22] George Fatseas, Fiona Stapleton, and Patrick Versace. Role of percent peripheral tissue ablated on refractive outcomes following hyperopic lasik. *PloS one*, 12(2):e0170559, 2017.
- [23] Sidath E Liyanage and Bruce D Allan. Multiple regression analysis in myopic wave-front laser in situ keratomileusis nomogram development. *Journal of Cataract & Refractive Surgery*, 38(7):1232–1239, 2012.
- [24] Carl-Arnold Lackerbauer, Martin Grüterich, Michael Ulbig, Anselm Kampik, and Corina Kojetinsky. Correlation between estimated and measured corneal ablation and refractive outcomes in laser in situ keratomileusis for myopia. *Journal of Cataract & Refractive Surgery*, 35(8):1343–1347, 2009.
- [25] Jorge L Alio, Felipe A Soria, Alessandro Abbouda, and Pablo Peña-García. Fifteen years follow-up of photorefractive keratectomy up to 10 d of myopia: outcomes and analysis of the refractive regression. *British Journal of Ophthalmology*, 100(5):626–632, 2016.
- [26] James V Jester, Theodore Venet, John Lee, David J Schanzlin, and Ronald E Smith. A statistical analysis of radial keratotomy in human cadaver eyes. *American journal of ophthalmology*, 92(2):172–177, 1981.

- [27] James Salz, John S Lee, James V Jester, Douglas Steel, Richard A Villasenor, Anthony B Nesburn, and Ronald E Smith. Radial keratotomy in fresh human cadaver eyes. *Ophthalmology*, 88(8):742–746, 1981.
- [28] MICHAEL G Block and MARC B Block. Use of multiple regression techniques in determining the surface of the cornea. *American journal of optometry and physiological optics*, 61(12):721–728, 1984.
- [29] Fang Jun Bao, A Yong Yu, Wael Kassem, Qin Mei Wang, and Ahmed Elsheikh. Biometry of the cornea in myopic chinese patients. *Journal of Refractive Surgery*, 27(5):345–355, 2011.
- [30] Richard A Villaseñor, Vicki Rice Santos, Kerry C Cox, Delaware F Harris II, Michael Lynn, and George O Waring III. Comparison of ultrasonic corneal thickness measurements before and during surgery in the prospective evaluation of radial keratotomy (perk) study. *Ophthalmology*, 93(3):327–330, 1986.
- [31] Niels Ehlers and Jesper Ø Hjortdal. Excimer laser refractive keratectomy for high myopia 6-month follow-up of patients treated bilaterally. *Acta ophthalmologica*, 70(5):578–586, 1992.
- [32] Srinivas Dutt, Roger F Steinert, Michael B Raizman, and Carmen A Puliafito. One-year results of excimer laser photorefractive keratectomy for low to moderate myopia. *Archives of Ophthalmology*, 112(11):1427–1436, 1994.
- [33] M Kohlhaas, R-Ch Lerche, J Draeger, M Klemm, N Ehlers, J Hjortdal, H Olsen, C Barraquer, JI Barraquer, D Flicker, et al. The influence of corneal thickness and corneal curvature on tonometry readings after corneal refractive surgery. *European journal of Implant and Refractive Surgery*, 7(2):84–88, 1995.
- [34] Yuan-Chieh Lee, Fung-Rong Hu, and I-Jong Wang. Quality of vision after laser in situ keratomileusis: influence of dioptric correction and pupil size on visual function. *Journal of Cataract & Refractive Surgery*, 29(4):769–777, 2003.
- [35] Andreas Helgesen, Jesper Hjortdal, and Niels Ehlers. Pupil size and night vision disturbances after lasik for myopia. *Acta Ophthalmologica Scandinavica*, 82(4):454–460, 2004.

- [36] Won-Mo Yi and Choun-Ki Joo. Corneal flap thickness in laser in situ keratomileusis using an scmd manual microkeratome. *Journal of Cataract & Refractive Surgery*, 25(8):1087–1092, 1999.
- [37] Sabong Srivannaboon, Dan Z Reinstein, Hugo FS Sutton, and Simon P Holland. Accuracy of orbscan total optical power maps in detecting refractive change after myopic laser in situ keratomileusis. *Journal of Cataract & Refractive Surgery*, 25(12):1596–1599, 1999.
- [38] Jens Bühren, Konrad Pesudovs, Tim Martin, Anja Strenger, Geunyoung Yoon, and Thomas Kohlen. Comparison of optical quality metrics to predict subjective quality of vision after laser in situ keratomileusis. *Journal of Cataract & Refractive Surgery*, 35(5):846–855, 2009.
- [39] Carl-Arnold Lackerbauer, Martin Grüterich, Michael Ulbig, Anselm Kampik, and Corina Kojetinsky. Correlation between estimated and measured corneal ablation and refractive outcomes in laser in situ keratomileusis for myopia. *Journal of Cataract & Refractive Surgery*, 35(8):1343–1347, 2009.
- [40] Jorge L Alio, Felipe A Soria, Alessandro Abbouda, and Pablo Peña-García. Fifteen years follow-up of photorefractive keratectomy up to 10 d of myopia: outcomes and analysis of the refractive regression. *British Journal of Ophthalmology*, 100(5):626–632, 2016.
- [41] Juan J Perez-Santonja, Juan Bellot, Pascual Claramonte, Mahmoud M Ismail, and Jorge L Alio. Laser in situ keratomileusis to correct high myopia. *Journal of Cataract & Refractive Surgery*, 23(3):372–385, 1997.
- [42] David Huang, R Doyle Stulting, Jonathan D Carr, Keith P Thompson, George O Waring, et al. Multiple regression and vector analyses of laser in situ keratomileusis for myopia and astigmatism. *Journal of Refractive Surgery*, 15(5):538–549, 1999.
- [43] Ömer F Recep, Nurullah Çağıl, and Hikmet Hasripi. Correlation between intraocular pressure and corneal stromal thickness after laser in situ keratomileusis. *Journal of Cataract & Refractive Surgery*, 26(10):1480–1483, 2000.
- [44] Vikram D Durairaj, Jennifer Balentine, Gregory Kouyoumdjian, Janet A Tooze, David Young, Lawrence Spivack, and Michael J Taravella. The predictability of

- corneal flap thickness and tissue laser ablation in laser in situ keratomileusis. *Ophthalmology*, 107(12):2140–2143, 2000.
- [45] Russell N Van Gelder, Karen Steger-May, and Jay S Pepose. Correlation of visual and refractive outcomes between eyes after same-session bilateral laser in situ keratomileusis surgery. *American journal of ophthalmology*, 135(5):577–583, 2003.
- [46] H Eleftheriadis, B Prandi, A Diaz-Rato, M Morcillo, and JB Sabater. The effect of flap thickness on the visual and refractive outcome of myopic laser in situ keratomileusis. *Eye*, 19(12):1290, 2005.
- [47] Michael C Chen, Nancy Lee, Nirit Bourla, and D Rex Hamilton. Corneal biomechanical measurements before and after laser in situ keratomileusis. *Journal of Cataract & Refractive Surgery*, 34(11):1886–1891, 2008.
- [48] D Rex Hamilton, R Duncan Johnson, Nancy Lee, and Nirit Bourla. Differences in the corneal biomechanical effects of surface ablation compared with laser in situ keratomileusis using a microkeratome or femtosecond laser. *Journal of Cataract & Refractive Surgery*, 34(12):2049–2056, 2008.
- [49] Kosuke Ogasawara and Tsuyoshi Onodera. Residual stromal bed thickness correlates with regression of myopia after lasik. *Clinical ophthalmology (Auckland, NZ)*, 10:1977, 2016.
- [50] Saira A Choudhri, Susan K Feigenbaum, and Jay S Pepose. Factors predictive of lasik flap thickness with the hansatome zero compression microkeratome. *Journal of refractive surgery*, 21(3):253–259, 2005.
- [51] Daniel H Chang and R Doyle Stulting. Change in intraocular pressure measurements after lasik: the effect of the refractive correction and the lamellar flap. *Ophthalmology*, 112(6):1009–1016, 2005.
- [52] H Razmjoo, A Peyman, A Kashfi, M Peyman, and A Dehghani. A regression model for correcting intraocular lens power after refractive surgery independent of preoperative data. *European journal of ophthalmology*, 16(4):525–529, 2006.
- [53] Boonchai Wangsupadilok and Orasa Horatanaruang. The impact of central corneal thickness on intraocular pressure measured by non-contact tonometry. *Journal of the Medical Association of Thailand*, 94(5):574, 2011.

-
- [54] Sidath E Liyanage and Bruce D Allan. Multiple regression analysis in myopic wavefront laser in situ keratomileusis nomogram development. *Journal of Cataract & Refractive Surgery*, 38(7):1232–1239, 2012.
- [55] Bruce D Allan, Hala Hassan, and Alvin Jeong. Multiple regression analysis in nomogram development for myopic wavefront laser in situ keratomileusis: improving astigmatic outcomes. *Journal of Cataract & Refractive Surgery*, 41(5):1009–1017, 2015.
- [56] Erich L Lehmann and George Casella. *Theory of point estimation*. Springer Science & Business Media, 2006.
- [57] Rob J Hyndman and Anne B Koehler. Another look at measures of forecast accuracy. *International journal of forecasting*, 22(4):679–688, 2006.
- [58] John W Graham. Missing data analysis: Making it work in the real world. *Annual review of psychology*, 60:549–576, 2009.
- [59] Donald B Rubin. Inference and missing data. *Biometrika*, 63(3):581–592, 1976.
- [60] A Rogier T Donders, Geert JMG Van Der Heijden, Theo Stijnen, and Karel GM Moons. A gentle introduction to imputation of missing values. *Journal of clinical epidemiology*, 59(10):1087–1091, 2006.
- [61] Roderick JA Little. A test of missing completely at random for multivariate data with missing values. *Journal of the American statistical Association*, 83(404):1198–1202, 1988.
- [62] Roderick JA Little. Regression with missing x’s: a review. *Journal of the American Statistical Association*, 87(420):1227–1237, 1992.
- [63] Sander Greenland and William D Finkle. A critical look at methods for handling missing covariates in epidemiologic regression analyses. *American journal of epidemiology*, 142(12):1255–1264, 1995.
- [64] Mark A Klebanoff and Stephen R Cole. Use of multiple imputation in the epidemiologic literature. *American journal of epidemiology*, 168(4):355–357, 2008.
- [65] Joseph L Schafer and John W Graham. Missing data: our view of the state of the art. *Psychological methods*, 7(2):147, 2002.

- [66] Stef Van Buuren. *Flexible imputation of missing data*. Chapman and Hall/CRC, 2018.
- [67] Inderjeet Mani and I Zhang. knn approach to unbalanced data distributions: a case study involving information extraction. In *Proceedings of workshop on learning from imbalanced datasets*, volume 126, 2003.
- [68] Peter Hart. The condensed nearest neighbor rule (corresp.). *IEEE transactions on information theory*, 14(3):515–516, 1968.
- [69] Dennis L Wilson. Asymptotic properties of nearest neighbor rules using edited data. *IEEE Transactions on Systems, Man, and Cybernetics*, (3):408–421, 1972.
- [70] Ivan Tomek. Two modifications of cnn. *IEEE Trans. Systems, Man and Cybernetics*, 6:769–772, 1976.
- [71] T Elhassan and M Aljurf. Classification of imbalance data using tomek link (t-link) combined with random under-sampling (rus) as a data reduction method.”. 2016.
- [72] Nitesh V Chawla, Kevin W Bowyer, Lawrence O Hall, and W Philip Kegelmeyer. Smote: synthetic minority over-sampling technique. *Journal of artificial intelligence research*, 16:321–357, 2002.
- [73] Hui Han, Wen-Yuan Wang, and Bing-Huan Mao. Borderline-smote: a new over-sampling method in imbalanced data sets learning. In *International conference on intelligent computing*, pages 878–887. Springer, 2005.
- [74] Chao Liu, Jia Wu, Labrador Mirador, Yang Song, and Weiyan Hou. Classifying dna methylation imbalance data in cancer risk prediction using smote and tomek link methods. In *International Conference of Pioneering Computer Scientists, Engineers and Educators*, pages 1–9. Springer, 2018.
- [75] Li Sun, Ziwei Shang, Qing Cao, Kang Chen, and Jiyun Li. Electrocardiogram diagnosis based on smote+ enn and random forest. In *International Conference on Intelligent Computing*, pages 747–757. Springer, 2019.
- [76] Ahmed Saad Hussein, Tianrui Li, Wondaferaw Yohannese Chubato, and Kamal Bashir. A-smote: A new preprocessing approach for highly imbalanced datasets

- by improving smote. *International Journal of Computational Intelligence Systems*, 2019.
- [77] Lina Gong, Shujuan Jiang, and Li Jiang. Tackling class imbalance problem in software defect prediction through cluster-based over-sampling with filtering. *IEEE Access*, 7:145725–145737, 2019.
- [78] Leo Breiman. Bagging predictors. *Machine learning*, 24(2):123–140, 1996.
- [79] Robert E Schapire. The strength of weak learnability. *Machine learning*, 5(2):197–227, 1990.
- [80] Yoav Freund and Robert E Schapire. A decision-theoretic generalization of on-line learning and an application to boosting. *Journal of computer and system sciences*, 55(1):119–139, 1997.
- [81] Shuang-Quan Wang, Jie Yang, and Kuo-Chen Chou. Using stacked generalization to predict membrane protein types based on pseudo-amino acid composition. *Journal of theoretical biology*, 242(4):941–946, 2006.
- [82] Michael I Jordan and Robert A Jacobs. Hierarchical mixtures of experts and the em algorithm. *Neural computation*, 6(2):181–214, 1994.
- [83] Cem Tekin, Jinsung Yoon, and Mihaela Van Der Schaar. Adaptive ensemble learning with confidence bounds. *IEEE Transactions on Signal Processing*, 65(4):888–903, 2016.
- [84] Debapriya Maji, Anirban Santara, Pabitra Mitra, and Debodoot Sheet. Ensemble of deep convolutional neural networks for learning to detect retinal vessels in fundus images. *arXiv preprint arXiv:1603.04833*, 2016.
- [85] Mário WL Moreira, Joel JPC Rodrigues, Guilherme AB Marcondes, Augusto J Venâncio Neto, and Vasco Furtado. Predicting neonatal condition at birth through ensemble learning methods in pregnancy care. In *Anais do XVIII Simpósio Brasileiro de Computação Aplicada à Saúde*. SBC, 2018.
- [86] Mohamed Hosni, Juan M Carrillo-de Gea, Ali Idri, José Luis Fernández-Alemán, and José A García-Berná. Using ensemble classification methods in lung cancer disease.

- In *2019 41st Annual International Conference of the IEEE Engineering in Medicine and Biology Society (EMBC)*, pages 1367–1370. IEEE, 2019.
- [87] Marina Storani de Almeida and Luis Alberto Carvalho. Different schematic eyes and their accuracy to the in vivo eye: a quantitative comparison study. *Brazilian Journal of Physics*, 37(2A):378–387, 2007.
- [88] Yves LeGrand and Sami G ElHage. *Physiological optics*, volume 13. Springer, 2013.
- [89] Rafael Navarro, Javier Santamaría, and J Bescós. Accommodation-dependent model of the human eye with aspherics. *JOSA A*, 2(8):1273–1280, 1985.
- [90] Isabel Escudero-Sanz and Rafael Navarro. Off-axis aberrations of a wide-angle schematic eye model. *JOSA A*, 16(8):1881–1891, 1999.
- [91] Robert Rosen, Hendrik A Weeber, Carmen Canovas Vidal, Marrie Van Der Mooren, Dora Sellitri, and Patricia Ann Piers. Dual-optic intraocular lens that improves overall vision where there is a local loss of retinal function, July 10 2018. US Patent 10,016,270.
- [92] Robert Rosen, Hendrik A Weeber, Carmen Canovas Vidal, Marrie Van Der Mooren, and Dora Sellitri. Intraocular lens that improves overall vision where there is a local loss of retinal function, October 29 2019. US Patent 10,456,242.
- [93] Yuhang Wu, Chao Ping Chen, Lantian Mi, Wenbo Zhang, Jingxin Zhao, Yifan Lu, Weiqian Guo, Bing Yu, Yang Li, and Nizamuddin Maitlo. Design of retinal-projection-based near-eye display with contact lens. *Optics express*, 26(9):11553–11567, 2018.
- [94] Wenbo Zhang, Chao Ping Chen, Lantian Mi, Yifan Lu, Ming Zhu, Xingyu Ren, Ruixue Tang, and Nizamuddin Maitlo. A retinal-projection-based near-eye display with contact lens for mixed reality. In *Optical Design Challenge 2019*, volume 11040, page 1104005. International Society for Optics and Photonics, 2019.
- [95] Pawan K Shrestha, Matt J Pryn, Jia Jia, Jhen-Si Chen, Hector Navarro Fructuoso, Atanas Boev, Qing Zhang, and Daping Chu. Research article accommodation-free head mounted display with comfortable 3d perception and an enlarged eye-box. 2019.

-
- [96] Pawan K Shrestha, Matt J Pryn, Jia Jia, Jhen-Si Chen, Hector Navarro Fructuoso, Atanas Boev, Qing Zhang, Daping Chu, et al. Accommodation-free head mounted display with comfortable 3d perception and an enlarged eye-box. *Research*, 2019:9273723, 2019.
- [97] Pau Santos Vives. Novel system for measuring the scattering of the cornea and the lens. 2018.
- [98] Wenying Fan, Akihito Uji, Enrico Borrelli, Michael Singer, Min Sagong, Jano van Hemert, and Srinivas R Sadda. Precise measurement of retinal vascular bed area and density on ultra-wide fluorescein angiography in normal subjects. *American journal of ophthalmology*, 188:155–163, 2018.
- [99] Sankrandan Loke and Soumya Jana. *3D Image Reconstruction of Retina using Aplanats*. PhD thesis, Indian Institute of Technology Hyderabad, 2018.
- [100] M Nadeem Akram, Rigmor C Baraas, and Karthikeyan Baskaran. Improved wide-field emmetropic human eye model based on ocular wavefront measurements and geometry-independent gradient index lens. *JOSA A*, 35(11):1954–1967, 2018.
- [101] Francisco Javier Gantes. Predictive modeling of visual quality. 2019.
- [102] Matt Pharr, Wenzel Jakob, and Greg Humphreys. *Physically based rendering: From theory to implementation*. Morgan Kaufmann, 2016.
- [103] Cyril Soler, Kartic Subr, Frédo Durand, Nicolas Holzschuch, and François Sillion. Fourier depth of field. *ACM Transactions on Graphics (TOG)*, 28(2):18, 2009.
- [104] Steven A Cholewiak, Gordon D Love, Pratul P Srinivasan, Ren Ng, and Martin S Banks. Chromablur: Rendering chromatic eye aberration improves accommodation and realism. *ACM Transactions on Graphics (TOG)*, 36(6):210, 2017.
- [105] Trisha Lian, Kevin J MacKenzie, David H Brainard, Nicolas P Cottaris, and Brian A Wandell. Ray tracing 3d spectral scenes through human optics models. *bioRxiv*, page 589234, 2019.
- [106] Todd J Kosloff, Michael W Tao, and Brian A Barsky. Depth of field postprocessing for layered scenes using constant-time rectangle spreading. In *Proceedings of Graphics Interface 2009*, pages 39–46. Canadian Information Processing Society, 2009.

- [107] Kai Selgrad, Christian Reintges, Dominik Penk, Pascal Wagner, and Marc Stamminger. Real-time depth of field using multi-layer filtering. In *Proceedings of the 19th Symposium on Interactive 3D Graphics and Games*, pages 121–127. ACM, 2015.
- [108] Pablo Bauszat, Martin Eisemann, S John, and M Magnor. Sample-based manifold filtering for interactive global illumination and depth of field. In *Computer Graphics Forum*, volume 34, pages 265–276. Wiley Online Library, 2015.
- [109] Martin Kraus and Magnus Strengert. Depth-of-field rendering by pyramidal image processing. In *Computer graphics forum*, volume 26, pages 645–654. Wiley Online Library, 2007.
- [110] David Tarditi, Sidd Puri, and Jose Oglesby. Accelerator: using data parallelism to program gpu for general-purpose uses. *ACM SIGPLAN Notices*, 41(11):325–335, 2006.
- [111] Shuai Che, Michael Boyer, Jiayuan Meng, David Tarjan, Jeremy W Sheaffer, and Kevin Skadron. A performance study of general-purpose applications on graphics processors using cuda. *Journal of parallel and distributed computing*, 68(10):1370–1380, 2008.
- [112] Steven G Parker, James Bigler, Andreas Dietrich, Heiko Friedrich, Jared Hoberock, David Luebke, David McAllister, Morgan McGuire, Keith Morley, Austin Robison, et al. Optix: a general purpose ray tracing engine. In *Acm transactions on graphics (tog)*, volume 29, page 66. ACM, 2010.
- [113] Matthias Nießner, Roman Sturm, and Günther Greiner. Real-time simulation and visualization of human vision through eyeglasses on the gpu. In *Proceedings of the 11th ACM SIGGRAPH International Conference on Virtual-Reality Continuum and its Applications in Industry*, pages 195–202. ACM, 2012.
- [114] Paul Gifford, Tracey Cannon, Cheryl Lee, Deborah Lee, Hai Fang Lee, and Helen A Swarbrick. Ocular aberrations and visual function with multifocal versus single vision soft contact lenses. *Contact Lens and Anterior Eye*, 36(2):66–73, 2013.
- [115] Statista. Number of lasik surgeries in the united states from 1996 to 2020. <https://www.statista.com/statistics/271478/number-of-lasik-surgeries-in-the-us/>. Accessed December 4, 2019.

- [116] Austin W Chang, Alexander C Tsang, Janice E Contreras, Paul D Huynh, Christopher J Calvano, Tracy C Crnic-Rein, and Edmond H Thall. Corneal tissue ablation depth and the munneryn formula. *Journal of Cataract & Refractive Surgery*, 29(6):1204–1210, 2003.
- [117] José R Jiménez, Rosario G Anera, and Luis Jiménez del Barco. Equation for corneal asphericity after corneal refractive surgery. *Journal of Refractive Surgery*, 19(1):65–69, 2003.
- [118] Carmen Canovas, Marrie van der Mooren, Robert Rosén, Patricia A Piers, Li Wang, Douglas D Koch, and Pablo Artal. Effect of the equivalent refractive index on intraocular lens power prediction with ray tracing after myopic laser in situ keratomileusis. *Journal of Cataract & Refractive Surgery*, 41(5):1030–1037, 2015.
- [119] Bertram Meyer, Georg Sluyterman van Langeweyde, and Matthias Wottke. Refractive outcomes of an advanced aspherically optimized profile for myopia corrections by lasik: a retrospective comparison with the standard aspherically optimized profile. *Clinical ophthalmology (Auckland, NZ)*, 9:379, 2015.
- [120] Mohamed Shafik Shaheen, Ahmed Shalaby Bardan, and Hani Ezzeldin. *Ocular Wavefront-Guided Treatment*, pages 185–205. Springer International Publishing, Cham, 2018.
- [121] Fabio A Guarnieri. *Corneal biomechanics and refractive surgery*. Springer, 2015.
- [122] Jiaze Wu, Changwen Zheng, Xiaohui Hu, Yang Wang, and Liqiang Zhang. Realistic rendering of bokeh effect based on optical aberrations. *The Visual Computer*, 26(6-8):555–563, 2010.
- [123] NVIDIA. Cuda c programming guide. <https://docs.nvidia.com/cuda/archive/9.0/cuda-c-programming-guide/index.html>. Accessed Dec. 7, 2019.
- [124] Gene M Amdahl. Validity of the single processor approach to achieving large scale computing capabilities. In *Proceedings of the April 18-20, 1967, spring joint computer conference*, pages 483–485. ACM, 1967.